BOSTON UNIVERSITY

GRADUATE SCHOOL OF ARTS AND SCIENCES

Dissertation

A SEARCH FOR NUCLEON DECAY INTO MODES FAVORED BY SUPERSYMMETRY USING SUPER-KAMIOKANDE

by

MATTHEW ALLEN EARL

B.A., The Johns Hopkins University, 1994
M.A., Boston University, 1999

Submitted in partial fulfillment of the

requirements for the degree of

Doctor of Philosophy

2000

Approved by

First Reader
James L. Stone, Ph.D.
Professor of Physics

Second Reader
Edward T. Kearns, Ph.D.
Associate Professor of Physics

Third Reader
Lawrence R. Sulak, Ph.D.
Professor of Physics

Acknowledgments

I would first like to give thanks to my advisor, Jim Stone, who involved me in the Super–Kamiokande experiment early in my graduate studies and has given me exceptional advice and support throughout my time at Boston University. I thank Ed Kearns for his day-to-day guidance, advice, and encouragement of my work. Thanks to Larry Sulak who has always been enthusiastic and encouraging of my studies in physics. I would also like to thank the rest of my thesis committee, Sekhar Chivukula, Steve Ahlen, and Bill Skocpol. They have always challenged me with tough questions which inspired me to think harder and scrutinize my work more thoroughly.

I deeply appreciate the particle astrophysics group in which I work at Boston University. The discussions, collaboration, and comradary between us has been a great experience. Thanks to post-docs Alec Habig, Chris Walter, and Kate Scholberg and fellow graduate students Shantanu Desai, Mark Messier, and Chris Orth.

I am extremely fortunate to have joined the Super–Kamiokande experiment. I would like to thank spokesmen Yoji Totsuka, Jim Stone, and Hank Sobel for providing such exceptional leadership. The atmospheric neutrino/proton decay data analysis group in which I worked benefitted from the superb leadership of T. Kajita and Ed Kearns and the hard work of a number of people. I would like to especially thank J. Kameda, K. Kobayashi, M. Etoh, Y. Hatakeyama, Y. Hayato, Y. Itow, K. Ishihara, S. Kasuga, C. McGrew, C. Mauger, B. Viren, D. Casper, and T. Barszczak. Special thanks to M. Shiozawa.

I would like to thank my family who have always given me love and support for which I am deeply grateful. My mom and dad have been extremely encouraging throughout my graduate career. This work could not have been completed without them. Thanks to my dad for teaching me his methodology for solving problems. He has been a role model for me. Thanks to my big brothers John, Jimmy, and David for being big brothers. I have always looked up to them.

Finally I would like to thank my wife, Diane. She has endured several of my long trips to Japan at inconvenient moments and remained patient. Without her love, support, and encouragement this work would not have been possible. I am very grateful for her.

The Super–Kamiokande experiment was built from and operated by funding from the Japanese Ministry of Education, Science, Sports, and Culture and the United States Department of Energy.

A SEARCH FOR NUCLEON DECAY INTO MODES FAVORED BY SUPERSYMMETRY USING SUPER–KAMIOKANDE

(Order No.)

MATTHEW ALLEN EARL

Boston University Graduate School of Arts and Sciences, 2000

Major Professor: James L. Stone, Professor of Physics

ABSTRACT

This dissertation presents results of a search for nucleon decay into modes favored by supersymmetric (SUSY) grand unified theories (GUTs) using a 991 day (61.5 kiloton·year) exposure of the the Super–Kamiokande water Cherenkov detector located near Kamioka, Japan. SUSY GUTs predict nucleon decay with lifetimes ranging from 10^{29} to 10^{35} years into modes with a kaon in the final state. The decay modes studied in this dissertation were $p \to \bar{\nu} K^+$, $n \to \bar{\nu} K^0$, $p \to \mu^+ K^0$, and $p \to e^+ K^0$. No evidence for nucleon decay into any of these modes was found; therefore lower limits for the partial lifetime into these modes were set. The limits at the 90% confidence level are (17, 2.5, 12, and 4.4) $\times 10^{32}$ years, respectively. The limits set for $p \to \bar{\nu} K^+$ and $p \to \mu^+ K^0$ exceed limits set by previous experiments by approximately an order of magnitude. The limits for the $n \to \bar{\nu} K^0$ and $p \to e^+ K^0$ modes exceed previous limits by approximately a factor of 3.

Contents

Acknowledgements **iii**

Abstract **v**

Table of Contents **v**

List of Figures **x**

List of Tables **xx**

1 Introduction **1**

2 Theoretical Motivation **5**

2.1 The Standard Model 5

2.1.1 Quarks and Leptons 5

2.1.2 Forces 6

2.1.3 Conservation Laws 7

2.1.4 Symmetry 8

2.1.5 $SU(3)_c \times SU(2)_W \times U(1)_Y$ Description 10

2.1.6 Problems 13

2.2 Grand Unification 13

2.2.1 Running Coupling Constants 14
2.2.2 Minimal SU(5) 14
2.2.3 Supersymmetric GUTs 19

3 Experiments **26**

3.1 Early Experiments 27
3.2 Iron calorimeter 28
3.2.1 Soudan (1981-1990) 29
3.2.2 KGF (1980-1992) 29
3.2.3 NUSEX (1982-1988) 30
3.2.4 Frejus (1984-1988) 30
3.2.5 Soudan 2 (1988-Present) 30
3.3 Water Cherenkov detectors 31
3.3.1 IMB/IMB-3 (1982-1991) 31
3.3.2 Kamiokande (1983-1988) 32
3.3.3 HPW (1983-1984) 33
3.3.4 Super–Kamiokande (1996-Present) 34

4 The Super–Kamiokande Detector **35**

4.1 General 35
4.1.1 Water Cherenkov Detector 35
4.1.2 Structure 37
4.1.3 Water Purification System 38
4.2 Inner Detector Electronics 39
4.2.1 Photomultiplier Tubes 39
4.2.2 Front End Electronics 41
4.2.3 Trigger 42

4.3 Outer Detector Electronics 43
4.3.1 Photomultiplier Tubes 44
4.3.2 Front End Electronics: QTC modules 45
4.3.3 Trigger 46
4.3.4 Data Acquisition 47

5 Calibration **48**
5.1 Relative Gain 48
5.2 Absolute Gain 49
5.3 Timing/Charge (TQ) Calibration 50
5.4 Water Attenuation Length 51
5.4.1 Laser 51
5.4.2 Cosmic-Ray Muons 53
5.5 Energy Scale 55
5.5.1 LINAC 55
5.5.2 Michel Electrons 56
5.5.3 Stopping Muons 57
5.5.4 π^0 Reconstruction 60
5.5.5 Summary of energy scale 61

6 Monte Carlo **63**
6.1 Nucleon decay Monte Carlo 63
6.1.1 Nucleon decay kinematics 63
6.1.2 Nuclear Interactions 66
6.2 Atmospheric Neutrino Monte Carlo 69
6.2.1 Atmospheric Neutrino Flux 70
6.2.2 Neutrino-nucleon Cross sections 71

6.2.3 Propagation of Pions Through Nucleus 78

6.2.4 Normalization of Background 79

6.3 Detector Simulation 81

7 Selection of Contained Events 82

7.1 1st Reduction 82

7.2 2nd Reduction 83

7.3 3rd Reduction 83

7.3.1 Through going muons 83

7.3.2 Stopping muons 84

7.3.3 Low energy event rejection 84

7.3.4 Flasher rejection 85

7.3.5 Cable hole 85

7.4 Final Reduction: flashscan and scanning 86

7.5 Final Event Sample 86

8 Event Reconstruction 88

8.1 Single ring fitting: afit 88

8.2 Ring counting 91

8.3 Particle identification 96

8.3.1 Electron expected PE distribution 97

8.3.2 Muon expected PE distribution 98

8.3.3 Particle identification parameter 99

8.4 Momentum determination 101

8.5 muon/shower (MS) fit 103

8.6 Decay electron counting 103

9 The Search for Nucleon Decay **105**

9.1 $p \to \bar{\nu} K^+$ . . . 106

9.1.1 $K^+ \to \pi^+ \pi^0$ . . . 106

9.1.2 $K^+ \to \mu^+ \nu_\mu$ . . . 110

9.1.3 Final Limit of $p \to \bar{\nu} K^+$ . . . 119

9.2 $n \to \bar{\nu} K^0$ . . . 119

9.2.1 $K_S \to \pi^0 \pi^0$ . . . 119

9.2.2 $K_S \to \pi^+ \pi^-$ . . . 122

9.2.3 Final Limit of $n \to \bar{\nu} K^0$ . . . 125

9.3 $p \to \mu^+ K^0$ . . . 127

9.3.1 $K_S \to \pi^0 \pi^0$ . . . 127

9.3.2 $K_S \to \pi^+ \pi^-$ . . . 130

9.3.3 Final Limit of $p \to \mu^+ K^0$ . . . 136

9.4 $p \to e^+ K^0$ . . . 137

9.4.1 $K_S \to \pi^0 \pi^0$ . . . 137

9.4.2 $K_S \to \pi^+ \pi^-$ . . . 139

9.4.3 Final Limit of $p \to e^+ K^0$ . . . 145

9.5 Summary . . . 147

10 Conclusion **151**

10.1 Summary . . . 151

10.2 Future . . . 152

10.3 Discussion . . . 153

A Setting a Limit **155**

Bibliography **158**

List of Figures

2.1 Picture of $SU(3)$. The gluons $g_{\alpha\bar{\beta}}$, where α and β correspond to the color index, connect different color states. 11

2.2 Simple picture of the Standard Model. The gluons mediate interactions between various color states and $W^{\pm}$ bosons mediate interactions between the $SU(2)$ eigenstates. 13

2.3 Feynman diagrams for new interactions predicted in Grand Unified Theories. 16

2.4 Feynman diagrams for the favored proton decay in minimal $SU(5)$, $p \to e^+\pi^0$. 17

2.5 Evolution of running coupling constants in Minimal $SU(5)$. Equations 2.10 are solved to yield the unification scale M_X and the weak mixing angle $\sin^2\theta_W$. The α_i ($i = 1, 2, 3$) denote the couplings for $U(1)_Y$,$SU(2)_L$, and $SU(3)_c$, respectively. 18

2.6 Evolution of running coupling constants in SUSY. The couplings merge at a scale about an order of magnitude larger than in minimal $SU(5)$. 21

2.7 The Feynman diagram for d=5 interactions predicted in SUSY GUTs. 21

2.8 Feynman diagram for the favored proton decay in Supersymmetric GUTs, $p \to \bar{\nu}K^+$. For $n \to \bar{\nu}K^0$, replace the spectator u quark with a d quark. 22

2.9 **16** multiplet in $SO(10)$. The $\bar{\mathbf{5}}$ and **10** of $SU(5)$ are contained within the **16**. In addition, there is a **1** which corresponds to a left-handed anti-neutrino, the anti-particle of a right-handed neutrino. 23

2.10 Structure of the Pati-Salam right-left symmetric $G(224)$ which is based on a $SU(2)_L \times SU(2)_R \times SU(4)_c$ symmetry. This model provides a place for a right-handed neutrino. 24

4.1 Illustration of Cherenkov radiation. 36

4.2 Schematic of the Super–Kamiokande detector. 37

4.3 Schematic of a supermodule. 38

4.4 Water purification system. 39

4.5 Schematic view of a 50-cm diameter photomultiplier tube used in Super–Kamiokande. 40

4.6 50-cm photomultiplier tube quantum efficiency as a function of photon wavelength. 41

4.7 Layout of the ID electronics 42

4.8 High and low energy trigger rate as a function of elapsed days since the start of data taking on April 1, 1996. 44

4.9 Block diagram of OD electronics. 45

4.10 Block diagram for a single channel (or "daughter" card) of a QTC module. 46

4.11 Cartoon of scope traces for different stages in a single QTC channel. . 47

5.1 Xe/scintillator ball calibration setup. 49

5.2 Relative gain distribution from Xe calibration. 49

5.3 Sample single photoelectron distribution. 50

5.4 Timing calibration: Setup used to measure TQ maps for individual PMTs. 51

5.5 TQ map for a typical PMT. 52

5.6 Setup used to measure water attenuation length at different wavelengths. 52

5.7 Attenuation length calibration for $\lambda = 420$ nm. 53

5.8 Attenuation length vs. wavelength. The solid line shows the model used in the Monte Carlo detector simulation. Points show the measurements using the N_2 laser system. 54

5.9 $\log\left(\frac{Ql}{f(\theta)}\right)$ versus l for cosmic ray muons in a single run of Super–Kamiokande data taking. 55

5.10 Reconstructed momentum distributions for 16-MeV electrons generated by the electron LINAC for both data and Monte Carlo. The agreement is about 1%. 56

5.11 Reconstructed momentum distributions Michel electrons for both data and Monte Carlo. The Monte Carlo simulation is systematically 2.2% lower than the data. 57

5.12 Distributions of $|\vec{p}_Q|$ vs. $|\vec{p}_\theta|$ for data and Monte Carlo low energy ($E < 400$ MeV) stopping muons. The momenta $|\vec{p}_Q|$ and $|\vec{p}_\theta|$ are the momenta calculated from the number of PE detected and the Cherenkov opening angle, respectively. 58

5.13 (a) Binned distributions of $|\vec{p}_Q|/|\vec{p}_\theta|$ vs. $|\vec{p}_\theta|$ for data and Monte Carlo low-energy stopping muons. (b) Percent difference between data and Monte Carlo (Data-MC)/Data. 59

5.14 Distributions of $|\vec{p}_\mu|$ vs. range for data and Monte Carlo stopping muons. The range is defined as the difference between the muon entrance point and the vertex of the decay electron. $|\vec{p}_\mu|$ was calculated using the number of PEs detected. 60

5.15 (a) Binned distributions of $|\vec{p}_\mu|$ vs. range for data and Monte Carlo stopping muons. (b) Percent difference between data and Monte Carlo (Data-MC)/Data. 61

5.16 Invariant mass distributions for π^0s induced by atmospheric neutrinos for both data and Monte Carlo. The agreement is about 3%. 62

6.1 Fermi momentum distributions for s and p states in O^{16}. 64

6.2 Effective mass for nucleons in O^{16}. 65

6.3 Cross sections for the K^+p interaction in the rest frame of the proton. Open triangles and circles correspond to data submitted to the Particle Data Group. Solid boxes and circles correspond to a partial wave analysis by Hyslop *et al.* The line around 600 MeV illustrates the cutoff momentum for K^+ from $p \rightarrow \nu K^+$ in the rest frame of the target proton. 67

6.4 Flux of primary cosmic rays used in Honda's calculation. The top three curves correspond to calculations for solar minimum (top), solar average (middle), and solar maximum (bottom) for Hydrogen. Similarly, the middle three correspond to Helium and the bottom three to CNO. Points are from experimental measurements. 71

6.5 Neutrino flux in the middle of the solar cycle at the Super–Kamiokande site calculated by Honda *et al.* The overall uncertainty is $\sim 20\%$. . . 72

6.6 Charged and neutral current quasi-elastic scattering cross sections for both $\bar{\nu}$ and ν. 73

6.7 Single-pion production cross sections. 75

6.8 Coherent-pion production cross sections. 76

6.9 Multiple-pion production cross sections. 77

6.10 K production cross sections. These cross sections are small compared to those for single-π and multi-π production. 78

6.11 η production cross sections. Like the cross sections for K production, they are small compared to those for single and multi-π production. . 79

6.12 Cumulative probabilities for absorption, inelastic scattering, charge exchange, and no interaction of positively charged pions traversing an O^{16} nucleus as a function of the pion's momentum. 80

6.13 Differential cross sections for π^+-^{16}O scattering. The points show the experimental measurement of Ingram *et al.* and the histogram shows the result of the Monte Carlo simulation. 81

8.1 A $Q(\theta)$ distribution for a 525-MeV electron. 90

8.2 Vertex distributions for the 61 kiloton·year sub-GeV sample. Left figure is for single-ring muons and right figure is for multi-ring events. 91

8.3 Deviation of reconstructed vertex from true vertex for various nucleon decay Monte Carlo samples. 92

8.4 Hough transform procedure. After transforming the PMT coordinates from (x, y, z) space to (θ, ϕ) space, evenly distribute the charge from the PMT in a circle around it. The circles overlap in the center of the Cherenkov ring corresponding to the direction of the track. 93

8.5 An example two-ring event and its hough transforms: a) the actual event b) tube hits in θ-ϕ space c) contour plot of Hough map d) 3-dimensional plot of Hough transform. The two peaks in Hough space can clearly be seen. 94

8.6 Number of rings for the 61-kton·year data sampel (points) and 40-year atmospheric neutrino Monte Carlo (normalized to the 61-kton·year livetime). 95

8.7 Efficiency curves as a function of particle momentum for pions and γ-rays in $p \to \bar{\nu}K^+$, $n \to \bar{\nu}K^0$, $p \to \mu^+K^0$, and $p \to e^+K^0$ Monte Carlo samples. 96

8.8 The expected angular photoelectron distribution corresponding to a 525-MeV electron. This distribution takes into account detector effects like geometry and light attenuation. 98

8.9 The expected angular photoelectron distribution corresponding to a 725-MeV muon. 99

8.10 The particle identification parameter for single ring sub-GeV events for the 991-day exposure of Super–Kamiokande (points with error bars) and the (normalized) 40-year equivalent sample of atmospheric neutrino Monte Carlo. 101

8.11 Conversion from photoelectrons corresponding to a track to momentum for electrons and muons. 102

9.1 $p \to \bar{\nu}K^+;\ K^+ \to \pi^+\pi^0$ Monte Carlo event in unrolled view and front-back view. The two γ-rays from the decay of the π^0 can be seen clearly in both views. A collapsed Cherenkov ring from the π^+ can be seen in the backwards hemisphere (right circle) in the front-back view. The spike in the time histogram around 1250 ns is from the decay electron. 108

9.2 Invariant mass distribution for events passing criteria A1 and A2 for $p \to \bar{\nu}K^+; K^+ \to \pi^+\pi^0$ Monte Carlo and the 40-year equivalent sample of atmospheric neutrino Monte Carlo. 109

9.3 Q_{back} vs. $|\vec{p}_{\gamma\gamma}|$ for $p \to \bar{\nu}K^+; K^+ \to \pi^+\pi^0$ and 40-year atmospheric neutrino Monte Carlo samples. The Q_{back} cut is asymmetric because it maximizes $S/\sqrt{N}$. 111

9.4 Q_{back} vs. $|\vec{p}_{\gamma\gamma}|$ distribution for 61-kton·year data. No events pass the selection criteria. 111

9.5 Sample time of flight (TOF) subtracted timing distribution for a $p \to \bar{\nu}K^+;\ K^+ \to \mu^+\nu_\mu$ Monte Carlo event with prompt γ-ray emission. . 113

9.6 Description of quantities used in the prompt γ-ray search. 115

9.7 N_{hit}^{12ns} distributions for $p \to \bar{\nu}K^+; K^+ \to \mu^+\nu_\mu$ Monte Carlo, 40-year equivalent Monte Carlo event samples, and 61-kton·year SK data. The $p \to \bar{\nu}K^+; K^+ \to \mu^+\nu_\mu$ Monte Carlo was normalized to 2.3 events/61 kton·year. 116

9.8 Momentum spectrum for events passing criteria B1-B2. The points with error bars are the data, the solid line is the 90% C.L. upper limit on the excess of signal events with the atmospheric neutrino Monte Carlo events, and the dashed line is the same as the solid line with the signal excess removed. 118

9.9 $n \to \bar{\nu}K^0$; $K_S \to \pi^0\pi^0$ Monte Carlo event. 120

9.10 $|\vec{p}_{\gamma s}|$ vs. $M_{\gamma s}$ for events passing criteria C1-C2 for $n \to \bar{\nu}K^0$; $K_S \to \pi^0\pi^0$ Monte Carlo and 40-year atmospheric neutrino Monte Carlo. . 121

9.11 $|\vec{p}_{\gamma s}|$ vs. $M_{\gamma s}$ for events passing criteria C1-C2 for $n \to \bar{\nu}K^0$; $K_S \to \pi^0\pi^0$ Monte Carlo and 40-year atmospheric neutrino Monte Carlo. These events also satisfy the requirement that at least one pair of e-like rings reconstructed to the π^0 mass. 122

9.12 $|\vec{p}_{\gamma s}|$ vs. $M_{\gamma s}$ for events passing criteria C1-C2 and the π^0 mass requirement for the 61-kton·year Super–Kamiokande data sample. The number of events passing the selection criteria is consistent with the expected background. 123

9.13 $n \to \bar{\nu}K^0$; $K_S \to \pi^+\pi^-$ Monte Carlo event. 124

9.14 $|\vec{p}_{\pi\pi}|$ vs. $M_{\pi\pi}$ for events passing criteria D1-CD for $n \to \bar{\nu}K^0$; $K_S \to \pi^+\pi^-$ Monte Carlo and 40-year atmospheric neutrino Monte Carlo. . 125

9.15 $|\vec{p}_{\pi\pi}|$ vs. $M_{\pi\pi}$ for events passing criteria D1-D2 the 61-kton·year Super–Kamiokande data sample. Like the search for $n \to \bar{\nu}K^0$; $K_S \to \pi^0\pi^0$, the number of events passing the selection criteria is consistent with the expected background. 126

9.16 $p \to \mu^+K^0$; $K_S \to \pi^0\pi^0$ Monte Carlo in front-back view. The four EM showers from the γs from the decays of the π^0s (left hemisphere) are balanced by the μ track (right hemisphere). Note the spike in the timing histogram at about 1600 ns from the decay electron of the μ. 128

9.17 Momentum vs. mass for events passing criteria E1-E3 for $p \to \mu^+K^0$; $K_S \to \pi^0\pi^0$ Monte Carlo and 40-year atmospheric neutrino Monte Carlo. 129

9.18 μ momentum vs. e-like mass for events passing selection criteria E1-E5 for $p \to \mu^+ K^0$; $K_S \to \pi^0\pi^0$ Monte Carlo and 40-year atmospheric neutrino Monte Carlo. 130

9.19 Total momentum vs. total mass and μ momentum vs. e-like mass for the 61-kton·year data sample in searching for $p \to \mu^+ K^0$; $K_S \to \pi^0\pi^0$. The events in the left figure have passed criteria E1-E3 and the events in the right figure have passed E4-E5. 131

9.20 $p \to \mu^+ K^0$;$K_S \to \pi^+\pi^-$ Monte Carlo event in unrolled view and front-back view. The two collapsed Cherenkov rings from the two pions from the decay of the K_S balance the track from the muon. Note the two spikes in the timing histogram at about 1500 ns and 1700 ns from the two decay electrons. 132

9.21 $|\vec{p}_{tot}|$ vs. M_{tot} for events passing criteria F1-F2 for $p \to \mu^+ K^0$;$K_S \to \pi^+\pi^-$ Monte Carlo and 40-year atmospheric neutrino Monte Carlo. . 134

9.22 Invariant mass of the two pions for events passing selection criteria F1-F4 for $p \to \mu^+ K^0$; $K_S \to \pi^+\pi^-$ Monte Carlo and 40-year atmospheric neutrino Monte Carlo. 134

9.23 $|\vec{p}_{tot}|$ vs. M_{tot} for events passing selection criteria F1-F2 for the 61-kton·year data sample. 135

9.24 Distribution of $|\vec{p}_{tot}|$ vs. $|\vec{p}_\mu|$ for events passing selection criteria G1-G2 for $p \to \mu^+ K^0$; $K_S \to \pi^+\pi^-$ Monte Carlo and 40-year atmospheric neutrino Monte Carlo. 136

9.25 Distribution of $|\vec{p}_{tot}|$ vs. $|\vec{p}_\mu|$ for events passing selection criteria G1-G2 for the 61-kton·year data sample. 137

9.26 Momentum vs. mass for events passing criteria H1-H2 for $p \rightarrow e^+K^0$; $K_S \rightarrow \pi^0\pi^0$ Monte Carlo and 40-year atmospheric neutrino Monte Carlo. 139
9.27 Momentum vs. mass for events passing criteria H1-H2 the 61-kton·year Super–Kamiokande data sample. 140
9.28 $p \rightarrow e^+K^0$; $K_S \rightarrow \pi^+\pi^-$ Monte Carlo event. The two lower energy collapsed Cherenkov rings are from the π^+ and π^- from the K_S decay. 141
9.29 Momentum vs. mass for events passing criteria I1-I2 for $p \rightarrow e^+K^0$; $K_S \rightarrow \pi^+\pi^-$ Monte Carlo and 40-year atmospheric neutrino Monte Carlo. 142
9.30 Invariant mass of the two pions for events passing selection criteria I1-I4 for $p \rightarrow e^+K^0$; $K_S \rightarrow \pi^+\pi^-$ Monte Carlo and 40-year atmospheric neutrino Monte Carlo. 142
9.31 a) Total momentum vs. total mass for the 61-kton·year data sample for events passing selection criteria I1-I2. b) $M_{\pi\pi}$ for the data event in the 61-kton·year data sample which passed selection criteria I1-I4. 143
9.32 Distribution of $|\vec{p}_{tot}|$ vs. $|\vec{p}_e|$ for events passing selection criteria J1-J3 for $p \rightarrow e^+K^0$; $K_S \rightarrow \pi^+\pi^-$ Monte Carlo and 40-year atmospheric neutrino Monte Carlo. 145
9.33 Data search for $p \rightarrow e^+K^0$; $K_S \rightarrow \pi^+\pi^-$ with selection criteria J1-J5. Total momentum vs. total mass for the 61-kton·year data sample. . . 146

10.1 Summary of limits set in this dissertation and previous limits. 152

List of Tables

2.1 Quarks and Leptons in the Standard Model 6

2.2 Some mesons and their quark content. 6

2.3 Gauge bosons in the Standard Model 7

2.4 Standard Model particles and their supersymmetric partners. 19

2.5 Summary of selected Grand Unified Theories and their predictions for nucleon decay. 25

3.1 Summary of indirect detection methods 28

3.2 Summary of various parameters of Iron Calorimeters. 31

3.3 Summary of Water Cherenkov Detectors 34

4.1 50-cm PMT characteristics. 41

4.2 Trigger types 43

6.1 Decay modes of N^{15*} which have γ-rays as decay products. 66

9.1 Breakdown of background contributions to the decay $p \to \bar{\nu}K^+$; $K^+ \to \pi^+\pi^0$. N_{norm} is the number normalized to the neutrino oscillation hypothesis (see section 6.2.4 for an explanation). The % is the normalized percentage contribution to the background. 112

9.2 Breakdown of background contributions to the decay $p \rightarrow \bar{\nu}K^+$; $K^+ \rightarrow \mu^+\nu_\mu$ with a prompt-γ ray emission. (See table 9.1 for an explanation of N_{norm} and %.) 117
9.3 Summary of three methods used to search for $p \rightarrow \bar{\nu}K^+$. 119
9.4 Breakdown of background contributions to the decay $n \rightarrow \bar{\nu}K^0$; $K_S \rightarrow \pi^0\pi^0$ (see table 9.1 for an explanation of N_{norm} and %.) 123
9.5 Breakdown of background contributions to the decay $n \rightarrow \bar{\nu}K^0$; $K_S \rightarrow \pi^+\pi^-$. 126
9.6 Summary of two methods used to search for $n \rightarrow \bar{\nu}K^0$ (see table 9.1 for an explanation of N_{norm} and %.) 127
9.7 Breakdown of background contributions to the decay $p \rightarrow \mu^+K^0$; $K_S \rightarrow \pi^0\pi^0$ (see table 9.1 for an explanation of N_{norm} and %.) . . . 133
9.8 Breakdown of background contributions to the decay $p \rightarrow \mu^+K^0$; $K_S \rightarrow \pi^+\pi^-$ in the scenario where only two rings were reconstructed (See table 9.1 for an explanation of N_{norm} and %.) 138
9.9 Summary of three methods used to search for $p \rightarrow \mu^+K^0$. 138
9.10 Breakdown of background contributions to the decay $p \rightarrow e^+K^0$; $K_S \rightarrow \pi^0\pi^0$ (see table 9.1 for an explanation of N_{norm} and %.) . . . 140
9.11 Breakdown of background contributions to the decay $p \rightarrow e^+K^0$; $K_S \rightarrow \pi^+\pi^-$ for the two-ring scenario (see table 9.1 for an explanation of N_{norm} and %.) 146
9.12 Summary of three methods used to search for $p \rightarrow e^+K^0$. 147
9.13 Summary of K mesons. Values taken from the Particle Data Book. . 147
9.14 Summary of final results for searches for $p \rightarrow \bar{\nu}K^+$, $n \rightarrow \bar{\nu}K^0$, $p \rightarrow \mu^+K^0$, and $p \rightarrow e^+K^0$. 148
9.15 Summary of the selection criteria used to search for $p \rightarrow \bar{\nu}K^+$. 148

9.16 Summary of the selection criteria used to search for $n \rightarrow \bar{\nu} K^0$ 149

9.17 Summary of the selection criteria used to search for $p \rightarrow \mu^+ K^0$ 149

9.18 Summary of the selection criteria used to search for $p \rightarrow e^+ K^0$ 150

10.1 Summary of limits studied in this dissertation for Super–Kamiokande, IMB, Kamiokande, and Soudan II. 151

Chapter 1

Introduction

The goal of particle physics is to understand nature at its most fundamental level. By exploring the world at ever decreasing distance scales, particle physicists have been able to dig deeper and deeper into the subatomic world. Probing smaller distances has required increasingly powerful particle accelerators which serve as microscopes which can see into the subatomic world. These powerful machines accelerate particles to high energies and provide a mechanism by which new particles can be materialized and smaller distances can be probed.

Physical observations change when probing smaller distances, or equivalently, higher energies. For instance, by the mid 1930s it was known that atoms are made of a small dense nucleus composed of neutrons and protons around which electrons orbit. At this time it was thought that protons were fundamental, however it was learned in the 1960s that protons are composed of smaller constituents called “quarks” [1]. This was accomplished by probing protons with electrons having sufficiently high energies [2]. In this way, the understanding of particle physics became more accurate when looking at smaller distance scales.

Through the years, physicists have been able to build accelerators which could accelerate particles to higher and higher energies and in doing so many exciting discoveries were made. After years of exploring the energy frontier with these machines and developing theories based on these measurements, the Standard Model of particle physics has been created. This is the model that is widely accepted today. The current understanding is that there are a handful of fundamental particles out of which everything is made. Protons and neutrons are composed of the fundamental "up" and "down" quarks. Electrons, which orbit nuclei composed of protons and neutrons to make atoms, are themselves fundamental. Heavier versions of the up and down quarks and the electron also exist but are unstable and decay before they can form something that we can touch, see, or feel. There are also elusive neutrinos which are very light and difficult to detect. Finally, there are four fundamental forces: strong, electromagnetic, weak, and gravity.

It is reasonable to ask the question: is this present understanding of natural phenomena sufficient to describe physics at even smaller distances (or equivalently, higher energies)? Theoretical predictions and experimental data suggest that the four forces behave differently at extremely short distances. In fact, these predictions state that at distances of more than 10^{13} times shorter than the current ability to probe, the forces have the same strength: they are said to be "unified." But how can such small distances be probed? The energy required is about 10^{13} times more than the current technology allows. It is likely impossible to build a particle accelerator capable of achieving such a large energy. This is where searching for proton decay becomes useful.

To understand why proton decay is so useful, first think about the four forces in nature. For each of these, there are force-carrying particles which transmit the forces. An analogy can be drawn to two people playing catch. By passing the ball back and forth, the ball exchanges a force between the two people. By comparing the rate at which we can pass a golf ball back and forth to the rate at which we can pass a 50-lb. medicine ball back and forth, it is easy to see that the latter has a much slower rate. In a similar way, in the subatomic world, heavier force carriers result in processes which proceed at a slower rate. Consider the decay of the muon (a heavier version of the electron) which is caused by the weak force. Compared to the decay of a particle via the strong or electromagnetic force, the muon lifetime is extremely long. This can be attributed to the exchange of the heavy particle which mediates the weak force, the W boson.

Let us now return to the theories where the four forces are unified at a very small distance scale. In these theories, new force carrying particles which are not part of the Standard Model exist which can cause protons to decay. However the masses of these particles are extremely large: more than 10^{13} times larger than the W boson. Therefore proton decay is predicted to be extremely rare and proton lifetimes predicted to be extremely long.

Since proton decay is the result of a physics process which occurs at an extremely short distance scale, searching for it is an indirect probe of these short distances (or equivalently, high energies). In this way proton decay provides a method by which we can probe energies which are unattainable by accelerator experiments.

The experimental method to search for nucleon decay is simple (nucleon is a generic term for either a proton or a neutron residing in a nucleus of an atom). A very large sample of nucleons is assembled and observed for a period of time with a detector which can detect the decay products of a single nucleon. This dissertation utilizes the Super–Kamiokande detector which sits deep underground in the Mozumi mine of the Kamioka Mining and Smelting company in the Japanese Alps. The volume of the detector is water, which serves as the source of nucleons. The walls of the tank are lined with photomultiplier tubes which detect the Cherenkov light from particles passing through the volume of the tank. If a nucleon in a water molecule decays, its decay products will generate this radiation. The patterns of Cherenkov light projected onto the walls of the detector and detected by the photomultiplier tubes will have characteristics which will distinguish it as a nucleon decay event.

This dissertation presents the results of a search for nucleon decay into modes favored by a specific type of unification theory: supersymmetric grand unification. This theory is elaborate in that it postulates the existence of an entirely new set of particles. For every particle in the Standard Model, it is postulated that there exists a corresponding "superpartner." These particles have not yet been observed however some of them have masses which are just above the current ability to probe with accelerators. Other "superpartners" are extremely heavy and cause nucleons to decay into specific modes. Observation of nucleon decay into these modes would be a hint of things to come at the next generation accelerator, the Large Hadron Collider (LHC) in Europe, set to turn on within the next decade. It would also provide a window into an energy frontier which no collider will ever be able to look directly.

Chapter 2

Theoretical Motivation

2.1 The Standard Model

2.1.1 Quarks and Leptons

Quarks and leptons are the fundamental spin-$\frac{1}{2}$ fermions in the Standard Model (see table 1). The electron and its corresponding neutrino, with charges of -1 and 0, are some familiar leptons. In contrast to leptons, quarks are fractionally charged fundamental particles which cannot exist by themselves but comprise hadronic particles such as protons, neutrons, and pions. For example, a proton is composed of two "up" quarks and one "down" quark. A positively charged pion is a bound state of one "up" quark and the anti-particle of the "down" quark. Pions are examples of mesons which in general are composed of a quark and an anti-quark (see table 2.2 for a list of some mesons and their quark content). Every fermion listed in table 2.1 has a corresponding anti-particle which has the same mass but opposite quantum numbers. For example, the positron is the antiparticle of the electron with charge of $Q = +1$.

	particle	*mass* (MeV/c^2)	*charge*	*Lepton no.*	*Baryon no.*
	ν_e	0	0	$L_e = 1$	0
First	e^-	0.511	-1	$L_e = 1$	0
Family	up quark (u)	a few MeV/c^2	$\frac{2}{3}$	0	$\frac{1}{3}$
	down quark (d)	a few MeV/c^2	$-\frac{1}{3}$	0	$\frac{1}{3}$
	ν_μ	0	0	$L_\mu = 1$	0
Second	μ^-	105.7	-1	$L_\mu = 1$	0
Family	charm quark (c)	1.3×10^3	$\frac{2}{3}$	0	$\frac{1}{3}$
	strange quark (s)	~ 100	$-\frac{1}{3}$	0	$\frac{1}{3}$
	ν_τ	0	0	$L_\tau = 1$	0
Third	τ^-	1.78×10^3	-1	$L_\tau = 1$	0
Family	top quark (c)	$\sim 1.7 \times 10^5$	$\frac{2}{3}$	0	$\frac{1}{3}$
	bottom quark (s)	4.2×10^3	$-\frac{1}{3}$	0	$\frac{1}{3}$

Table 2.1: Quarks and Leptons in the Standard Model

Meson	**Quark Content**	*mass* (MeV/c^2)
π^+	ud	139.6
π^0	$\frac{1}{2}(u\bar{u} - d\bar{d})$	135.0
π^-	$d\bar{u}$	139.6
K^+	$u\bar{s}$	493.7
K^0	$d\bar{s}$	497.7
$\bar{K}^0$	$s\bar{d}$	497.7
K^-	$s\bar{u}$	493.7

Table 2.2: Some mesons and their quark content.

2.1.2 Forces

Four fundamental forces are observed in nature: strong, electromagnetic, weak, and gravity. The strong force is responsible for holding nuclei together, electromagnetism accounts for the force between two charged particles, and the weak force mediates decay processes such as beta decay $n \to pe^-\bar{\nu}_e$. Gravity is the most familiar to us, but is the weakest and least understood of the four.

The fundamental forces are mediated via the exchange of gauge bosons which

particle	*Force*	*mass* (MeV/c^2)	*charge*	*Relative Strength*
gluons (g)	strong	0	0	~ 1
photon (γ)	electromagnetic	0	0	$\sim 1/137$
W bosons ($W^{\pm}$)	weak	80.4×10^3	± 1	$\sim 10^{-5}$
Z boson (Z^0)	weak	91.2×10^3	0	$\sim 10^{-5}$
graviton	gravity	0	0	$\sim 10^{-38}$

Table 2.3: Gauge bosons in the Standard Model

are transfered between particles experiencing the force. “Gluons” carry the strong force between quarks in nuclei. The light quantum, the photon, transmits the electromagnetic force between charged particles. The weak force is mediated by the $W^{\pm}$ and Z^0 bosons. Experimental evidence for the gluons, $W^{\pm}$, Z^0, and γ exists. It is postulated that gravity is mediated by a “graviton,” however there is no direct experimental evidence for its existence. Table 2.3 summarizes the properties of the four forces.

2.1.3 Conservation Laws

Quantities which do not change with time are designated as “conserved.” For example, energy, momentum, and angular momentum are three kinematic quantities that are conserved in all interactions. Another important quantity which is conserved in all interactions is charge: the sum of all charges in the initial state of a reaction must equal the sum of all charges in the final state of a reaction.

The lepton and baryon quantum numbers which are outlined in table 2.1 are conserved in all observed interactions. For instance, the μ decay $\mu \to e\gamma$ via the electromagnetic interaction does not occur because it does not conserve lepton number. The initial state has $L_\mu = 1$ and $L_e = 0$ and the final state has $L_\mu = 0$ and $L_e = 1$. An example of a baryon number violating process is the proton decay $p \to e^+\pi^0$

which has an initial state of $B = 1$ and a final state of $B = 0$. The idea of baryon number conservation was first proposed by Weyl in 1929 [3] when he postulated that the proton was the Dirac counterpart to the electron. As a result, the number of electrons and protons remain constant in an interaction. After the discovery of the positron (the actual counterpart to the electron) the idea of baryon number conservation was refined by Stückelberg in 1938 [4] and again by Wigner in 1949 [5]. With these proposals, protons and neutrons were assigned a "heavy charge" which corresponds to baryon number. This postulation of baryon number conservation led to experiments which set out to test the proposal.

2.1.4 Symmetry

Conserved quantities and symmetries in particle physics are intimately related. This can be seen using the Lagrangian formulation to describe a system. A physical system can be described by its Lagrangian, from which the classical equations of motion can be derived. If the form of the Lagrangian remains unchanged after transforming the fields in the Lagrangian (by a rotation or translation, for instance), it is "symmetric" under the transformation. For each of these possible transformations for which the Lagrangian remains invariant, there is an associated conservation law. Examples are conservation of energy, momentum, and angular momentum which follow from the invariance of the Lagrangian under general Lorentz space-time transformations. In addition to the conserved quantities associated with space-time transformations there are internal symmetries which are not dependent upon the spatial and temporal coordinates of the system. An example of an internal symmetry is isospin invariance in nuclear interactions.

Physicists typically utilize group theory to describe symmetries and conservation laws. To show how this works, consider the group $SU(2)$ which is used to describe the spin-$\frac{1}{2}$ system of quantum mechanics. The commutation relations of the generators completely describe $SU(2)$

$$[L_i, L_j] = i\epsilon_{ijk}L_k \tag{2.1}$$

where ϵ_{ijk} is the completely antisymmetric tensor and (i, j, k) correspond to the (x, y, z) coordinates. The L_i matrices can be written in terms of the Pauli spin matrices σ_i as $L_i = \frac{1}{2}\sigma_i$ which are traceless unitary matrices. It follows that any arbitrary traceless unitary matrix can be written as

$$\mathcal{R} = e^{i\vec{\alpha}\cdot\vec{L}} \tag{2.2}$$

where $\vec{\alpha}$ is an arbitrary scaling vector. The L_i's can generate any general transformation within the space and are therefore called "generators." The two physical states spin-up, $|+\rangle$, and spin-down,$|-\rangle$, are the orthogonal eigenstates of the system and constitute a "spin-$\frac{1}{2}$ doublet." Any state in the system can be written as a linear combination of these two eigenstates. Finally, there are two important operators

$$L_{\pm} = (L_1 \mp iL_2) \tag{2.3}$$

which represent mixing between states, $L_{\pm}|\mp\rangle = |\pm\rangle$. The entire system may now be described in terms of its "generator matrix" L and its "doublet" ψ

$$L = \frac{1}{2}\begin{bmatrix} l_z & l_+ \\ l_- & -l_z \end{bmatrix} \quad \psi \rightarrow \begin{pmatrix} \text{up} \\ \text{down} \end{pmatrix} \tag{2.4}$$

The diagonal elements of L represent the projection of the state ψ while the off-diagonal elements represent transformations between eigenstates. This is where an analogy can be drawn to a system in particle physics: the matrices L_z and $L_\pm$ can be compared to "gauge bosons" (the Z and $W^\pm$ bosons, for example) and the "doublet" can be compared to a physical doublet of fermions (the electron and its neutrino, for example). This example can now be used to provide a basic description of the Standard Model of particle physics.

2.1.5 $SU(3)_c \times SU(2)_W \times U(1)_Y$ Description

The Standard Model is based on the direct product $SU(3)_c \times SU(2)_L \times U(1)_Y$ gauge group. The group $SU(3)_c$ describes the strong force between the quarks. The quarks have "color charge" and comprise a color triplet ψ_c having states arbitrarily labeled red, green, and blue. The gluons can be represented in the generator matrix $\mathbf{G_{gluons}}$ and the system can be compactly written

$$\mathbf{G_{gluons}} = \begin{bmatrix} g_{r\bar{r}} & g_{r\bar{g}} & g_{r\bar{b}} \\ g_{g\bar{r}} & g_{g\bar{g}} & g_{g\bar{b}} \\ g_{b\bar{r}} & g_{b\bar{g}} & g_{b\bar{b}} \end{bmatrix} \quad \psi_c \rightarrow \begin{pmatrix} \text{red} \\ \text{green} \\ \text{blue} \end{pmatrix} \tag{2.5}$$

where $g_{b\bar{b}} = -g_{r\bar{r}} - g_{g\bar{g}}$. This description is the analog $SU(3)_c$ description of $SU(2)$ described in equation 2.4. The off diagonal matrix elements of $\mathbf{G_{gluons}}$ represent the coupling of the different color states to one another. A pictorial representation of the $SU(3)$ system is shown in figure 2.1.

Electroweak theory is the unification of electromagnetism and the weak force. It is governed by the direct product $SU(2)_L \times U(1)_Y$ symmetry [6, 7, 8]. The subscript L on $SU(2)$ is the statement that only left-handed particles are subject to interactions of this symmetry group, the so-called "V-A" interaction. Neglecting mass, left-handed particles are particles whose spin vector is in the opposite direction of its momentum

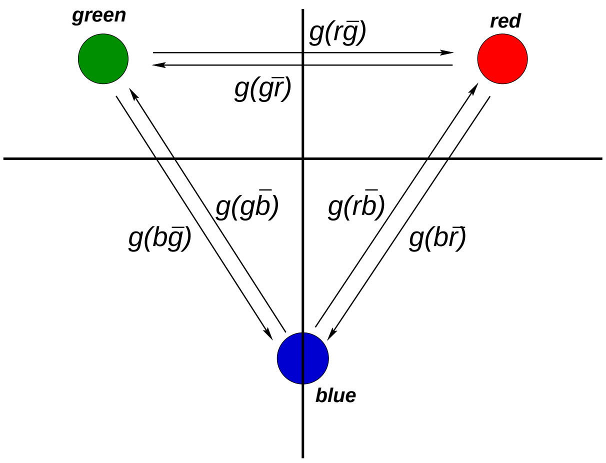

Figure 2.1: Picture of $SU(3)$. The gluons $g_{\alpha\bar{\beta}}$, where α and β correspond to the color index, connect different color states.

vector. The subscript Y on $U(1)$ denotes a quantity called "weak-hypercharge" which is defined to be

$$Y = \frac{1}{2}(Q - T_3) \tag{2.6}$$

where Q is charge from electromagnetism and T_3 is the eigenvalue for the 3rd component of weak isospin from $SU(2)_L$. From equation 2.6 one can see that electromagnetism and the weak interaction are intimately related.

If unbroken, the gauge theory of $SU(2)_L \times U(1)_Y$ is related to four massless gauge bosons, $W^{\mu}_{1,2,3}$ from $SU(2)_L$ and a_μ from $U(1)_Y$. This is not consistent with observations in nature which has one massless boson (the photon) and three massive ($W^{\pm}$ and Z bosons) gauge bosons. One way to resolve this is to introduce a scalar particle called the Higgs boson. The Higgs generates masses for the W and Z bosons and mixes the massless gauge bosons corresponding to the massive Z of the weak interaction and the massless photon of electromagnetism

$$Z^{\mu} = -a^{\mu}\sin\theta_W + W^{\mu}_3\cos\theta_W \tag{2.7}$$

$$A^\mu = a^\mu \cos\theta_W + W_3^\mu \sin\theta_W \tag{2.8}$$

where μ is the space-time Lorentz index, A^μ is the massless gauge field of electromagnetism (the photon), and θ_W is the "weak mixing angle" which parameterizes the relation between the weak and electromagnetic forces. The coupling constants of $SU(2)_L$ and $U(1)_Y$ can then be expressed in terms of the fine structure constant α_{em} of electromagnetism and θ_W.

The particles from table 2.1 form the weak doublets

$$\begin{pmatrix} \nu_e \\ e \end{pmatrix}_L \begin{pmatrix} u \\ d' \end{pmatrix}_L \; ; \begin{pmatrix} \nu_\mu \\ \mu \end{pmatrix}_L \begin{pmatrix} c \\ s' \end{pmatrix}_L \; ; \begin{pmatrix} \nu_\tau \\ \tau \end{pmatrix}_L \begin{pmatrix} t \\ b' \end{pmatrix}_L \tag{2.9}$$

The subscript L denotes left-handedness. The d',s', and b' in the weak doublets are actually admixtures of the color d, s, and b mass eigenstates. These admixtures are parameterized by the Cabibbo-Kobayashi-Maskawa mixing matrix [9, 10].

The quarks come in both $SU(3)_c$ color triplets and $SU(2)_L$ weak doublets, however the leptons come only in $SU(2)_L$ weak doublets. They do not come in $SU(3)_c$ triplets and for this reason they are called "color singlets" which means that they do not feel the "color" force. There are also right-handed leptons, e_R, μ_R, and τ_R, and right handed quarks. The right-handed leptons are both color singlets and singlets under $SU(2)_L$ while the right-handed quarks are color triplets but singlets under $SU(2)_L$. An important aspect of the Standard Model is that a right-handed neutrino (or left-handed anti-neutrino) does not exist. A graphical description of the first family of the $SU(3)_c \times SU(2)_L \times U(1)_Y$ standard model is shown in figure 2.2.

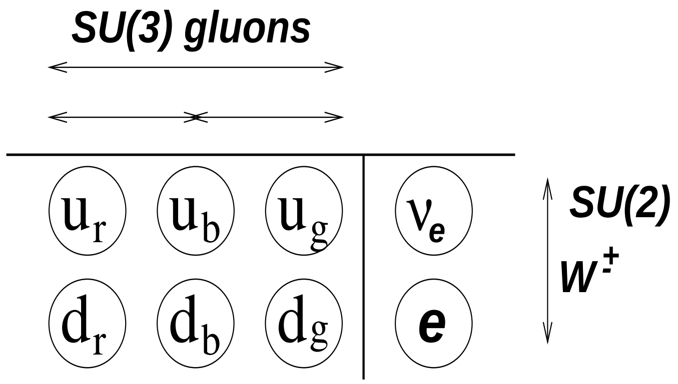

Figure 2.2: Simple picture of the Standard Model. The gluons mediate interactions between various color states and $W^{\pm}$ bosons mediate interactions between the $SU(2)$ eigenstates.

2.1.6 Problems

Despite the success of the Standard Model, there remain some unanswered questions. To name a few:

- Why is nature described by the direct product $SU(3)_c \times SU(2)_L \times U(1)_Y$ symmetry group?
- Why are the charges of quarks in units of 1/3 the electron charge?
- Why do both quarks and leptons come in weak doublets?

Grand Unification Theories (GUTs) attempt to explain these questions.

2.2 Grand Unification

Grand Unified Theories (GUTs) are an attempt to unify the forces in nature into a single force at some large energy scale. This means that at some extremely small distance scale the forces in nature become indistinguishable from one another. This is described quantitatively by the merging of the coupling constants of the forces at this high energy scale. When constructing such theories one must choose a symmetry group which contains the observed $SU(3) \times SU(2) \times U(1)$ structure of the Standard Model such as $SU(5)$ or $SO(10)$. By examining the structure of the symmetry group, predictions can be made and tested against experiment. Nucleon decay is predicted by all GUTs in which $SU(3)_c \times SU(2)_L$ are unified in a single group and is therefore a good experimental test of these theories.

2.2.1 Running Coupling Constants

The coupling constants of the strong and electroweak interactions are not actually constants but vary with increasing energy scales (or equivalently, decreasing distance scales). One of the first hints of Grand Unification was the apparent convergence of the three coupling constants $\alpha_{1,2,3}$ at some extremely high energy scale. The evolution of α_i's is described quantitatively to first order by

$$\frac{1}{\alpha_i\left(E\right)} = \frac{1}{\alpha_{GUT}} + \frac{1}{6\pi} b_i \log \frac{M_X}{E} \tag{2.10}$$

where α_i $(i = 1, 2, 3)$ are the coupling constants of the $U(1)_Y$, $SU(2)_L$, and $SU(3)_c$ interactions. E is the energy scale at which the measurements are made, α_{GUT} is the value of α when the couplings meet, M_X is the GUT energy scale, and b_i are the coefficients for the first order calculations. The coefficients b_i are specific to the different theories and depend on the number and charges of the fermions.

2.2.2 Minimal SU(5)

The smallest gauge group which can contain $SU(3) \times SU(2) \times U(1)$ is $SU(5)$. The simplest GUT based on this symmetry group is called "Minimal $SU(5)$" and was first proposed by Georgi and Glashow in 1974 [11]. The generator matrix is written as

$$\mathbf{V}_{SU(5)} = \begin{bmatrix} g_{r\bar{r}} - \frac{2}{\sqrt{30}}a & g_{r\bar{g}} & g_{r\bar{b}} & X_1 & Y_1 \\ g_{g\bar{r}} & g_{g\bar{g}} - \frac{2}{\sqrt{30}}a & g_{g\bar{b}} & X_2 & Y_2 \\ g_{b\bar{r}} & g_{b\bar{g}} & g_{b\bar{b}} - \frac{2}{\sqrt{30}}a & X_3 & Y_3 \\ \bar{X}_1 & \bar{X}_2 & \bar{X}_3 & \frac{1}{\sqrt{2}}W^3 + \frac{3}{\sqrt{30}}a & W^+ \\ \bar{Y}_1 & \bar{Y}_2 & \bar{Y}_3 & W^- & -\frac{1}{\sqrt{2}}W^3 + \frac{3}{\sqrt{30}}a \end{bmatrix} \tag{2.11}$$

and the fermions are contained in the $\bar{\mathbf{5}}$ and $\mathbf{10}$ representations (analogous to the doublet in $SU(2)$ and the triplet in $SU(3)$)

$$\bar{\mathbf{5}} = \begin{pmatrix} \bar{d}_r \\ \bar{d}_g \\ \bar{d}_b \\ e^- \\ -\nu_e \end{pmatrix}_L \qquad \mathbf{10} = \left[\begin{array}{ccc|cc} 0 & \bar{u}_b & -\bar{u}_g & -u_r & -d_r \\ -\bar{u}_b & 0 & \bar{u}_r & -u_g & -d_g \\ \bar{u}_g & -\bar{u}_r & 0 & -u_b & -d_b \\ \hline u_r & u_g & u_b & 0 & e^+ \\ d_r & d_g & d_b & -e^+ & 0 \end{array}\right]_L \tag{2.12}$$

The $SU(3) \times SU(2) \times U(1)$ structure of the Standard Model is completely contained in this description: the upper left 3×3 of $\mathbf{V}_{SU(5)}$ contain the gluons of $SU(3)$ and the bottom right 2×2 contain the Ws of $SU(2)$. The diagonal elements also contain $U(1)_Y$. Below the masses $M_{X,Y}$ the $SU(3) \times SU(2) \times U(1)$ picture becomes valid: $SU(5)$ is said to be "broken" to the $SU(3) \times SU(2) \times U(1)$ structure of the Standard Model.

An attractive feature following from this theory is charge quantization. The photon corresponds to the charge generator and is contained in $\mathbf{V}_{SU(5)}$. The generators of the group must be traceless so applying the charge operator on the $\bar{\mathbf{5}}$ implies the condition

$$3Q(d) = -Q(e^+) \tag{2.13}$$

explaining why charges of quarks are in units of 1/3 the charge of the electron.

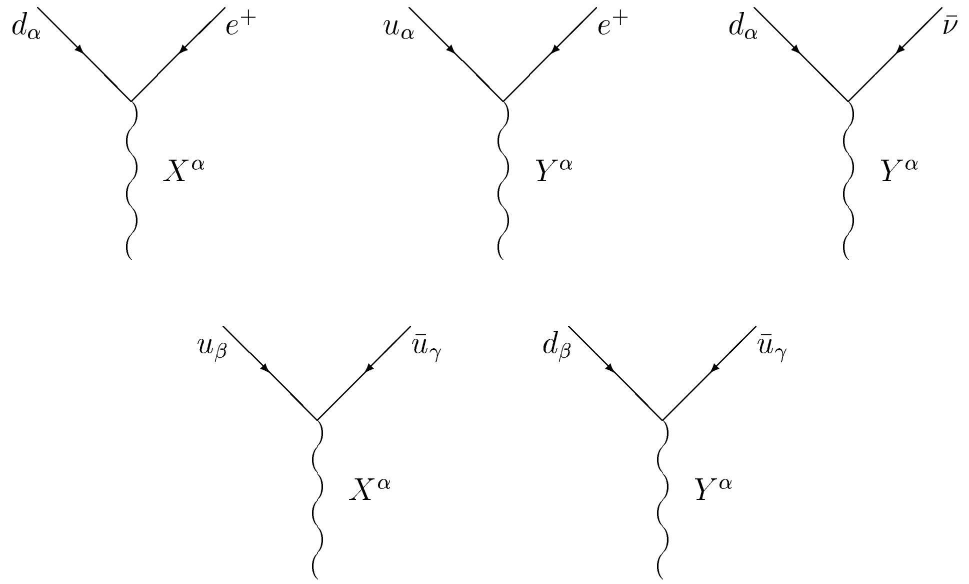

Figure 2.3: Feynman diagrams for new interactions predicted in Grand Unified Theories.

In addition to the bosons of the Standard Model, $\mathbf{V}_{SU(5)}$ contains new X and Y gauge bosons with masses $M_{X,Y}$ which mediate new interactions not contained in the Standard Model (figure 2.3). These interactions do not conserve baryon or lepton number (B or L) but do conserve $B - L$ and lead to nucleon decay via the exchange of one of these massive bosons. Some examples of the favored proton decay mode in mimimal $SU(5)$, $p \to e^+\pi^0$, are shown in figure 2.4. The proton lifetime has the following dependence

$$\tau_p \left(p \to e^+\pi^0\right) \sim \frac{1}{\alpha_{GUT}^2} \frac{M_X^4}{m_p^5} \tag{2.14}$$

where m_p is the mass of the proton and $M_{X,Y}$ is the mass of the new gauge boson

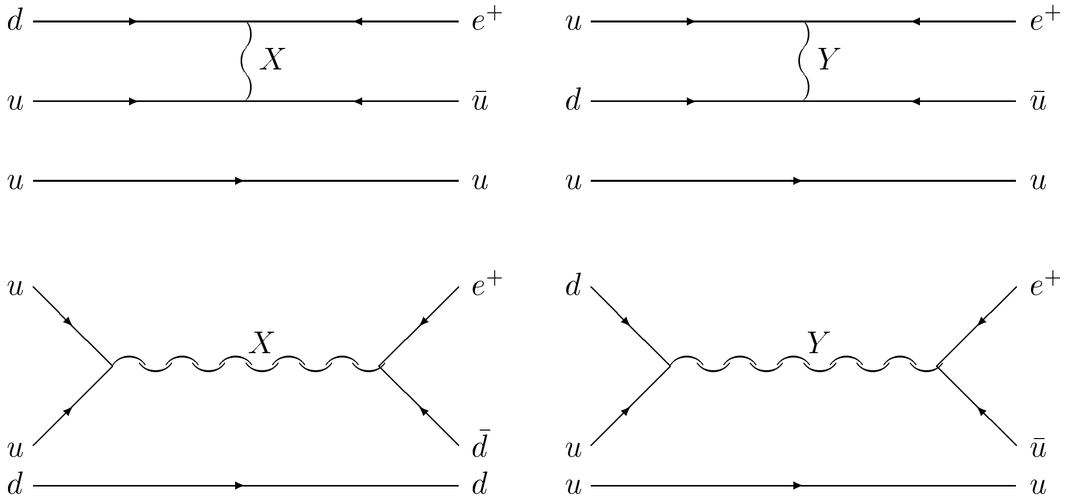

Figure 2.4: Feynman diagrams for the favored proton decay in minimal $SU(5)$, $p \rightarrow e^+\pi^0$.

which is close to the scale of the unification of the coupling constants. To make a prediction for the proton lifetime, $M_{X,Y}$ must be estimated. This is accomplished by using equation 2.10 to estimate the unification scale. The calculation of the b_i's for minimal $SU(5)$ to first order are

$$\begin{aligned} b_3 &= 33 - 4\,n_f \\ b_2 &= 22 - 4\,n_f - \tfrac{1}{2} \\ b_1 &= -4\,n_f - \tfrac{3}{10} \end{aligned} \tag{2.15}$$

where n_f is the number of generations, or families. In the Standard Model there are three families. Using the measured values for the coupling constants α_i, the unification of the coupling constants occurs around $M_X \sim 10^{15}$ GeV and is shown in figure 2.5. This gives a prediction for the proton lifetime into $e^+\pi^0$ of $10^{30\pm1.5}$ years

[11]. In addition to setting the unification scale, a prediction for the weak mixing angle $\sin^2\theta_W$ of 0.215 ± 0.005 is made.

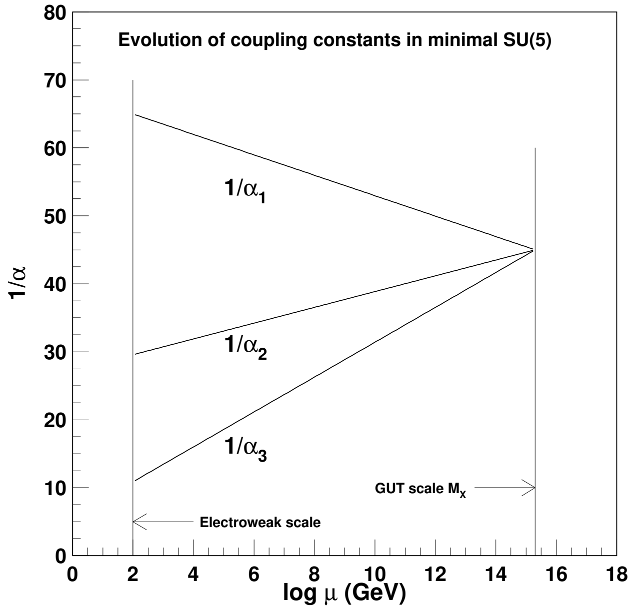

Figure 2.5: Evolution of running coupling constants in Minimal $SU(5)$. Equations 2.10 are solved to yield the unification scale M_X and the weak mixing angle $\sin^2\theta_W$. The α_i $(i = 1, 2, 3)$ denote the couplings for $U(1)_Y$,$SU(2)_L$, and $SU(3)_c$, respectively.

Despite the aesthetically pleasing simplicity of minimal $SU(5)$, experimental observations have excluded it. IMB set a limit of $\tau(p \to e^+\pi^0) > 5.5 \times 10^{32}$ years at the 90% confidence level [12] and Super–Kamiokande has recently increased this to 1.6×10^{33} years (90% C.L.) [13]. In addition, experimental observations reveal a weak mixing angle of 0.232 ± 0.001, a significant deviation from the prediction of 0.215 ± 0.005.

Particle	Spin	Superpartner	Spin
Quark (q)	1/2	“Squark” ($\tilde{q}$)	0
Lepton (l)	1/2	“Slepton” ($\tilde{l}$)	0
Photon (γ)	1	“Photino” ($\tilde{\gamma}$)	1/2
Gluon (g)	1	“Gluino” ($\tilde{g}$)	1/2
W	1	“Wino” ($\tilde{W}$)	1/2
Higgs (H)	0	“Higgsino” ($\tilde{H}$)	1/2

Table 2.4: Standard Model particles and their supersymmetric partners.

2.2.3 Supersymmetric GUTs

When calculating the mass of the electroweak Higgs boson assuming the existence of a GUT, first order radiative corrections depend on the large value of $M_{X,Y}$. This leads to corrections which are naturally much larger than the weak scale. This is called the “hierarchy problem.” One way to reconcile this [14, 15] is to postulate an entirely new spectrum of particles in such a way that for every Standard Model particle there is a corresponding “superpartner.” To effectively cancel the radiative corrections, the contributions from the superpartners must be opposite in sign to their corresponding Standard Model particle. To accomplish this, the superpartners must have a spin which is $\frac{1}{2}$ unit different from the Standard Model partner. This is called “supersymmetry”: for every fermion in the Standard Model there exists a corresponding bosonic partner and for every boson in the Standard Model there exists a corresponding fermionic partner (see table 2.4). Requiring the radiative corrections to the Higgs mass to be manageable sets the scale of the mass difference between partners and superpartners

$$\left| m_{SUSY}^2 - m_{SM}^2 \right| < O(1\,\mathrm{TeV}^2) \tag{2.16}$$

When incorporating the new spectrum of particles into the calculations for the evolution of the running coupling constants, the constants b_i change to

$$\begin{aligned} b_3 &= 27 - 6\,n_f \\ b_2 &= 28 - 6\,n_f - 3 \\ b_1 &= -6\,n_f - \tfrac{9}{5} \end{aligned} \tag{2.17}$$

Putting these into equation 2.10, a larger unification scale is found (figure 2.6). A comparison of the evolution of the couplings in this model incorporating SUSY to the non-SUSY model (figure 2.5) reveals a higher unification scale for the SUSY case by about an order of magnitude. $M_{X,Y}$ is predicted to be about 10^{16} GeV compared to about 10^{15} GeV in the non-SUSY case. Since the decay rate of the proton via the exchange of the X and Y gauge bosons scales as $\sim M_X^{-4}$, the proton lifetime into $e^+\pi^0$ is suppressed by four orders of magnitude in SUSY GUTs compared to the non-SUSY Minimal $SU(5)$. This is consistent with the experimental non-observation of $p \to e^+\pi^0$. In addition, the prediction for $\sin^2\theta_W$ becomes 0.236 ± 0.002 [16] when incorporating SUSY, much closer to the experimental value. Incorporating SUSY then solves three problems encountered in non-SUSY GUTs: the hierarchy problem, the disagreement between prediction and measurement for $\sin^2\theta_W$, and the non-observation of the proton decay $p \to e^+\pi^0$.

Despite the fact that nucleon decay via the exchange of the heavy gauge bosons is suppressed in SUSY GUTs, there are other interactions in the SUSY Lagrangian which can mediate nucleon decay. The type having the most significant contribution is the dimension 5 (d=5) operator via the exchange of the heavy supersymmetric color triplet Higgsino [17, 18, 19]. The Feynman diagram for this interaction is shown in figure 2.7. These operators have the property that transitions from one family in the initial state to the same family in the final state are not allowed. For instance, the

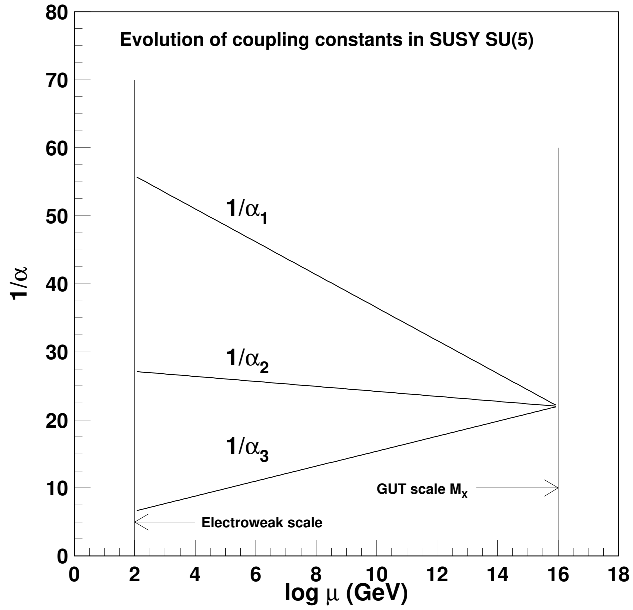

Figure 2.6: Evolution of running coupling constants in SUSY. The couplings merge at a scale about an order of magnitude larger than in minimal $SU(5)$.

proton is composed of quarks from the first family, two "up" quarks and one "down" quark. An interaction via the d=5 operator requires the second or third family to be in the final state. All quarks except a strange quark are kinematically disallowed, meaning that an anti-strange quark must be the final state. The anti-strange quark binds with a spectator u or d quark to form a K meson. The favored decay modes are therefore $p \to \bar{\nu}K^+$ and $n \to \bar{\nu}K^0$ (figure 2.8).

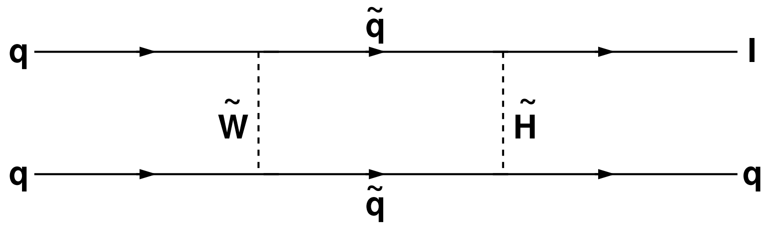

Figure 2.7: The Feynman diagram for d=5 interactions predicted in SUSY GUTs.

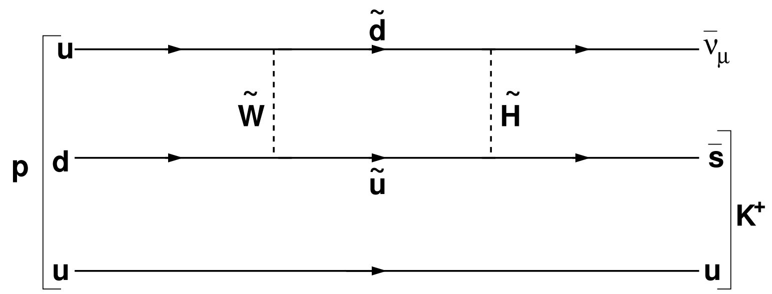

Figure 2.8: Feynman diagram for the favored proton decay in Supersymmetric GUTs, $p \to \bar{\nu}K^+$. For $n \to \bar{\nu}K^0$, replace the spectator u quark with a d quark.

Since the Higgsino is a fermionic propagator, the amplitude contains only one power of the Higgsino mass. Therefore the nucleon lifetime scales as

$$\tau|_{d=5} \sim \lambda \frac{M_{H_X}^2 m_{SUSY}^2}{m_p^5} \tag{2.18}$$

where M_{H_X} is the mass of the heavy color triplet Higgsino, m_p is the proton mass, m_{SUSY} is the scale of SUSY breaking, and λ is a factor which depends on various parameters. The many free parameters in the model allow a wide range of predictions for the nucleon lifetime. Parameters such as the mass of the color triplet Higgsino M_{H_X}, the masses of the various squarks and sleptons, the mass of the Wino, the SUSY breaking scale, CKM mixing factors, and the masses of the electroweak Higgsino doublet all contribute to the calculation. In the minimal SUSY $SU(5)$ GUT [20, 21], the calculation by Hisano, Murayama, and Yanagida [22] yields lifetimes for $p \to \bar{\nu}K^+$ and $n \to \bar{\nu}K^0$ of around $10^{30\pm2}$ years.

Other models have been proposed beyond those based on $SU(5)$. More popular models have been proposed based on an $SO(10)$ symmetry group [23, 24, 25]. $SO(N)$ is the group which describes orthogonal rotations in an N dimensional space. An important feature of $SO(10)$ is that all of the fermions can be contained in a single representation. This is different from $SU(5)$ where the fermions must be broken up into $\bar{\mathbf{5}}$ and $\mathbf{10}$ multiplets. The multiplet for $SO(10)$ is the $\mathbf{16}$ which contains the $\mathbf{10}$ and $\bar{\mathbf{5}}$

$$\mathbf{16} \;=\; \mathbf{10} + \;\bar{\mathbf{5}}\; + \;\mathbf{1} \tag{2.19}$$

Notice that there is an additional singlet $\mathbf{1}$ representation within the $\mathbf{16}$. This provides a place for a right-handed neutrino ν_R which does not exist in the Standard Model or $SU(5)$. A diagram of the $\mathbf{16}$ representation is shown in figure 2.9 (diagram from [26]).

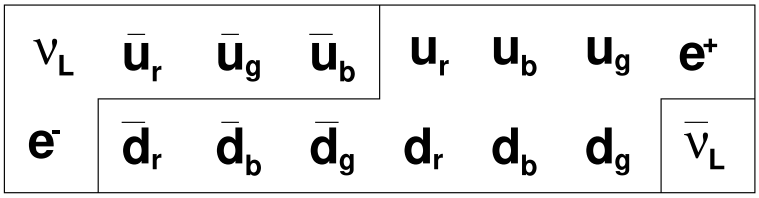

Figure 2.9: $\mathbf{16}$ multiplet in $SO(10)$. The $\bar{\mathbf{5}}$ and $\mathbf{10}$ of $SU(5)$ are contained within the $\mathbf{16}$. In addition, there is a $\mathbf{1}$ which corresponds to a left-handed anti-neutrino, the anti-particle of a right-handed neutrino.

The $SO(10)$ model by Babu, Pati, and Wilczek [27, 24] has drawn attention in light of the recent evidence for neutrino mass from Super–Kamiokande [28, 29]. Neutrino mass fits nicely into the $SO(10)$ group structure on which this model is based. This theory is based on early ideas by Pati and Salam [30, 31] which introduced the group $G(224)$ which is shorthand for the left-right symmetric group $SU(2)_L \times SU(2)_R \times SU(4)_c$. The features which distinguish this model from the Standard Model are the existence of a right-handed $SU(2)_R$ group and a $SU(4)_c$ of "extended color" instead of $SU(3)_c$. The idea of extended color is that in addition to the three colors from $SU(3)_c$ in the Standard Model, there is an additional color for the leptons. The existence of the $SU(2)_R$ provides a place for the right-handed neutrino. A picture of $G(224)$ is shown in figure 2.10 (diagram from [26]).

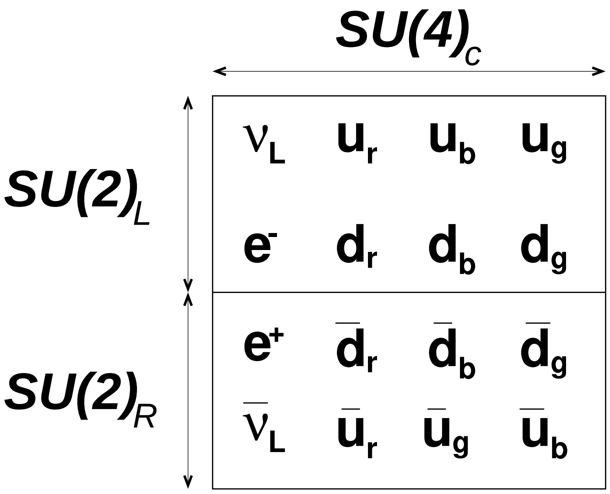

Figure 2.10: Structure of the Pati-Salam right-left symmetric $G(224)$ which is based on a $SU(2)_L \times SU(2)_R \times SU(4)_c$ symmetry. This model provides a place for a right-handed neutrino.

An important feature of this theory is that to generate neutrino masses the existence of a new set of color triplet fields is required. These fields generate a new set of d=5 operators which predict comparable rates for $p \to \bar{\nu} K^+$ and $p \to \mu^+ K^0$ of

$$\Gamma(p \to \mu^+ K^0) \approx (20\% \text{ to } 50\%)\, \Gamma\left(p \to \bar{\nu}_\mu K^+\right) \tag{2.20}$$

Using the Super–Kamiokande measurement for the mass difference squared Δm^2 [29, 28] between the two neutrino mass eigenstates as an input parameter, a proton lifetime of no more than about 5×10^{33} years [32] into $p \to \bar{\nu} K^+$ is predicted. This is within the observable range of Super–Kamiokande.

In conclusion, a few models and their predictions are summarized in table 2.5.

Model	**Authors**	**Modes**	τ_N (years)
Minimal $SU(5)$	Georgi and Glashow [11]	$p \to e^+\pi^0$	$\sim 10^{30}$
Minimal SUSY $SU(5)$	Dimopoulos and Georgi [20], Sakai[18] Lifetime Calculations: Hisano, Murayama, and Yanagida [22]	$p \to \bar{\nu}K^+$ $n \to \bar{\nu}K^0$	10^{28} to 10^{32}
SUGRA $SU(5)$	Nath and Arnowitt [33, 34]	$p \to \bar{\nu}K^+$	10^{32} to 10^{34}
SUSY $SO(10)$ with anomalous flavor $U(1)$	Shafi and Tavartkiladze [25]	$p \to \bar{\nu}K^+$ $n \to \bar{\nu}K^0$ $p \to \mu^+K^0$	10^{32} to 10^{35}
SUSY $SO(10)$	Lucas and Raby [23]	$p \to \bar{\nu}K^+$ $n \to \bar{\nu}K^0$	10^{33} to 10^{34} (p) 10^{32} to 10^{33} (n)
SUSY $SO(10)$ with $G(224)$, ν mass	Babu, Pati, and Wilczek [27, 24, 32]	$p \to \bar{\nu}K^+$ $n \to \bar{\nu}K^0$ $p \to \mu^+K^0$	$< 10^{34}$

Table 2.5: Summary of selected Grand Unified Theories and their predictions for nucleon decay.

Chapter 3

Experiments

The experimental search for nucleon decay began long before the idea of Grand Unified Theories. Instead of GUTs, the motivation for early experiments was to test baryon number conservation. It wasn't until the late 1970s that experiments were proposed which would search specifically for nucleon decay predicted by GUTs. Around this time the $SU(3) \times SU(2) \times U(1)$ structure of the Standard Model was beginning to be accepted and it became feasible that minimal $SU(5)$ was indeed the "theory of everything." If this were the case, the proton should decay via $p \rightarrow e^+\pi^0$ with a lifetime of $10^{30\pm1.5}$. In the early 1980s tracking calorimeters began to turn on to search directly for proton decay followed a couple of years later by the more massive water Cherenkov detectors.

Because the lifetimes of the proton and bound neutron are expected to be extremely long, it is important that nucleon decay experiments observe a large number of nucleons for a sufficient amount of time to achieve the desired sensitivity to the long nucleon lifetime. In addition, it is important that the detectors are able to detect nucleon decay events efficiently. In general nucleon decay experiments are divided into two categories: indirect and direct detection. Indirect detection methods are insensitive to the particular nucleon decay mode while direct detections methods search for decay products from the nucleon decay in real time. To reduce background induced by cosmic ray muons which are the result of primary cosmic rays striking the upper atmosphere, direct detection nucleon decay experiments are typically placed at significant depths below the surface of the earth.

3.1 Early Experiments

Radiochemical and geochemical methods were initially used to search for nucleon decay [35]. These methods searched for daughter nuclei which could be the result of the decay of a nucleon within a sample of parent nuclei. For this reason they are designated as indirect detection. The virtue of these types of experiments is their insensitivity to the particular decay mode into which the nucleon decays. The basic idea of radiochemical experiments is that a nucleon decay within a heavy parent nucleus can leave a hole in the residual nucleus which can induce spontaneous fission. A search for the resulting nuclei from the fission reaction is then performed. Geochemical methods assemble a pure sample of nuclei and periodically search it for rare isotopes which might be the result of the decay of one of the nucleons in the nucleus. Since there are modest limits to the quantity of a sample which can be assembled and searched, these methods could only reach nucleon lifetime sensitivities of $\sim 10^{26}$ years. A summary of various radiochemical and geochemical experiments is shown in table 3.1 [36].

The first direct detection experiment was by Reines, Cowan, and Goldhaber in the 1950s using a detector designed to detect neutrinos [37]. It was 60 meters underground and was made of 300 liters of liquid scintillator. In addition to detecting neutrinos, the large source of nucleons in the detector made it possible to also test

Method	nucleon lifetime	Authors
Spontaneous fission ^{232}Th	10^{23} years	Flerov *et al.* [43]
^{129}Xe$\rightarrow$^{128}Xe	10^{25} years	J.C. Evans and R.I. Steinberg [44]
^{39}K$\rightarrow$^{38}K or ^{38}Ar	10^{26} years	R.I. Steinberg and J.C. Evans [45]

Table 3.1: Summary of indirect detection methods .

baryon number conservation. The test was quite crude: the count rate was checked for an excess over the expectation from cosmic ray muons resulting in a limit on the proton lifetime of 10^{22} years. The liquid scintillator method was improved over the years [38, 39, 40, 41] culminating in a total nucleon lifetime calculated by Learned, Reines, and Soni in 1979 of $\tau_p > 10^{30}$ years at the 90% confidence level [42].

3.2 Iron calorimeter

With the hope that the rate of proton decay via $p \rightarrow e^+\pi^0$ fell in the middle of the range predicted by minimal $SU(5)$, the first iron calorimeters were designed to have a sensitivity of nucleon lifetimes up to about 10^{31} years. The second wave detectors had larger mass and therefore sensitivity to longer lifetimes. Iron calorimeters search directly for the decay products of the nucleon and are typically composed of iron plates, which serve as a source of nucleons, interspersed with detectors which track particles traversing the detector. The virtue of iron calorimeters is their excellent tracking resolution. The drawback is that instrumentation of iron is expensive, resulting in a high cost per kiloton. Also, nuclear effects on the daughter particles from a nucleon decay are more complicated and prominent in iron compared to oxygen. Table 3.2 summarizes the characteristics of various iron calorimeters.

3.2.1 Soudan (1981-1990)

The first Soudan detector was situated in the Soudan mine which is located in northern Minnesota. The detector was composed of 432 concrete slabs each having 8 proportional tubes. The concrete served as the source of nucleons and was loaded with taconite concentrate resulting in a concentration of 57% iron, 29% oxygen, 13% calcium, and 1.2% hydrogen. The detector was located at about 2000 meters water equivalent (m.w.e.) below the surface of the earth and had a total mass of 31.4 metric-tons. Nucleon decay was not observed by Soudan and they set a limit on the proton lifetime via $p \rightarrow e^{+}\pi^{0}$ of 1.3×10^{30} years [46].

3.2.2 KGF (1980-1992)

The Kolar Gold Field (KGF) nucleon decay experiment was located in the Kolar Gold Mines in India [47]. The detector had 34 layers of alternating 12-mm thick iron plates interspersed with 10 cm $\times$ 10 cm proportional counters. Its total mass was 0.140 kilotons and it was placed extremely deep underground at a depth of m.w.e. in order to significantly reduce the background from cosmic-ray muons.

Excitement came in the early 1980s when KGF reported an anomaly in their data which they interpreted to be caused by nucleon decays [47, 48]. The non-observation of nucleon decay from every other experiment at the time refuted this claim. Based on the number of observed events they estimated the nucleon lifetime to be $\tau_N \sim 6 \times 10^{30}$ years. If this were the case, Super–Kamiokande would be expected to see several hundreds of events from nucleon decay after 1-2 years of livetime.

3.2.3 NUSEX (1982-1988)

The NUcleon Stability EXperiment (NUSEX) was located at a depth of 4800 m.w.e. beneath Mont Blanc in a highway tunnel connecting Italy and France [49]. The detector consisted of a sandwich of 134 layers of alternating 1 cm $\times$ 3.5 m $\times$ 3.5 m iron plates and streamer tubes of cross-section of 9 mm$\times$9 mm. The total mass of the detector was 0.150 kiloton.

3.2.4 Frejus (1984-1988)

The Frejus nucleon decay detector was located in the Frejus highway connecting Modane, France to Bardonecchia, Italy [50]. It consisted of 912 layers of 3-mm thick iron plates and flash tubes with 5 mm $\times$ 5 mm cross-section. Every 8 layers there was a layer of Geiger tubes which provided a trigger for the flash tubes. Because of the long readout time of the flash tubes (2-3 seconds), the rate of cosmic ray muons crossing the detector had to be small to minimize deadtime. This was achieved by placing it at a depth of 4800 m.w.e. resulting in a muon rate of about 20 per hour. The mass of the detector was 0.9 kilotons.

3.2.5 Soudan 2 (1988-Present)

The Soudan 2 detector [51] is a larger version of the first Soudan detector [46]. This iron calorimeter is located in the Soudan iron mine in Northern Minnesota and has a total mass of 0.974 kiloton. It is composed of 224 (2.7 m $\times$ 1.0 m $\times$ 1.2 m) modules each of which is made of drift tubes layers interspersed with iron sheets. A cross-sectional view of a module reveals a “honeycomb”-like structure. A virtue of Soudan 2 is that the K^+ from $p \to \bar{\nu} K^+$ can be detected directly. This is because it is highly ionizing and can therefore be tracked in the detector. The tracks of the subsequent

Detector	mass (kiloton)	exposure (kton·year)	depth (m.w.e.)	nucleon lifetime sensitivity (years)
KGF	0.140	0.126 [48]	6800	10^{30} to 10^{31}
NUSEX	0.150	0.130 [52]	5200	10^{30} to 10^{31}
Frejus	0.9	2.0 [53]	4800	10^{31} to 10^{32}
Soudan 1	0.031	0.3 [46]	2000	10^{30}
Soudan 2	0.974	4.4 [54]	2000	10^{31} to 10^{32}

Table 3.2: Summary of various parameters of Iron Calorimeters.

decay products can be seen where the K^+ stops. Being able to directly detect the K^+ and its decay provides very powerful background rejection criteria.

3.3 Water Cherenkov detectors

Water Cherenkov detectors use Cherenkov radiation, an optical shock wave produced by charged particles traveling faster than the speed of light in the medium (section 4.1.1), to track charged particles passing through the detector. These detectors are tanks of water instrumented with photomultiplier tubes (PMTs) which detect the flashes of Cherenkov light. The water therefore serves as both the source of nucleons and the tracking medium. Due to the relatively low cost of water, these detectors can have a large mass, making them sensitive to longer proton lifetimes than iron calorimeter experiments. In addition, timing information can be obtained from the PMT pulses. A summary of various water Cherenkov detectors is in Table 3.3.

3.3.1 IMB/IMB-3 (1982-1991)

Located in the Fairport salt mine close to Cleveland, Ohio, the Irvine Michigan Brookhaven (IMB) water Cherenkov detector was designed to cover the entire lifetime range of the proton decay $p \to e^+\pi^0$ predicted by minimal $SU(5)$[55]. To achieve a sensitivity to the partial lifetime predicted by $SU(5)$ [11] which is $\tau/B|_{p\to e^+\pi^0} = 4.5\times10^{(29\pm1.7)}$ years, it had a 3.3 kiloton fiducial mass (corresponding to $\sim 10^{33}$ protons) with a cubical shape (18 m $\times$ 17 m $\times$ 22.5 m). It operated in three different operation modes, the second having very brief duration. The major difference between the first and third phases was an upgrade in which the 2048 13-cm PMTs were replaced with 20-cm PMTs equipped with wavelength-shifter plates to increase light collection efficiency [56]. These PMTs and wavelength-shifters are now used in the outer detector of Super–Kamiokande. Although it did not observe proton decay, IMB had some triumphs which include observation of neutrinos from Supernova 1987A concurrent with Kamiokande and the first hints of a deficit of muon neutrinos in the sample of atmospheric neutrinos.

3.3.2 Kamiokande (1983-1988)

Kamiokande was the predecessor to Super–Kamiokande. It was located about 200 m away from the present location of Super–Kamiokande in the Mozumi mine of the Kamioka Mining and Smelting company in Gifu Prefecture, Japan. A smaller version of Super–Kamiokande, Kamiokande was a cylindrical tank with total mass of 3 kilotons. It was instrumented with 948 50-cm diameter PMTs viewing a fiducial mass of 1 kiloton yielding a photocathode coverage of 20%. This large photocathode coverage increased the sensitivity of Kamiokande to nucleon decay modes with lower Cherenkov light yields, such as $p \to \bar{\nu}K^+$.

Operation consisted of two phases, Kamiokande I (1983-84) and Kamiokande II (1986-88). The upgrade to Kamiokande II was designed to detect low-energy solar neutrinos and consisted of three major changes. The first was the installation of an anti-counter used to veto incoming particles. This anti-counter was a water

Cherenkov detector which surrounded the inner detector and was instrumented with 123 PMTs. The second part of the upgrade was an improved water purification system to remove the background from radon gas. Finally, a new electronics system was installed which made it possible to make multi-hit time and charge measurements.

Like IMB, Kamiokande did not observe nucleon decay, but did produce significant scientific discoveries. Observation of neutrinos from Supernova 1987A, observation of a deficit of solar-neutrinos in the energy range of about 10 to 20 MeV, and the first signs of a distortion in the zenith angle distribution of atmospheric neutrinos were all very important advances in the field of neutrino physics. Although data analysis stopped in 1988, Kamiokande remained alive until 1997 in order to detect neutrino signals from stellar collapse.

3.3.3 HPW (1983-1984)

The Harvard-Purdue-Wisconsin (HPW) water Cherenkov detector was located in a mine near Park City Utah at a depth of about 1500 m.w.e [57]. Unlike other water Cherenkov detectors which have PMTs mounted on the walls of the detector, its 700 PMTs were mounted on vertical strings of hoops suspended in a cylindrical tank of water which had a mass of 0.7 kilotons. The walls were lined with mirrors to increase light detection efficiency. The combination of the 3-d spacing of PMTs and the mirrors made it difficult to track particles, so they were only able to quote limits based on the number of electrons from muon decays. For example, the decay $p \to \nu K^+$; $K^+ \to \pi^+\pi^+\pi^-$ would have two decay electrons from the decay of the π^+s to μ^+s.

Detector	mass (fiducial) (in kilotons)	exposure (kton·years)	depth (m.w.e)	nucleon lifetime sensitivity (years)
HPW	.680 (.130/.180)	0.2 [57]	1500	10^{30}
Kamiokande (I/II)	3.0	3.76 [58]	2700	10^{31} to 10^{32}
IMB/IMB-3	8.0 (3.3)	7.6 [12]	1600	10^{31} to 10^{32}
Super–Kamiokande	50 (22.5)	-	2700	10^{32} to 10^{34}

Table 3.3: Summary of Water Cherenkov Detectors

3.3.4 Super–Kamiokande (1996-Present)

Super–Kamiokande is a massive 50 kiloton water Cherenkov detector with a fiducial mass of 22.5 kilotons. Its large mass provides a sensitivity to longer proton lifetimes. In addition, the 11146 50-cm PMTs viewing the inner detector provide 40% photocathode coverage. This large coverage makes it possible to efficiently track particles traversing the detector. Particles can be distinguished efficiently between showering particles from electrons or gamma-rays and non-showering particles like muons, pions, or protons. The large coverage also provides an enhanced ability to reconstruct multiple tracks in events with many particles. It is also possible to detect showering particles having energies as low as about 5 MeV. This is important when detecting the nuclear de-excitation gamma-rays which can be produced when a nucleon in O^{16} decays.

Data taking began in April 1996 and the detector has been running with an integrated livetime of about 80% since then. More details of Super–Kamiokande appear in Chapter 4.

Chapter 4

The Super–Kamiokande Detector

4.1 General

Super–Kamiokande is located in the Mozumi mine of the Kamioka Mining and Smelting Company in Gifu Prefecture, Japan. It sits at a depth of about 1000 meters (2700 meters water equivalent) below the peak of Mount Ikenoyama. This shielding attenuates the constant rain of cosmic ray muons by about five orders of magnitude, which results in a muon detection rate of about 2 Hz. The total mass of 50 kilotons makes it the largest underground water Cherenkov detector to date.

4.1.1 Water Cherenkov Detector

When a charged particle travels faster than the speed of light in a medium, the electromagnetic waves it emits form a coherent shock front known as Cherenkov radiation (figure 4.1) [59]. This radiation is emitted in a conical shape with angle relative to the direction of movement of the particle (θ_C) given by

$$\cos\theta_C = \frac{1}{n\beta} \tag{4.1}$$

where n is the index of refraction of the medium and $\beta = v/c$ is the velocity of the particle relative to the speed of light.

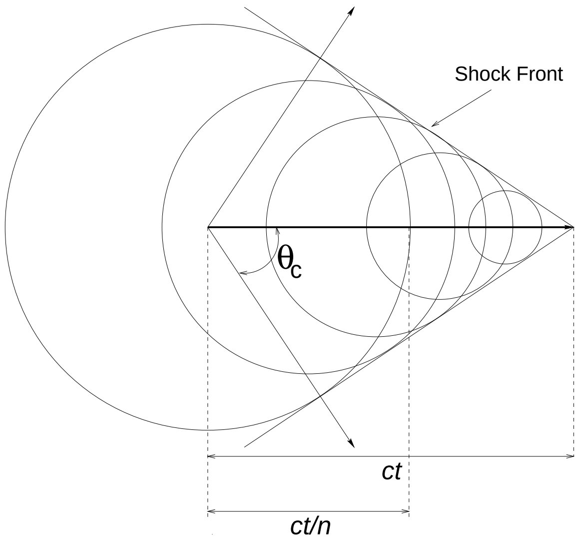

Figure 4.1: Illustration of Cherenkov radiation.

The number of photons (N) emitted per unit path length (dx) per unit wavelength $(d\lambda)$ is

$$\frac{d^2N}{d\lambda dx} = \frac{2\pi\alpha}{\lambda^2}\left(1 - \frac{1}{\beta^2 n^2(\lambda)}\right) \tag{4.2}$$

where $\alpha \approx \frac{1}{137}$ is the fine structure constant. In the wavelength range where the PMTs of Super–Kamiokande are sensitive ($\sim$ 300-600 nm), a particle moving at $\beta = 1$ will emit about 300 photons/cm. The cone of Cherenkov light emitted by the particle will project onto the PMT lined wall of Super–Kamiokande creating a circular pattern on the wall. Various kinematic variables such as momentum, energy, and direction of particles traversing the detector are reconstructed on the basis of these patterns.

4.1.2 Structure

Super–Kamiokande is a cylindrical stainless steel water tank with a height of 41.4 m and a diameter of 39.3 m (figure 4.2). The detector is optically separated into two regions, the inner and outer detectors (ID and OD). The ID has a diameter of 33.8 m and a height of 36.2 m and is lined with 11,146 inward facing 50-cm diameter PMTs covering 40% of the surface. The OD completely surrounds the ID with a thickness of 2.6 to 2.75 m and is lined with 1885 outward facing 20-cm diameter PMTs recycled from the IMB detector. These PMTs are equipped with 60 cm $\times$ 60 cm wavelength-shifter plates to increase the light detection efficiency [56]. By Fall 1996, the death rate of the PMTs had stabilized to one every 11 days for the OD and one every 20 days for the ID. The total number of dead PMTs as of December 1999 were 154 and 216 for the ID and OD, respectively.

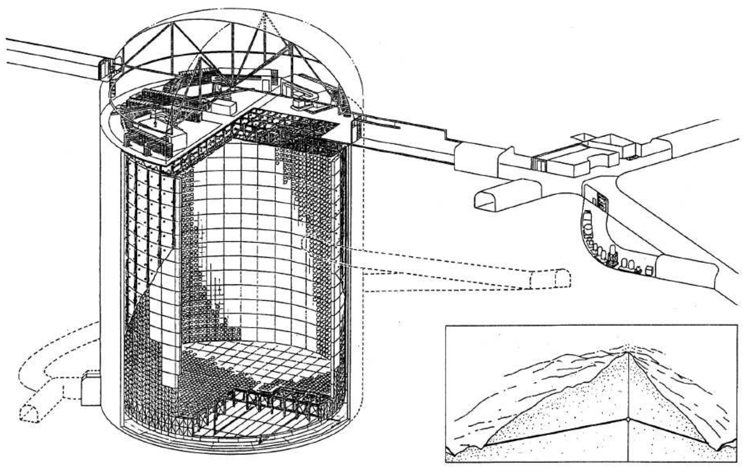

Figure 4.2: Schematic of the Super–Kamiokande detector.

The ID and OD are separated by a 55-cm thick PMT support structure composed of about 1000 "super modules," each of which supports 12 50-cm ID PMTs and 2

OD 20-cm PMTs (figure 4.3).

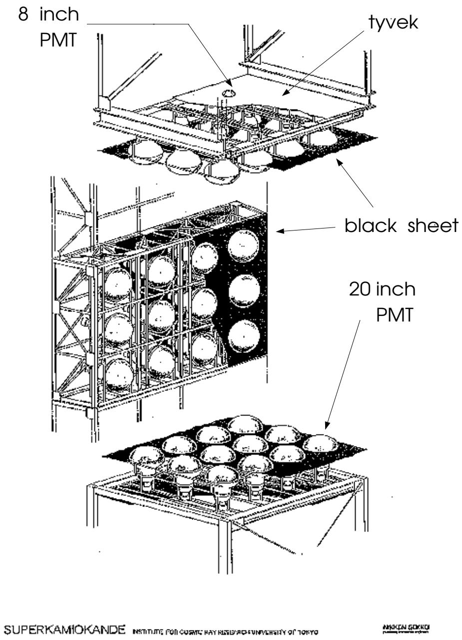

Figure 4.3: Schematic of a supermodule.

In order to optically separate the ID and OD, the side of each super module facing the inner detector is lined with a black plastic sheet. The side of the structure facing the OD is lined with Tyvek, a reflective material which also increases the light detection efficiency of the OD.

On top of the water tank are five electronics huts, calibration devices including an electron LINAC, and hundreds of kilometers of cables connecting the PMTs to the electronics. About 100 m from the top of the water tank is a control room where physicists monitor the many different processes related to data taking.

4.1.3 Water Purification System

The main purposes of the water purification system in Super–Kamiokande (figure 4.4) are to decrease the light attenuation and to remove radioactive impurities such as radon gas. Radon decays are a major background in the low energy analysis but do not contribute significantly to nucleon decay analyses.

Water is initially circulated through a filter which removes dust with size $\sim$1 μm. It is then passed through stages to remove metal ions, bacteria, and any remaining oxygen or radon gases. Finally, the water is passed through "ultra-filters" which remove smaller particles with size $\sim$100 nm. The resulting attenuation length of the water is about 100 m for 450 nm wavelength photons.

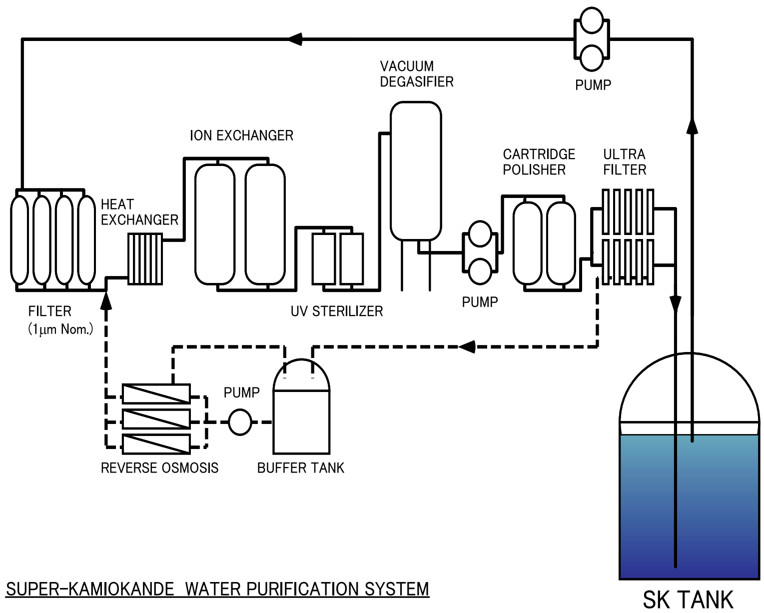

Figure 4.4: Water purification system.

4.2 Inner Detector Electronics

4.2.1 Photomultiplier Tubes

The 50-cm diameter photomultiplier tubes (PMTs) used in Super–Kamiokande were originally designed for the Kamiokande detector by HAMAMATSU Corporation [60].

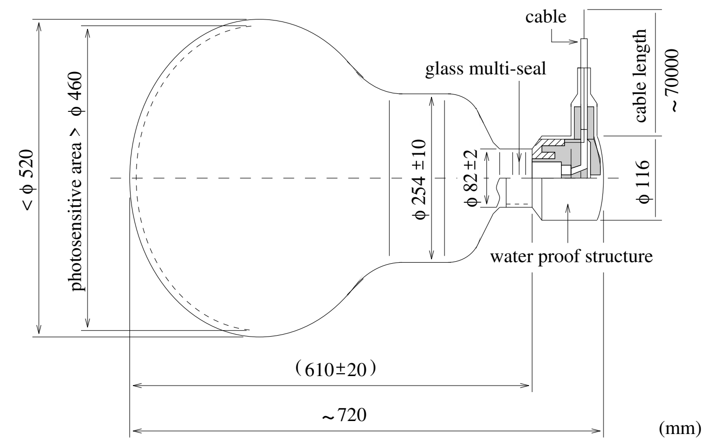

Figure 4.5: Schematic view of a 50-cm diameter photomultiplier tube used in Super–Kamiokande.

A schematic of the PMT is shown in figure 4.5. They were designed to have large photosensitive area, good timing resolution, ability to detect single photoelectrons, and stability over a long period of time. In order to have sufficient precision in vertex and direction reconstruction in the low-energy solar neutrino analysis, improvements in timing and energy resolution at the 1 photoelectron (PE) level were required. This was achieved by making changes in the "Venetian blind" dynode structure [61]. The timing resolution was reduced to $\sim$2.5 ns. Furthermore, a clear single photoelectron peak can be distinguished from dark noise (figure 5.3). The quantum efficiency has a maximum of 22% at 390 nm wavelength and is significant in the range of $\sim$300-600 nm (figure 4.6). Some parameters of PMTs are outlined in table 4.1.

Magnetic fields affect the response of PMTs making it necessary to compensate for the geomagnetic field of 450 mG at the Super–Kamiokande site. A system of 26 Helmholtz coils was constructed around the detector to account for this effect reducing the magnetic field to approximately 50 mG.

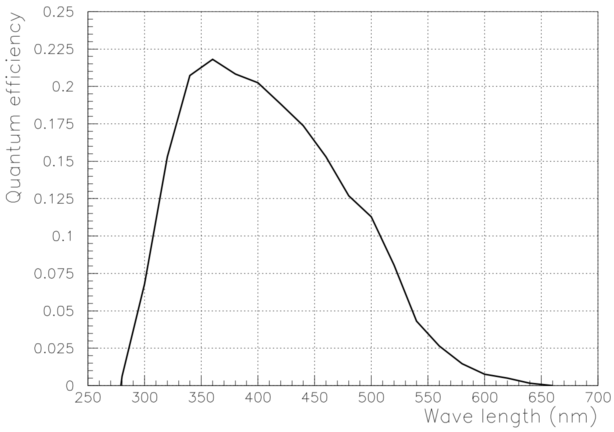

Figure 4.6: 50-cm photomultiplier tube quantum efficiency as a function of photon wavelength.

Diameter	50 cm
Dynode Structure	11 stage Venetian Blind
Gain	10^7 at 2 kV
Quantum efficiency	22% at 390 nm
Mean Transit time	100 ns
Timing Resolution	2.5 ns
Dark Noise Rate	$\sim$ 3 kHz at .25 PE level

Table 4.1: 50-cm PMT characteristics.

4.2.2 Front End Electronics

Analog Timing Modules (ATMs) are used to process the analog signals from the PMTs. These modules are equipped with two channels which enable them to store two successive pulses from a PMT [62]. This makes it possible to detect electrons from muon decays and to handle high rate situations such as supernovae. Each channel consists of a time to amplitude converter (TAC) to record timing information and a charge to analog converter (QAC) to record the size of the PMT pulse. The full time range is 1.6 μs with a timing resolution of 0.3 ns and the charge saturation level is 600 pC, corresponding to about 300 PE, with a resolution of 0.2 pC.

The ATM modules are part of a TKO (Tristan KEK Online) system. In each of four electronics huts on the detector, there are 12 TKO crates. A TKO crate consists of 20 ATMs, a GONG (GO NoGo) trigger control module, and a SCH (Super Control Header). The SCH provides an interface between the TKO crate and its corresponding SMP (Super Memory Partner) residing in a VME crate in the electronics hut. This SMP acts as a buffer for data before being read out to online computer workstations. There are two workstations, each handling 6 SMP modules, in each of the four electronics huts. A schematic of the system is shown in figure 4.7.

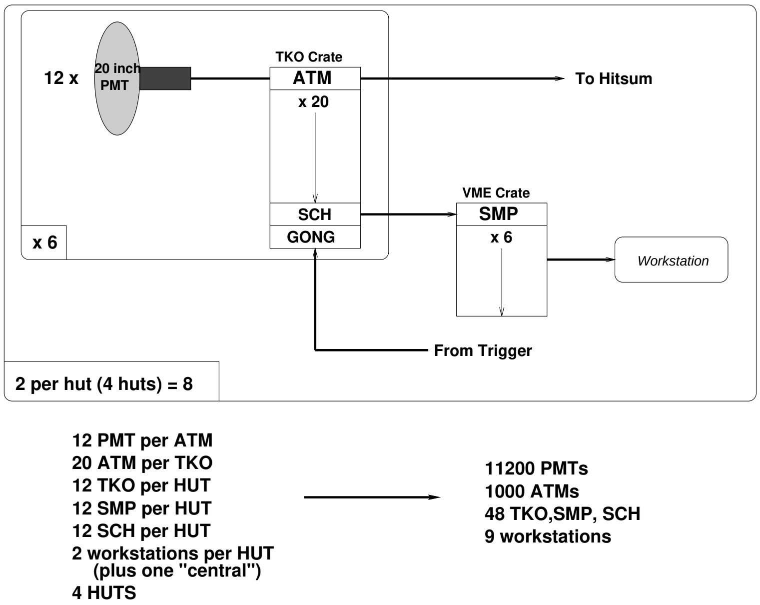

Figure 4.7: Layout of the ID electronics

4.2.3 Trigger

In the ATM module, PMT signals are amplified by a factor of 100 and are sent to a discriminator set at a threshold corresponding to ∼0.2 PE. If the signal exceeds this threshold a rectangular pulse with a width of 200 ns and amplitude of -15 mV is sent

Trigger type	Threshold	N_{hit}	Energy	Rate
Low Energy	320 mV	29	5 MeV	11 Hz
Super Low Energy	222 mV	20	3.5 MeV	550 Hz
High Energy	340 mV	31	6 MeV	6 Hz
Outer Detector	-	19	N/A	3 Hz

Table 4.2: Trigger types

to a summing circuit. The output of this summing circuit is called a HITSUM. The HITSUMs from each of the four huts are sent to the central hut to another summing circuit and a final HITSUM for the entire detector is generated. The trigger is based on thresholds set on the final HITSUM output

The discriminator threshold for the final HITSUM varies depending on the four trigger types, high energy (HE), low energy (LE), super-low energy (SLE), and outer detector trigger (explained later). The HE trigger, which is required for all events caused by atmospheric neutrinos and proton decays, is the most pertinent for this dissertation. The LE and SLE triggers are important for the solar neutrino analysis. Table 4.2 summarizes the different triggers. The high and low energy trigger rates as a function of elapsed time since data taking started on April 1, 1996 are shown in figure 4.8.

4.3 Outer Detector Electronics

The OD electronics consists of 1885 20-cm PMTs which are fed to the front end electronics charge to time converters (QTCs) via paddle cards. One paddle card serves twelve PMTs. The output of the QTCs is sent to time-to-digital converters (TDCs) which are read out with the aid of dual-port memory modules in a VME crate controlled by a Sun workstation. A box diagram of the OD electronics is shown

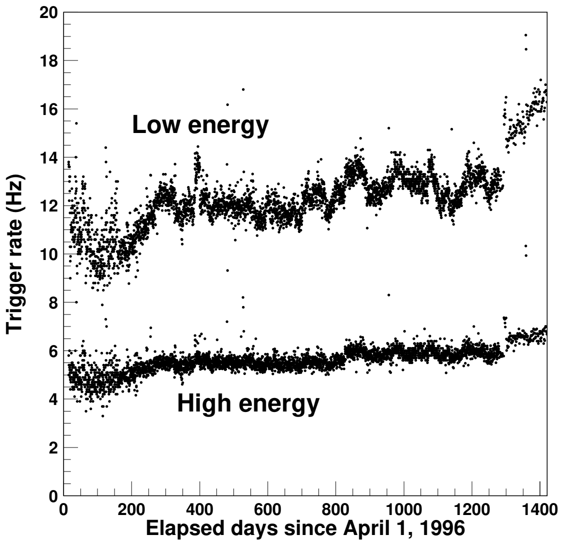

Figure 4.8: High and low energy trigger rate as a function of elapsed days since the start of data taking on April 1, 1996.

in figure 4.9.

4.3.1 Photomultiplier Tubes

The 1800 20-cm diameter OD PMTs were recycled from the IMB detector. The PMTs are optically coupled to 60-cm × 60-cm × 1-cm wavelength-shifter plates which are acrylic doped with bis-MSB [56]. The bis-MSB absorbs Cherenkov photons in the near ultraviolet region of the spectrum where the flux is larger and re-emits photons in the blue-green region where the PMTs are most sensitive. The wavelength-shifter plates reduce the timing resolution from ∼10 ns to ∼15 ns but increases the light collection efficiency by ∼60%. The reduction in timing resolution does not significantly affect the ability of the OD to veto events and is a small price to pay for the increase in light collection.

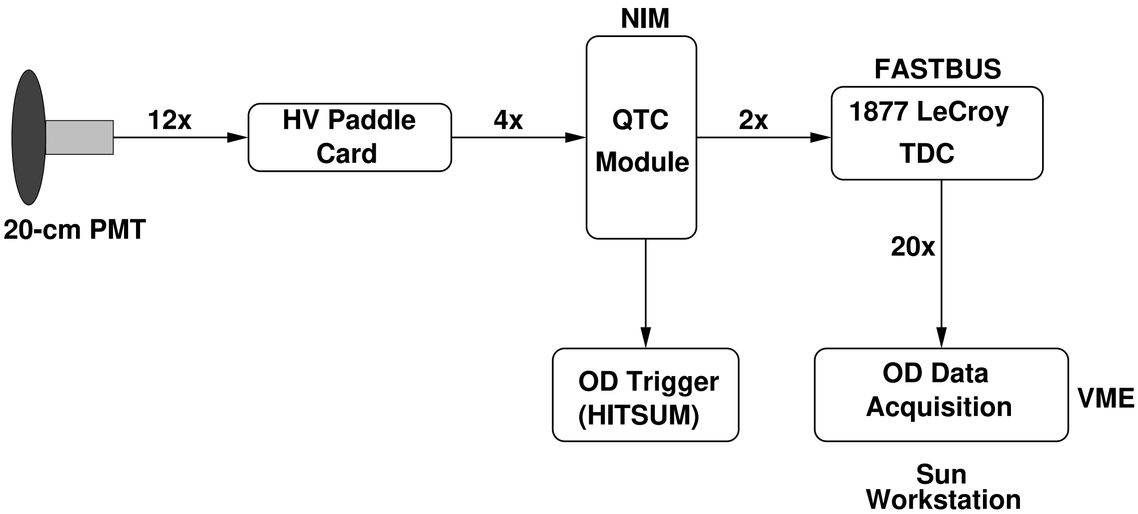

Figure 4.9: Block diagram of OD electronics.

4.3.2 Front End Electronics: QTC modules

The QTC (charge-to-time converter) modules which compose the front end electronics of the OD were designed, built, and tested at Boston University. The QTC modules are self-gated charge integrators which encode timing information in the rising edge of the output pulse and charge information in the width of the pulse. Each QTC module, composed of 3 "mothercards" each serving 16 "daughter" cards, supports 48 channels. There are 10 QTC modules residing in two NIM crates in each of the four electronics huts.

A box diagram of a single QTC channel is shown in figure 4.10. A pulse from the 20-cm PMT is sent through a discriminator with threshold of about 0.25 PE. Pulses over threshold trigger the circuit generating a 200-ns gate which is used as the integrating window for the LeCroy MQT200 charge-to-time converter chip. The PMT pulse is also sent to the LeCroy MQT200 chip and integrated within the 200-ns gate. Finally, the output pulse from the LeCroy MQT200 is discriminated and sent to the CE16V8 PAL. The PAL (programmable array logic) chip converts the pulse

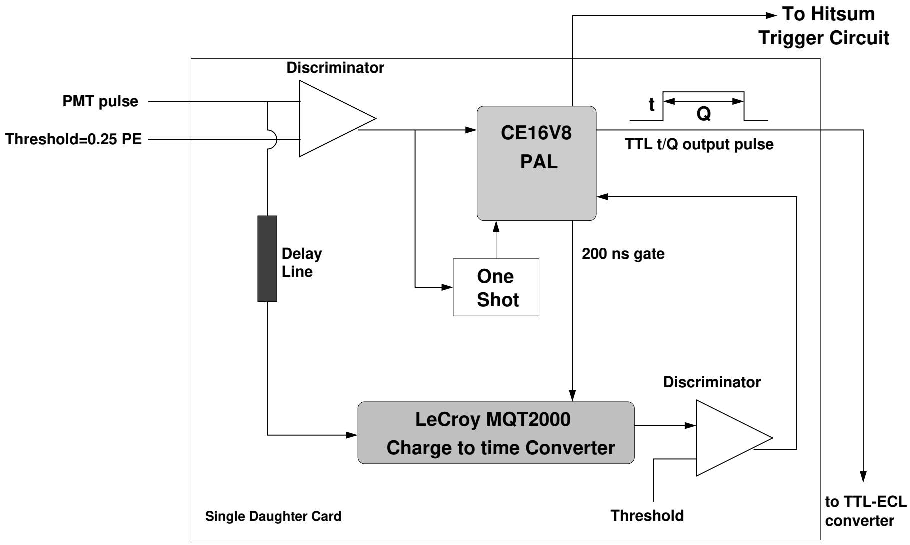

Figure 4.10: Block diagram for a single channel (or "daughter" card) of a QTC module.

to TTL output and provides the logic for the rising edge of the final daughter card output. Cartoon oscilloscope traces for various stages of the circuit are shown in figure 4.11.

4.3.3 Trigger

In addition to encoding charge and timing information from the PMTs, the QTCs generate the trigger for the OD. A single 200-ns width 25-mV square pulse is generated for PMT signals which are above the initial discriminator threshold of 0.25 PE. Each QTC module generates a HITSUM by summing these pulses. The HITSUMs from the individual QTC modules are sent to the central hut where they are summed. This final sum is a global HITSUM. The OD is triggered when there are 19 or more hits within a 200-ns time window. The OD trigger rate is about 3 Hz.

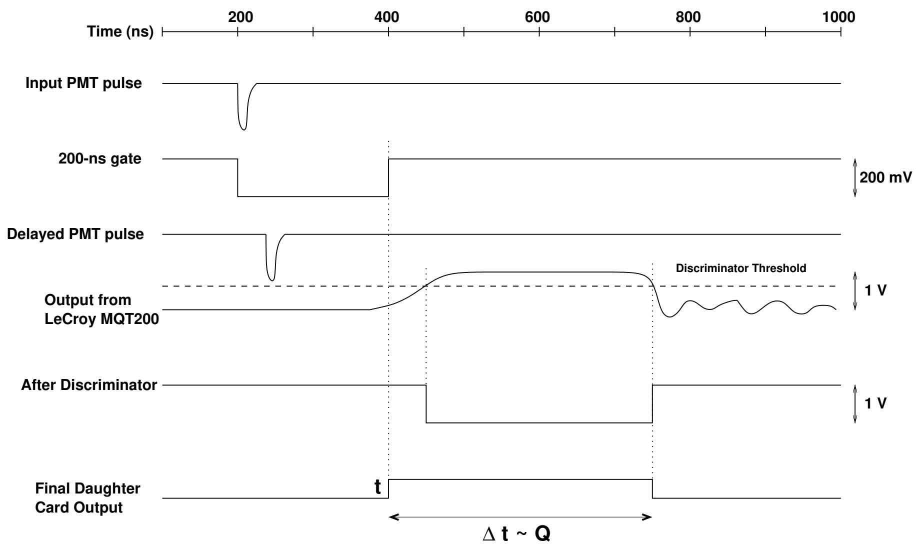

Figure 4.11: Cartoon of scope traces for different stages in a single QTC channel.

4.3.4 Data Acquisition

The ECL output of the QTC modules is sent to a LeCroy 1877 Time-to-Digital converter (TDC). Each quadrant hut houses five 1877 modules which are contained in a single FASTBUS crate. Each TDC channel can digitize a maximum of 16 pulse edges in a window of up to 32 μs. Each QTC output pulse has two edges, meaning that each channel can digitize a maximum of 8 hits in 32 μs. Digitization takes anywhere between 2 to 5 μs. More details of the OD DAQ may be found in reference [63].

The width of the digitization window and its location relation to trigger time can be adjusted. At the start of detector operation the full width of 32 μs was used with the detector trigger centered in the window. The width was reduced to 16 μs with the detector trigger occurring 10 μs into the window in September 1996. This smaller window reduced the amount of data from the OD and helped solve the problem of after-pulses overriding real pulses.

Chapter 5

Calibration

5.1 Relative Gain

The relative gains of individual PMTs are calibrated with the aid of the Xe ball setup shown in figure 5.1. A Xe flash lamp generates UV light which is passed via optical fiber to a scintillator ball in the detector. The scintillator shifts the UV light to visible and diffuses it throughout the detector. The output spectrum peaks at about 440 nm. The relative gain of the i-th PMT is given by

$$G_i = \frac{1}{f(\theta_i)} \frac{Q_i}{Q_0} r_i^2 \exp\left(\frac{r_i}{L}\right) \tag{5.1}$$

where Q_i is the charge detected at the i-th PMT, $f(\theta_i)$ is the PMT angular acceptance depending on the angle θ between the axis of symmetry of the PMT and the direction of the incoming photon, r_i is the distance from the scintillator ball to the i-th PMT, L is the attenuation length of the water, and Q_0 is a normalization factor. The high voltage for each PMT is adjusted so that the distribution of G_i for the 11146 PMTs has minimum spread (figure 5.2).

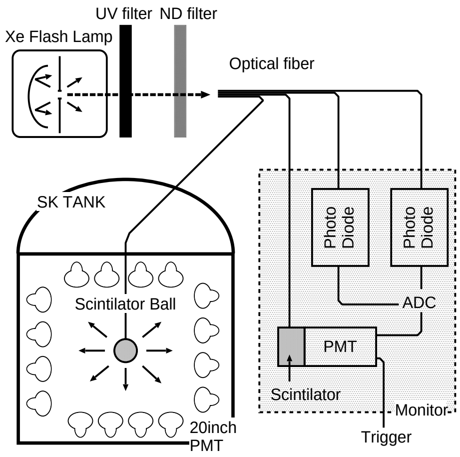

Figure 5.1: Xe/scintillator ball calibration setup.

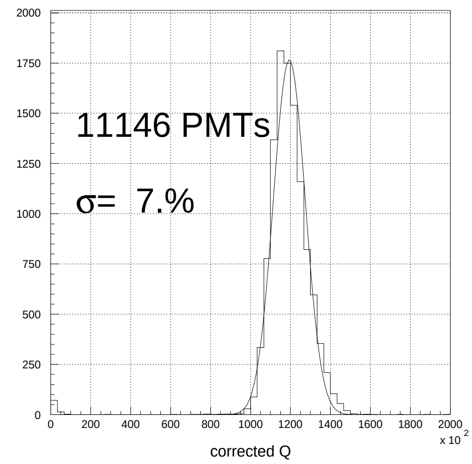

Figure 5.2: Relative gain distribution from Xe calibration.

5.2 Absolute Gain

Signals from the PMTs are measured in units of picoCoulombs (pC). Absolute gain calibration is the process of determining the conversion of pC to photoelectrons (PE). This requires a low energy source in order to generate single photoelectrons. A Cf^{252} source surrounded by Ni wire is contained in a plastic case. Spontaneous fission of Cf produces neutrons which are captured on Ni subsequently emitting γ-

rays with varying energies, the most common being 9 MeV. The γ-rays produce an electromagnetic shower from which Cherenkov radiation is generated. Single PE distributions are made for each PMT and are used to convert from raw charge in pC to PE. A sample single PE distribution is shown in figure 5.3.

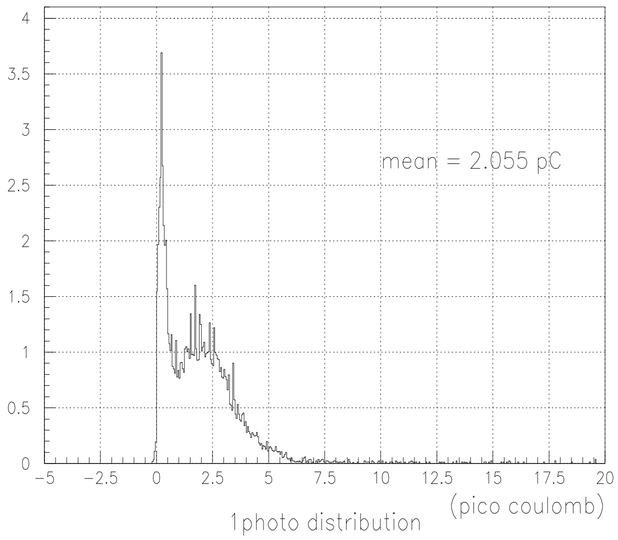

Figure 5.3: Sample single photoelectron distribution.

5.3 Timing/Charge (TQ) Calibration

Timing calibration for the PMTs is performed with the aid of the N_2 laser system shown in figure 5.4. The 337-nm output wavelength of the laser is slightly lower than typical Cherenkov radiation, therefore it is shifted to 384 nm with the aid of a dye. The intensity of the light is varied with the aid of an optical filter and the laser pulses have a width of about 4 ns. Light from the laser is transmitted via optical fiber to a diffusing ball which is suspended in the center of the Super–Kamiokande detector. Time vs. charge maps (TQ maps) are generated for each PMT using this setup and are used to shift the relative time offset for the PMTs. These maps are used in the

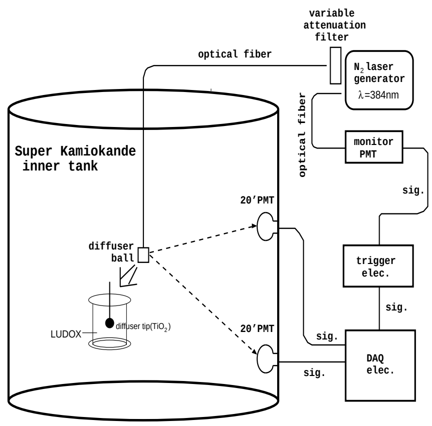

Figure 5.4: Timing calibration: Setup used to measure TQ maps for individual PMTs.

Monte Carlo detector simulation. A typical TQ-map is shown in figure 5.5.

5.4 Water Attenuation Length

5.4.1 Laser

The attenuation length of the water is measured at different wavelengths with the laser setup shown in figure 5.6. Monochromatic light produced with wavelengths from 337 nm to 600 nm from a dye module pumped by a N_2 laser is split into two beams, one of which is transmitted via optical fiber to a diffuser ball which has been lowered into Super–Kamiokande. The other beam is sent to a 2-inch diameter PMT which monitors the beam intensity. A CCD camera at the top of the tank measures the light intensity from the diffuser ball, I_{CCD}, for various depths of the ball, l_d. Several measurements are taken at each depth and wavelength. The attenuation

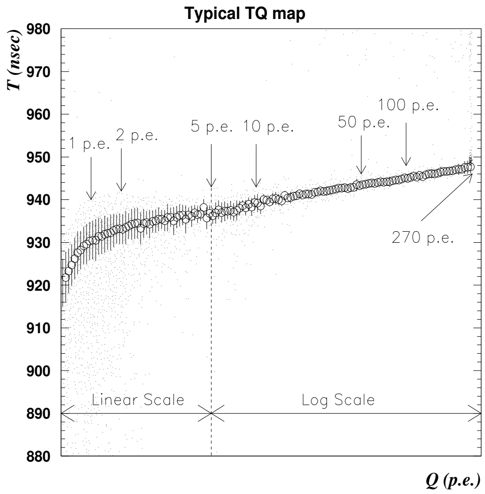

Figure 5.5: TQ map for a typical PMT.

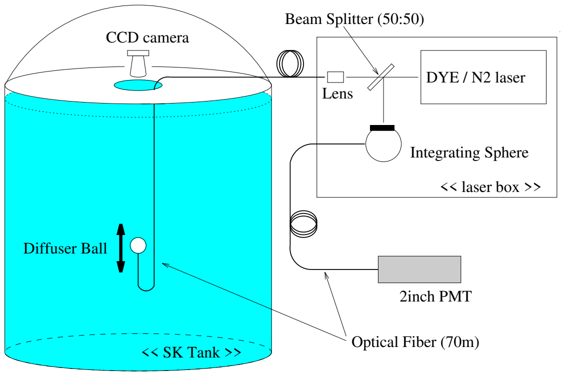

Figure 5.6: Setup used to measure water attenuation length at different wavelengths.

length for each wavelength $L(\lambda)$ is calculated by fitting the function

$$\log \frac{I_{CCD}}{I_{\text{laser}}} = A - \frac{l_d}{L(\lambda)} \tag{5.2}$$

where A is a constant. A sample distribution of I_{CCD}/I_{laser} is shown for $\lambda = 420$ nm in figure 5.7. Final results for all measurements are shown in figure 5.8. The points represent the results of the measurements and the solid lines represent a model which includes Rayleigh scattering, Mie scattering, and absorption. Rayleigh scattering is the scattering of a photon with an entire water molecule and has a $1/\lambda^4$ wavelength dependence. Mie scattering is the scattering of photons with particles within the water and has no wavelength dependence. Absorption is more pronounced for longer wavelength photons. The model shown by the solid lines in figure 5.8 is used in the Monte Carlo detector simulation.

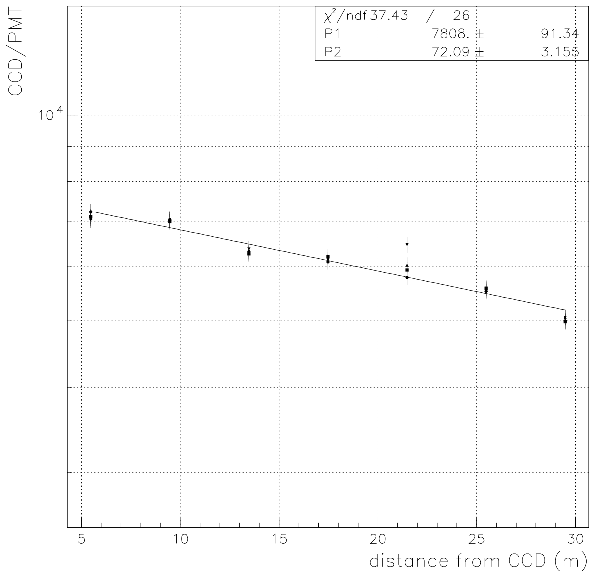

Figure 5.7: Attenuation length calibration for $\lambda = 420$ nm.

5.4.2 Cosmic-Ray Muons

Cosmic-ray muons are also used to measure the attenuation length of water in Super–Kamiokande. Although it is impossible to make a wavelength dependent measurement from them, it is nice to use a natural source to double-check the measurement from the N_2 laser method. Another virtue is that it is not necessary to halt regular data taking to make the measurement.

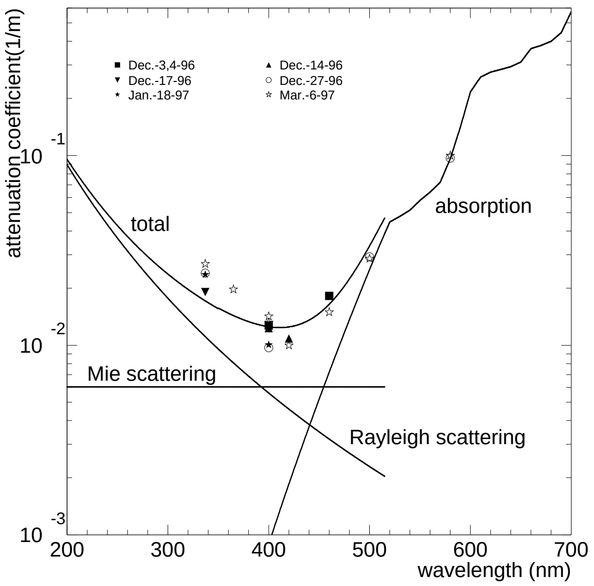

Figure 5.8: Attenuation length vs. wavelength. The solid line shows the model used in the Monte Carlo detector simulation. Points show the measurements using the N_2 laser system.

The charge detected at the i-th PMT can be written

$$Q_i = A\,\frac{f(\theta_i)}{l_i} e^{-\frac{l_i}{L}} \tag{5.3}$$

or equivalently

$$\log\left(\frac{Q_i l_i}{f(\theta_i)}\right) + const = -\frac{l_i}{L} \tag{5.4}$$

where A is some normalization constant, $f(\theta)$ is the same as the in equation 5.1, l is the path length of the photon to the PMT, and L is the attenuation length. Figure 5.9 shows $\log\left(\frac{Ql}{f(\theta)}\right)$ versus l for a sample run. The fitted slope of the line is the measurement for L. This measurement is done continuously to detect any overall variations in attenuation lengths.

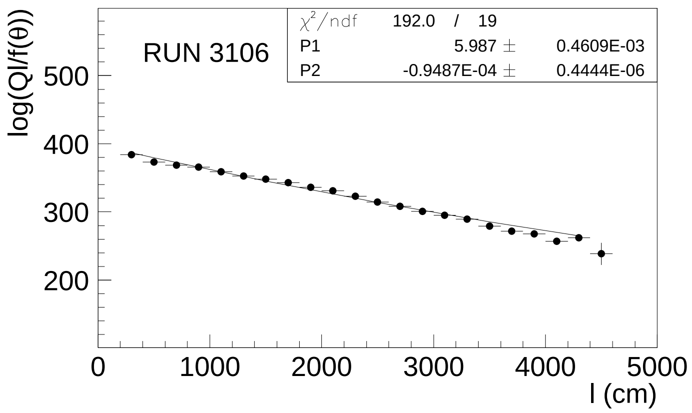

Figure 5.9: $\log\left(\frac{Ql}{f(\theta)}\right)$ versus l for cosmic ray muons in a single run of Super–Kamiokande data taking.

5.5 Energy Scale

An important part of nucleon decay analyses is choosing selection criteria using Monte Carlo samples. Many of these criteria are dependent on the energies of the particles. For this reason, it is important to correctly model the energy deposition and the detector response for particles traversing the detector in the Monte Carlo simulation. Energy scale calibration is performed by comparing data and Monte Carlo for electrons from a LINAC, decay electrons from stopping cosmic ray muons, stopping cosmic ray muons themselves, and π^0s produced in atmospheric neutrino interactions. Each source provides a calibration in a different energy range.

5.5.1 LINAC

An electron linear accelerator (LINAC) is used to calibrate the detector for the low-energy solar neutrino analysis [64]. The LINAC generates electrons which are injected vertically into Super–Kamiokande via a beam pipe whose end can be placed at various depths in the detector. A series of magnets control the direction and energy of the beam. Beam energies can be tuned to values between 5 MeV and 16 MeV. The high-energy analysis uses only the 16-MeV data for energy calibration. Figure 5.10 shows the reconstructed momentum for 16-MeV electrons generated by the LINAC for both data and Monte Carlo. The mean is 17.26 MeV for the data compared to 17.45 MeV for the Monte Carlo, corresponding to an agreement of about 1%.

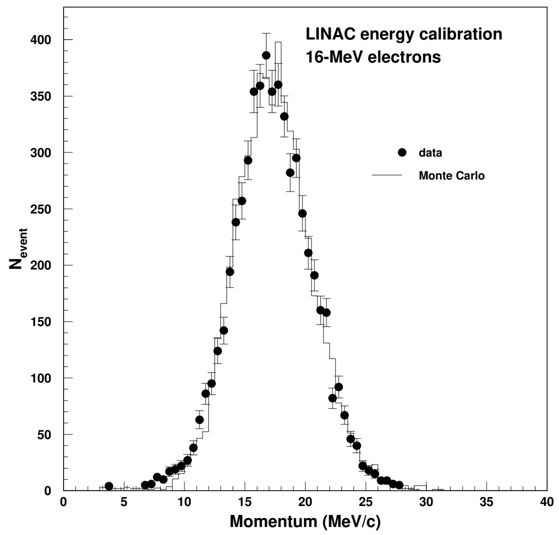

Figure 5.10: Reconstructed momentum distributions for 16-MeV electrons generated by the electron LINAC for both data and Monte Carlo. The agreement is about 1%.

5.5.2 Michel Electrons

Electrons from the decays of stopping muons are also a good energy calibration source. Decay electrons (Michel electrons) were selected by requiring

1. dwall > 2 m

2. 1.8 μs $<$ Δt $<$ 8.0 μs

3. Goodness > 0.5

4. $N_{hit}^{ID}(50 \text{ ns}) > 40$

where dwall is the reconstructed distance from the vertex to the wall (see section 8.1), Δt is the time from the muon to the decay electron, goodness is defined in equation 8.1, and $N_{hit}^{ID}(50 \text{ ns})$ is the number of hits in the ID within a 50-ns time window. The Michel spectrum for data and Monte Carlo is shown in figure 5.11. The Monte Carlo is systematically lower than data by about 2.2%.

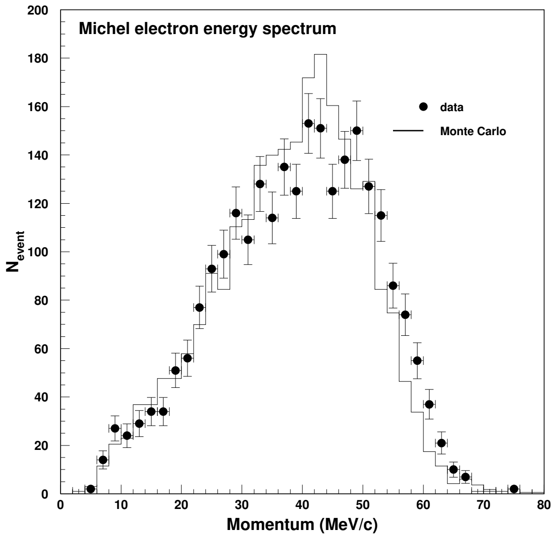

Figure 5.11: Reconstructed momentum distributions Michel electrons for both data and Monte Carlo. The Monte Carlo simulation is systematically 2.2% lower than the data.

5.5.3 Stopping Muons

Cosmic ray muons which stop in the detector are used for energy calibration using both their opening angle and the distance they traveled (range). Muons with energies greater than 1 GeV are used for range calculations and muons with energies less than 500 MeV are used for opening angle calculations. The two regimes provide energy scale determinations for two energy regions.

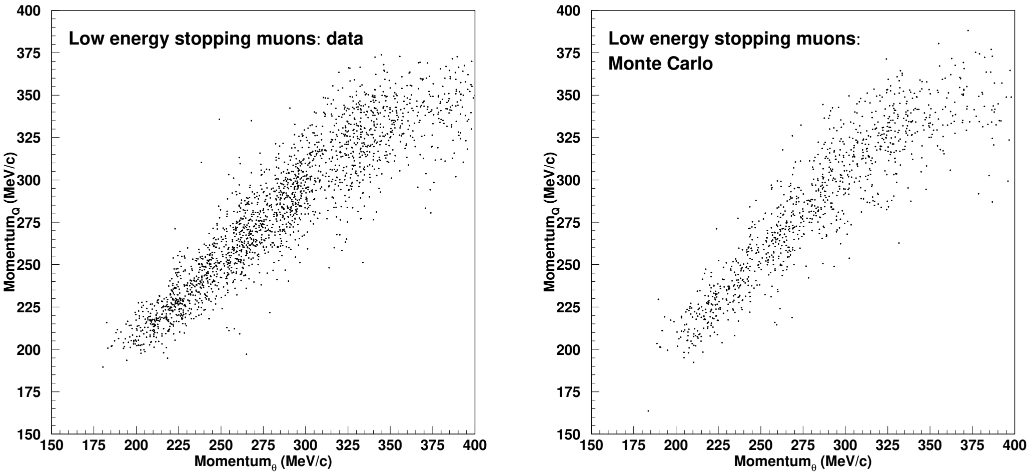

Figure 5.12: Distributions of $|\vec{p}_Q|$ vs. $|\vec{p}_\theta|$ for data and Monte Carlo low energy ($E < 400$ MeV) stopping muons. The momenta $|\vec{p}_Q|$ and $|\vec{p}_\theta|$ are the momenta calculated from the number of PE detected and the Cherenkov opening angle, respectively.

For low energy stopping muons ($E_\mu < 500$ MeV), the Cherenkov opening angle can be used to calculate the energy since it depends on the momentum according to the equation

$$\cos\theta_C = \frac{1}{n\beta} = \frac{1}{n}\sqrt{1+\left(\frac{m}{|\vec{p}_\mu|}\right)^2} \tag{5.5}$$

The Cherenkov angle for a sample of low-energy stopping muons is determined using the method described in section 8.3 and the momentum is calculated ($|\vec{p}_\theta|$) using equation 5.5. The momentum is also reconstructed from the number of PEs detected ($|\vec{p}_Q|$) using the method described in section 8.4. This provides two separate measurements of the momentum which can be compared.

The distributions of $|\vec{p}_Q|$ vs. $|\vec{p}_\theta|$ for data and Monte Carlo are shown in figure

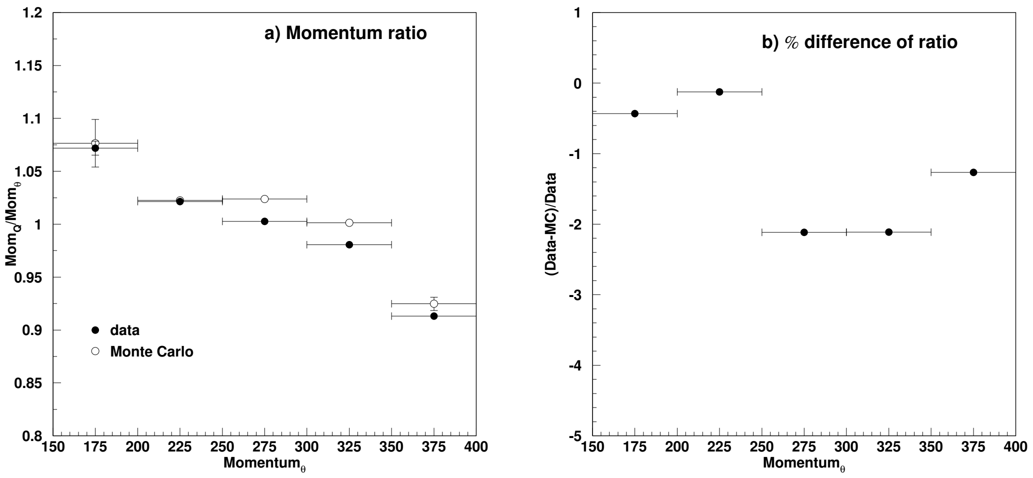

Figure 5.13: (a) Binned distributions of $|\vec{p}_Q|/|\vec{p}_\theta|$ vs. $|\vec{p}_\theta|$ for data and Monte Carlo low-energy stopping muons. (b) Percent difference between data and Monte Carlo (Data-MC)/Data.

5.12. The ratio $|\vec{p}_Q|/|\vec{p}_\theta|$ vs. $|\vec{p}_\theta|$ in bins of width of 50 MeV/c is shown in figure 5.13a and the percent difference between data and Monte Carlo with this binning is shown in figure 5.13b. The distributions agree within 2%.

The range of the muon is found by calculating the distance between the entrance point of the muon and the fitted vertex of the decay electron. Both vertices have a resolution of about 50 cm. The range gives a measurement of the momentum of the muon. This measurement is then compared to the momentum measurement ($|\vec{p}_\mu|$) from the number of PEs detected. Figure 5.14 shows the distribution of $|\vec{p}_\mu|$/range vs. range for stopping muons in the data and Monte Carlo simulated stopping muons. The data displayed in figure 5.14 were then binned into 500-MeV bins from 700 MeV to 3500 MeV (the first bin has a width of 300 MeV). This distribution is shown in figure 5.15a and the percent difference, (Data-MC)/Data, is shown in figure 5.15b. The discrepancy between data and Monte Carlo is at most 3%.

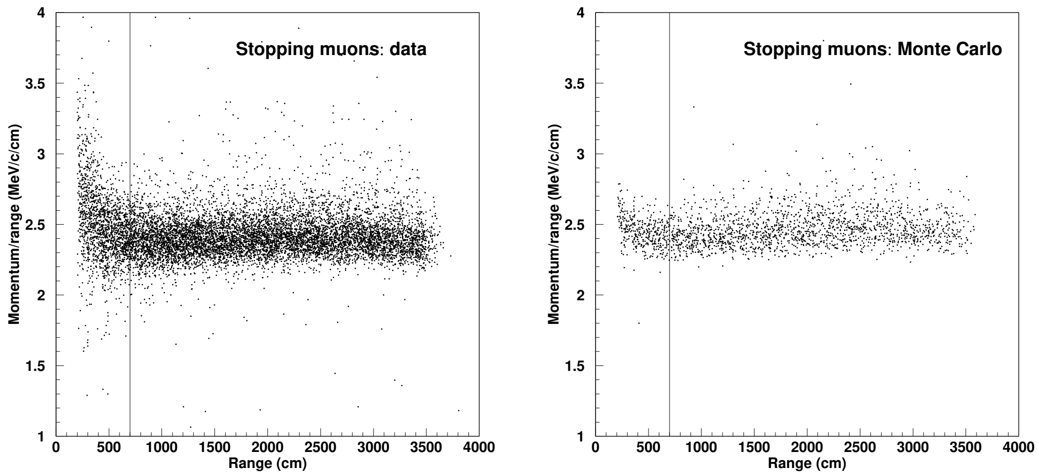

Figure 5.14: Distributions of $|\vec{p}_\mu|$ vs. range for data and Monte Carlo stopping muons. The range is defined as the difference between the muon entrance point and the vertex of the decay electron. $|\vec{p}_\mu|$ was calculated using the number of PEs detected.

5.5.4 π^0 Reconstruction

Atmospheric neutrino interactions sometimes create π^0s in Super–Kamiokande which decay immediately ($\tau \sim 10^{-16}$ s) via $\pi^0 \to \gamma\gamma$ with a branching ratio of 98.8%. The invariant mass of the π^0 is a useful energy quantity for calibration which may be calculated using the kinematic relation

$$m_{\pi^0} = \sqrt{2E_1E_2\,(1 - \cos\theta_{12})} \tag{5.6}$$

where E_1 and E_2 are the energies of the two γ-rays and θ_{12} is the angle between their momenta. Comparing the invariant mass distributions for data and Monte Carlo provides an idea of how well the energy scale is modeled in the simulation.

These events are selected by requiring

1. Two EM showers

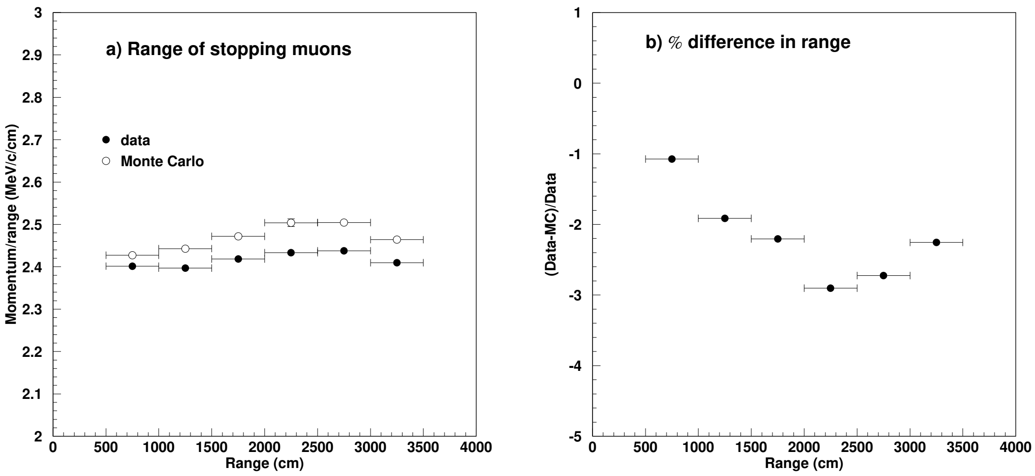

Figure 5.15: (a) Binned distributions of $|\vec{p}_\mu|$ vs. range for data and Monte Carlo stopping muons. (b) Percent difference between data and Monte Carlo (Data-MC)/Data.

2. no decay electrons

3. $|\vec{p}_{tot}| < 400$ MeV

where $|\vec{p}_{tot}|$ is the sum of the momenta of the two rings. Figure 5.16 shows the reconstructed mass for data and Monte Carlo. The distributions agree within about 3%.

5.5.5 Summary of energy scale

Based on the sources outlined in the previous sections, the energy scale is reproduced in the Monte Carlo with a deviation of no more than 3%. The sources provide calibrations over a wide range of energies varying from 16 MeV to several GeV. This is within the energy range relevant to nucleon decay studies.

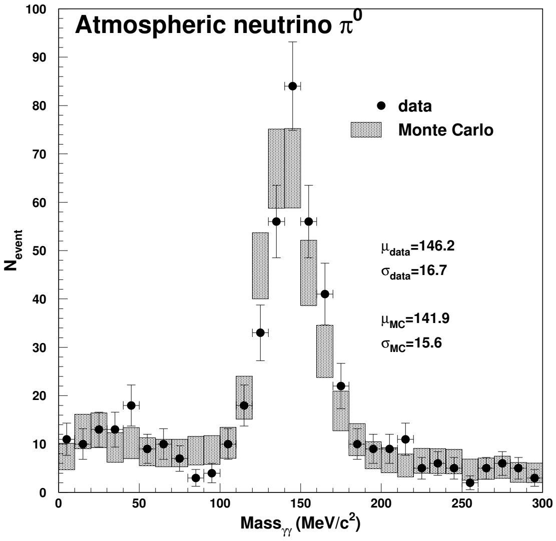

Figure 5.16: Invariant mass distributions for π^0s induced by atmospheric neutrinos for both data and Monte Carlo. The agreement is about 3%.

Chapter 6

Monte Carlo

6.1 Nucleon decay Monte Carlo

Monte Carlo simulations of nucleon decay are a critical component of nucleon decay searches. Simulations of specific decay modes provide a prediction for the signature of the events. Together with the prediction of background from atmospheric neutrinos, the signal simulation provides a method by which selection criteria for specific decay modes are chosen. Detection efficiency is then estimated by passing the nucleon decay Monte Carlo sample through the selection criteria. This section describes the process of generating a nucleon decay Monte Carlo sample.

6.1.1 Nucleon decay kinematics

Nucleon decay events are found by detecting the decay products of the nucleon. The kinematics of the decay products are determined by the initial kinematics of the nucleon. The quantities characterizing the initial state of a nucleon decay process are the nucleon's initial momentum and location in the nucleus. The former determines the energy and momenta of the decay products while the latter is a starting point for tracking the products through the nucleus.

Nucleons bound in oxygen have a non-zero momentum called "Fermi momentum." The Fermi momentum spectra for the angular momentum states $l = 0$ ("s-wave") and $l = 1$ ("p-wave") in O^{16} are shown in figure 6.1. These distributions are based on fits to measurements of electron-C^{12} scattering by Hiramatsu *et al.* [65]. The nucleon's binding energy also results in mass distributions which are displaced from the mass of a free nucleon (figure 6.2). Initial momentum and mass are randomly drawn from these distributions for nucleons in O^{16}. In addition to the nucleons bound in O^{16}, there are two additional protons from the hydrogen in H_2O. These protons are unbound within a nucleus; they have negligible initial momentum and their mass is that of a free proton.

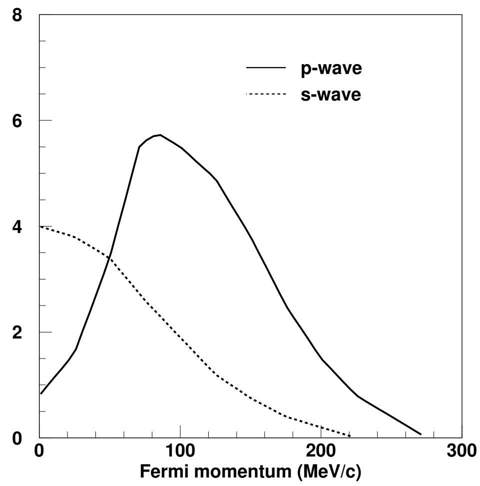

Figure 6.1: Fermi momentum distributions for s and p states in O^{16}.

After the effective mass and initial momentum are calculated, the kinematics of the decay products are calculated in the nucleon's rest frame. This dissertation studies only two body decays making the kinematics of these events simple. Momenta $\vec{p}_{final}$ of outgoing particles are equal and opposite in the rest frame of the nucleon

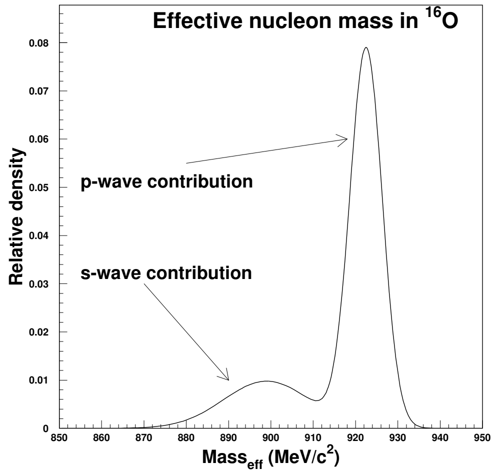

Figure 6.2: Effective mass for nucleons in O^{16}.

and have a magnitude of

$$|\vec{p}_{final}| = \frac{1}{2m_{nuc}}\left[m_{nuc}^2 - \left(m_1^2 + m_2^2\right)\right] \tag{6.1}$$

where m_{nuc} is the effective mass of the nucleon and m_1 and m_2 are the masses of the outgoing particles. A random direction is selected in the rest frame of the nucleon and a Lorentz boost corresponding to the initial momentum of the nucleon is applied to the decay products.

The initial position of the nucleon is drawn randomly from the Woods-Saxon density distribution [66] for nuclei

$$\rho(r) = \frac{\rho(0)}{1 + \exp\left(\frac{r-a}{b}\right)} \tag{6.2}$$

where $a = 1.07A^{1/3} = 2.69$ fermi for O^{16}, $2b = 0.82$ fermi is the thickness of the nuclear surface, and r is the distance from the center of the nucleus.

Hole	Resulting particles	p_γ	Probability
$p_{3/2}$	N^{15},γ-ray	6.32 MeV/c	41%
$p_{3/2}$	N^{15},γ-ray	9.93 MeV/c	3%
$s_{1/2}$	N^{14},neutron,γ-ray	7.03 MeV/c	2%
$s_{1/2}$	C^{14},proton,γ-ray	7.01 MeV/c	2%

Table 6.1: Decay modes of N^{15*} which have γ-rays as decay products.

Decaying nucleons in the $p_{3/2}$ and $s_{1/2}$ shells of O^{16} leave the residual N^{15} nucleus in an excited state which immediately decays, sometimes emitting de-excitation γ-rays. This process was studied by Ejiri [67] and the results from his analysis are used in the Monte Carlo simulation. Possible de-excitation schemes of N^{15} and their probabilities are summarized in table 6.1.

6.1.2 Nuclear Interactions

The decay products of a nucleon bound in oxygen can interact hadronically with the remaining protons and neutrons in the residual N^{15} nucleus before exiting. Interactions pertinent to the decay modes in this dissertations are K^+N elastic scattering, K^0N elastic scattering, K^+N inelastic scattering, and K^0N inelastic scattering via charge exchange.

The K^+p reaction can proceed elastically or inelastically. Inelasticities are due to a $K^+p \rightarrow K^+\Delta$ resonance. The distribution for total and elastic cross-sections based on data submitted to the particle data group [68] is shown in figure 6.3. A partial wave analysis for the scattering amplitudes was performed by Hyslop *et al.* by doing a global fit to many data samples [69] and is also shown in figure 6.3. The line around 600 MeV/c represents the maximum momentum of the K^+ from $p \rightarrow \bar{\nu}K^+$ in the rest frame of a target proton within the residual nucleus. Below 800 MeV/c or so K^+p scattering is mostly elastic, therefore a K^+ from the proton decay $p \to \bar{\nu}K^+$ will only experience elastic scattering with protons in the residual nucleus. Since proton decays via $p \to \bar{\nu}K^+$ are identified through the detection of the daughter particles of the K^+ decay at rest, K^+p scattering will not affect the detection efficiency of the proton decay mode $p \to \bar{\nu}K^+$.

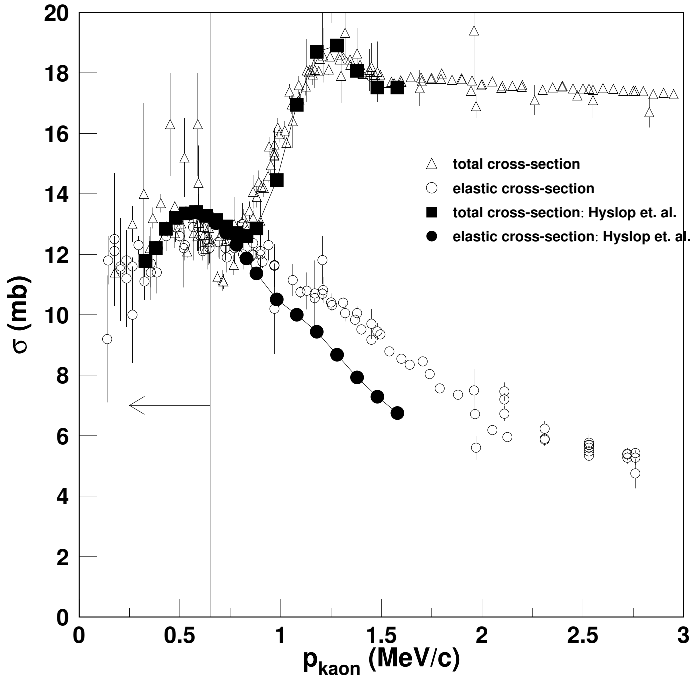

Figure 6.3: Cross sections for the K^+p interaction in the rest frame of the proton. Open triangles and circles correspond to data submitted to the Particle Data Group. Solid boxes and circles correspond to a partial wave analysis by Hyslop *et al.* The line around 600 MeV illustrates the cutoff momentum for K^+ from $p \to \nu K^+$ in the rest frame of the target proton.

The charge exchange reaction $K^+n \to K^0p$ can reduce the efficiency for detecting $p \to \bar{\nu}K^+$ events. It is important to estimate what fraction of K^+ are lost due this effect. The reaction was measured for low momentum kaons (250 to 600 MeV/c) by Glasser *et al.* [70] yielding cross sections ranging from 2.0 $\pm$ 0.18 mb at 250 MeV/c K^+ momentum to 6.4 $\pm$0.56 mb at 590 MeV/c K^+ momentum. To estimate the fraction of K^+ lost due to this effect, a Monte Carlo simulation was performed. K^+ were started at random points in the nucleus according to the Woods-Saxon density distribution (equation 6.2) with random momenta drawn from the Fermi momentum distribution. They were then stepped through the nucleus in 0.07-fm increments. At each point the nuclear density and cross-section for $K^+n \to K^0p$ charge-exchange were calculated from which an interaction probability was calculated. The K^+ was stepped through until it reached 4 fm, the outer edge of the nucleus. If there was an interaction, Pauli blocking was taken into account by requiring the momentum of the recoil nucleon to be greater than the top of the Fermi surface (p_F)

$$p_{recoil} \; > \; p_F(r) = \hbar\left(\frac{3\pi^2}{2}\rho(r)\right) \tag{6.3}$$

where $\rho(r)$ is the same as defined in equation 6.2. On the basis of this simulation, it is estimated that 4% of K^+ from $p \to \bar{\nu}K^+$ proton decays are lost due to charge exchange.

Because of isospin symmetry, the K^0N reactions have essentially the same magnitude as the K^+N reactions. For this reason, it is estimated that approximately 4% of K^0 from $n \to \bar{\nu}K^0$, $p \to \mu^+K^0$, and $p \to e^+K^0$ are lost due to the charge exchange reaction $K^0p \to K^+n$. Elastic scattering was estimated to have a small effect and was neglected.

Interactions of pions in nuclei are not important for the Monte Carlo simulation of nucleon decay modes studied in this dissertation, but they are important for the estimation of background from atmospheric neutrinos to these decay modes. Details of these nuclear interactions will be described in the following section.

6.2 Atmospheric Neutrino Monte Carlo

Atmospheric neutrinos are produced in collisions of cosmic rays with air molecules in the atmosphere of Earth. Primary cosmic rays interact hadronically with air molecules creating $\pi^{\pm}$,$K^{\pm}$, K^0, and other mesons. Neutrinos are then produced through the decay chains of these mesons

$$\pi^+ \rightarrow \mu^+ \nu_\mu \tag{6.4}$$

$$\mu^+ \rightarrow e^+ \bar{\nu}_\mu \nu_e \tag{6.5}$$

$$\pi^- \rightarrow \mu^- \bar{\nu}_\mu \tag{6.6}$$

$$\mu^- \rightarrow e^- \nu_\mu \bar{\nu}_e \tag{6.7}$$

$$K^+ \rightarrow \mu^+ \nu_\mu \quad (63.5\% \text{ B.R.}) \tag{6.8}$$

$$K^+ \rightarrow \pi^+ \pi^0 \quad (21.2\% \text{ B.R.}) \tag{6.9}$$

$$\cdots$$

The ratio of K production to π production varies with energy of the primary cosmic ray. It is 7% and 11% for 10 and 100-GeV primaries, respectively.

Because the cross sections for neutrinos to interact with matter is extremely small, they can travel unscathed through the earth and interact with a nucleon in the water of Super–Kamiokande via the weak interaction. A generic interaction is

$$\nu_l + N \rightarrow l + N' + X \tag{6.10}$$

where N and N' are the initial and final state nucleons, l is the outgoing lepton associated with ν_l, and X are other possible hadronic particles such as pions. Because some of these interactions result in topologies similar to those of nucleon decays, they present a challenging background to nucleon decay searches. It is necessary to understand and predict this background as precisely as possible.

6.2.1 Atmospheric Neutrino Flux

The first step in predicting the atmospheric neutrino background is calculating the flux of atmospheric neutrinos at Super–Kamiokande. The calculation by Honda [71][72] was used in this dissertation. The neutrino oscillation analysis also uses the Bartol calculation [73] as a cross check. The calculations agree within a few percent, and therefore the Honda calculation is sufficient for this analysis. A summary of Honda's calculation will be given in this section.

Primary cosmic rays are composed of mainly hydrogen and helium nuclei with abundances of $\sim 95\%$ and 5%, respectively. Calculation of the flux of these primaries is done in two energy regimes, lower energy (0.01-100 GeV) and higher energy (100-1000 GeV).

Low energy cosmic rays are affected by solar activity. Higher solar activity (solar maximum) influences lower energy cosmic rays in such a way that the flux at earth is smaller. The solar cycle has a period of 11 years with the last solar minimum in 1996 and the next solar maximum in 2001. The middle of the solar cycle was used in the flux calculation of atmospheric neutrinos. The earth's magnetic field also affects the flux in such a way that there is a deficit of low energy cosmic rays ($p < 50$ GeV/c) coming from the east. This has been observed in Super–Kamiokande by a deficit of neutrinos with momenta ranging from 400 MeV/c to 3000 MeV/c [74].

In the higher energy regime (> 100 GeV) the spectrum is fit to a power law

$$\Phi = A\left(\frac{E}{100\mathrm{GeV}}\right)^{\gamma} \tag{6.11}$$

where A is a normalization factor having units of flux, $\mathrm{m}^{-2}\ \mathrm{sec}^{-1}\ \mathrm{steradian}^{-1}\ \ \mathrm{GeV}^{-1}$. The fits are ($A = 6.65$, $\gamma = -2.75$) for hydrogen nuclei and ($A = 3.28$, $\gamma = -2.64$) for helium nuclei. The resulting fluxes for H,He, and CNO nuclei are shown in figure 6.4. The final neutrino flux calculated at the Super–Kamiokande site is shown in figure 6.5. The overall uncertainty in the absolute flux is $\sim 20\%$.

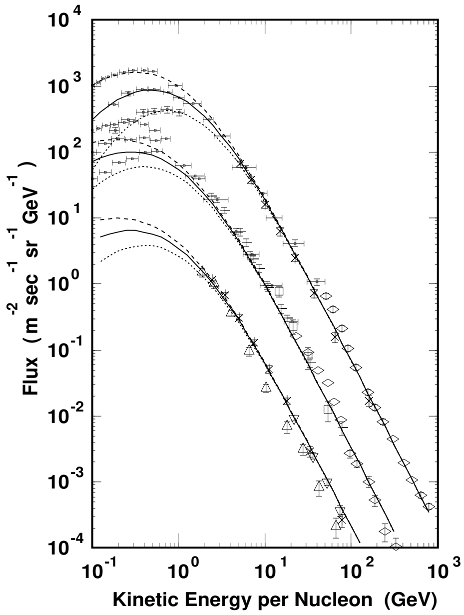

Figure 6.4: Flux of primary cosmic rays used in Honda's calculation. The top three curves correspond to calculations for solar minimum (top), solar average (middle), and solar maximum (bottom) for Hydrogen. Similarly, the middle three correspond to Helium and the bottom three to CNO. Points are from experimental measurements.

6.2.2 Neutrino-nucleon Cross sections

Once the flux of atmospheric neutrinos at Super–Kamiokande has been estimated, their interaction rate in the detector needs to be calculated. In the simulation, the following charged and neutral current neutrino interactions are taken into account

1. Quasi-elastic scattering

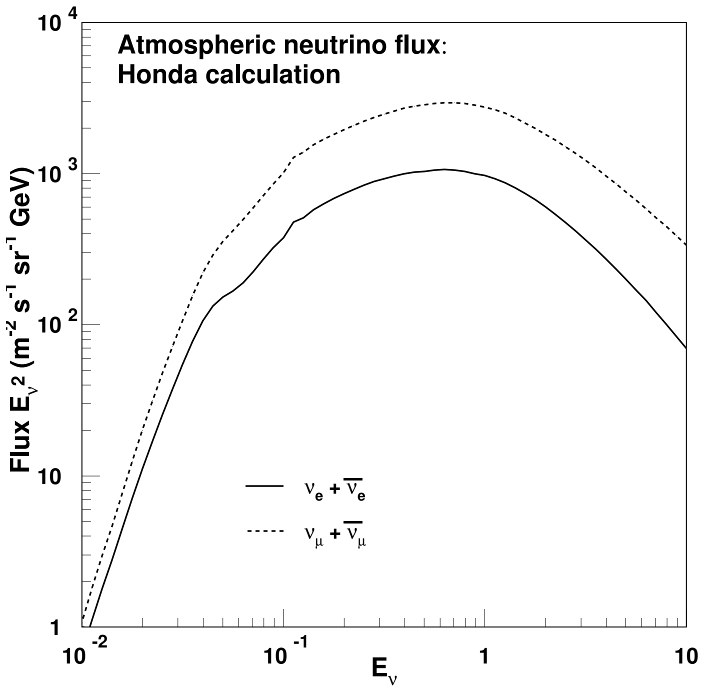

Figure 6.5: Neutrino flux in the middle of the solar cycle at the Super–Kamiokande site calculated by Honda *et al.* The overall uncertainty is $\sim 20\%$.

2. Single pion production
3. Multiple pion production
4. Coherent pion production
5. η,K production
6. Deep inelastic scattering

This section summarizes the cross sections for each of these processes. Fermi momentum in O^{16} is taken into account for νN scattering using the distribution in figure 6.1. In addition, Pauli blocking is taken into account by requiring that the recoil nucleon in the scattering is greater than the Fermi surface momentum (equation 6.3).

Quasi-elastic

Charged current and neutral current quasi-elastic reactions are calculated using standard $V - A$ theory. A detailed calculation was done by Llewellyn-Smith [75]. The cross sections are shown in figure 6.6. Quasi-elastic interactions are typically characterized in Super–Kamiokande by their single track either from the outgoing lepton in $\nu N \rightarrow lN'$ charged current interactions or a recoil proton above Cherenkov threshold in $\nu N \rightarrow \nu N$ neutral current interactions.

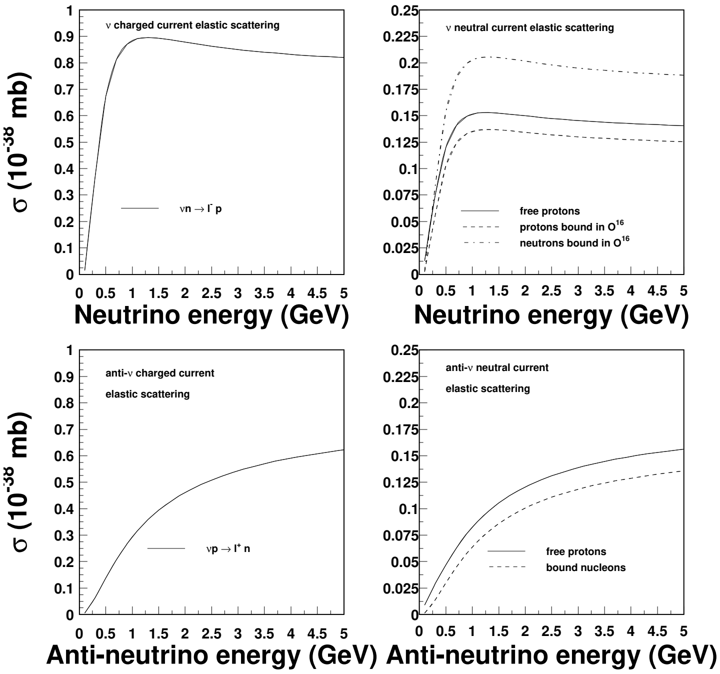

Figure 6.6: Charged and neutral current quasi-elastic scattering cross sections for both $\bar{\nu}$ and ν.

Because quasi-elastic interactions typically do not induce multi-ring events, they do not contribute significantly to backgrounds of nucleon decays which produce multiple particles. The only nucleon decay mode studied in this dissertation to which quasi-elastic scattering contributes to the background significantly is $p \to \bar{\nu}K^+$; $K^+ \to \mu^+\nu_\mu$ which is characterized by a 236-MeV/c monochromatic muon. The quasi-elastic reactions produces a large but continuous background. One way to find the proton decay $p \to \bar{\nu}K^+$; $K^+ \to \mu^+\nu_\mu$ is to search for a peak above background in the muon momenta spectrum.

Meson Production

Meson production induced by atmospheric neutrinos is the most challenging background to nucleon decay. Because of their potential for multiple tracks, these events can mimic nucleon decay events. Most of the mesons produced in atmospheric neutrino interactions are pions. Pion production can be generally classified into two types, single-π and multi-π production. Although the effect is small compared to pion production, K^+, K^0, and η production is included in the Monte Carlo simulation.

Single-π production begins to become important at a neutrino energy of about 1 GeV. The model by Rein and Sehgal [76] is used to calculate the cross sections and subsequent rates in Super–Kamiokande of single-π production. This model uses the fact that neutrinos with energies above 1 GeV interacting with nucleons can generate resonances which subsequently decay, emitting pions

$$\nu N \to lN^* \to lN'\pi \tag{6.12}$$

where N is the target nucleon, N^* is the resonant state, l is the outgoing lepton, and N' is the final state nucleon. Fourteen resonances are included in the simulation and both charged current and neutral current scenarios are included. Plots of cross section are shown in figure 6.7.

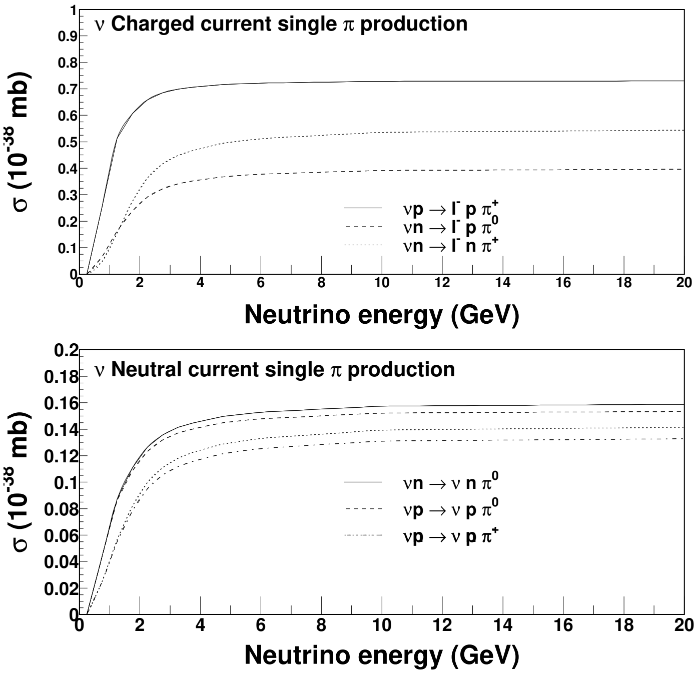

Figure 6.7: Single-pion production cross sections.

The dominant resonance in the region below 1.4 GeV is the $\Delta(1232)$ resonance. For this resonance, the angular distribution for the resulting pion is determined using Rein and Sehgal's calculation [76]. The angular distributions for the resulting pions for other resonances are assumed to be isotropic.

Coherent scattering occurs when a neutrino scatters off of the O^{16} nucleus as a whole rather than a nucleon within it. These reactions can induce only single pion production. The model used is outlined in references [77, 78]. Coherent scattering is clean in that pions are produced outside the O^{16} nucleus so nuclear interactions do not play a part. Cross section plots for coherent scattering are shown in figure 6.8.

Deep inelastic scattering with multiple π production at νN invariant masses of the neutrino-nucleon system above 2 GeV is included using a model based on the

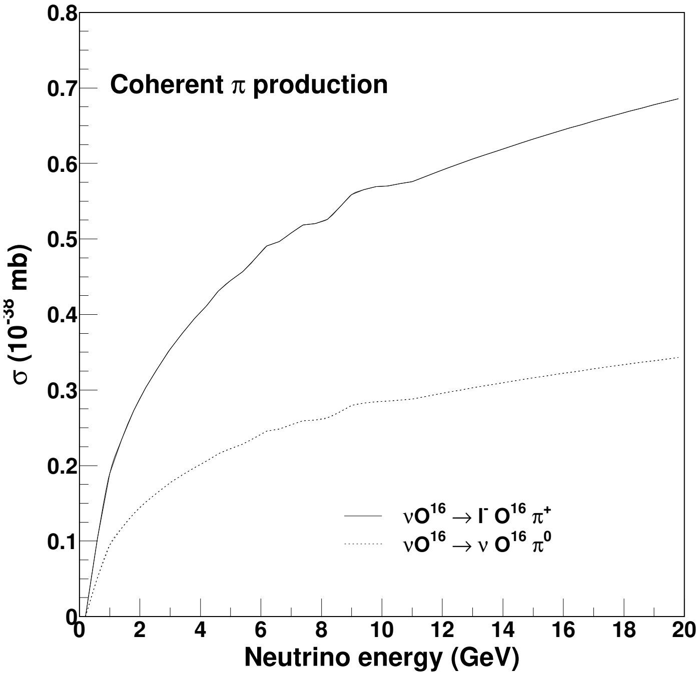

Figure 6.8: Coherent-pion production cross sections.

GRV94 calculations of the parton distribution functions of the nucleus [79]. For invariant masses from 1.4 GeV to 2.0 GeV, the model by Rein-Sehgal is used [77]. The cross sections for multiple π production are shown in figure 6.9.

The mean number of pions, $\bar{n}_\pi$ produced in multiple pion production interactions was studied at Fermilab with the 15-foot hydrogen bubble chamber [80]. The multiplicity was fit to the data

$$\bar{n}_\pi = 0.09 + 1.83 \ln W^2 \tag{6.13}$$

where W is the νN invariant mass of the system. The forward-backward asymmetry of the pion production was determined by the BEBC experiment [81] and is given

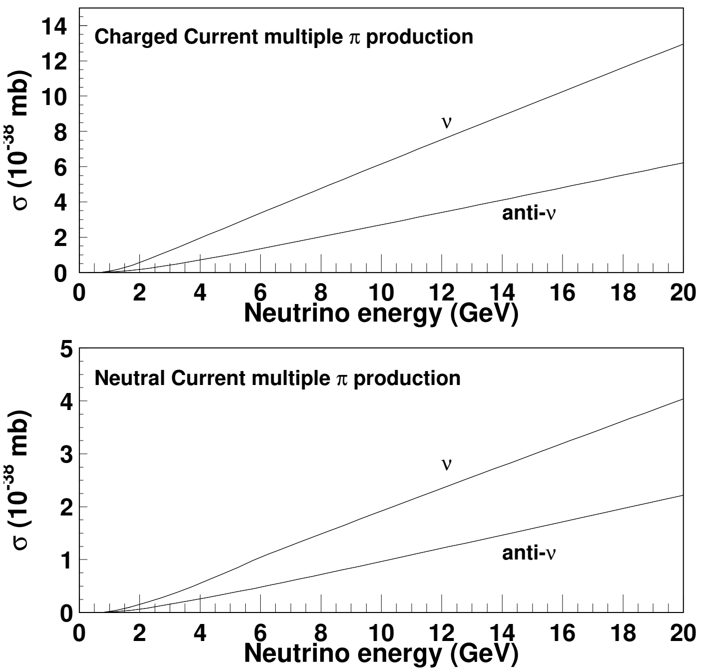

Figure 6.9: Multiple-pion production cross sections.

by the relation

$$\frac{\bar{n}_\pi^f}{\bar{n}_\pi^b} = \frac{0.35\ +\ 0.41\ln W^2}{0.50\ +\ 0.09\ln W^2} \tag{6.14}$$

Finally, neutral current cross sections of deep inelastic scattering are calculated from the charged current cross sections using the relations outlined in reference [82, 83].

Production of K^+, K^0, and η mesons is included based on the model of Rein and Sehgal [76, 84]. Although these interactions may seem as if they would contribute to the background to nucleon decay modes with kaons in the final state, their cross sections are rather small compared to those for single-pion and multi-pion production. In addition, K production is accompanied by a Λ baryon which decays into either $p\pi^-$ or $n\pi^0$. Figure 6.10 shows the various cross sections for K production and figure 6.11 shows the various cross sections for η production.

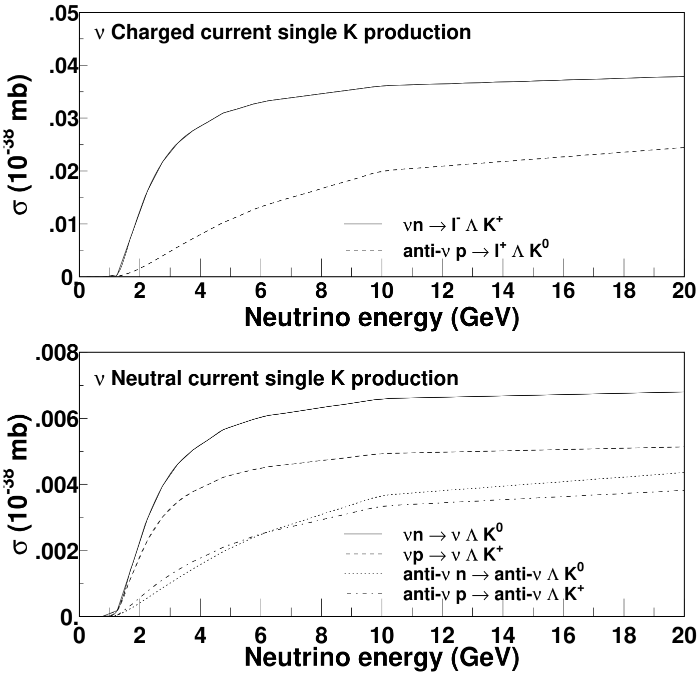

Figure 6.10: K production cross sections. These cross sections are small compared to those for single-π and multi-π production.

6.2.3 Propagation of Pions Through Nucleus

Nuclear interactions of pions before escaping the nucleus affects the estimation of background for nucleon decay. To estimate this effect, pions are propagated through the nucleus after they are created in simulated atmospheric neutrino interactions. The starting point of the pion is determined using the Woods-Saxon density distribution (equation 6.2), and the pion is stepped through the nucleus from that point in 0.07-fm increments. At each step, the cross sections for charge exchange, pion absorption, and inelastic scattering are calculated using the model by Oset *et al.* [85]. The probability of each of these interactions for positively charged pions is shown in figure 6.12 [86]. The model used was checked using experimental data from

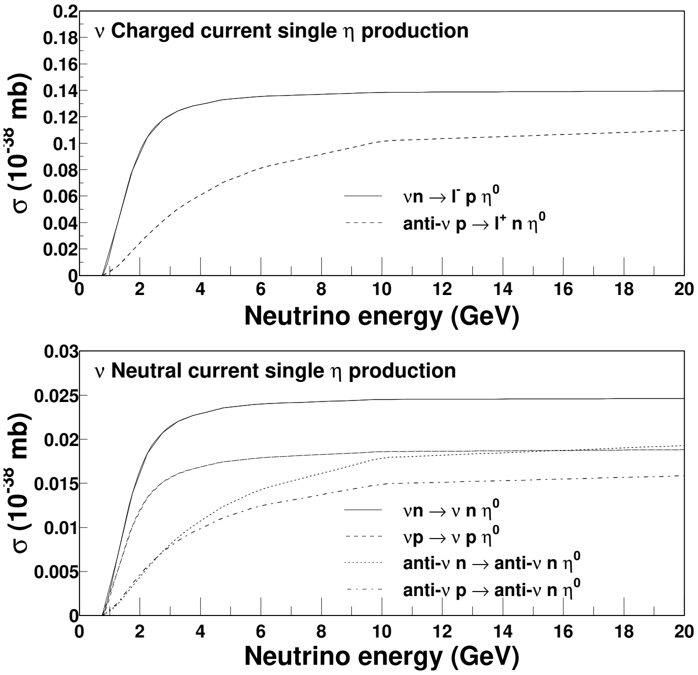

Figure 6.11: η production cross sections. Like the cross sections for K production, they are small compared to those for single and multi-π production.

π^+-O^{16} scattering [87] and π^+-C^{12} scattering [88] and a comparison of data [87] and Monte Carlo for the differential cross sections of π^+-O^{16} scattering for three momenta ($p = 213, 268, 353$ MeV) is shown in figure 6.13. Finally, Pauli blocking is taken into account by requiring the recoil nucleon to be above the Fermi surface (equation 6.3).

6.2.4 Normalization of Background

Using the neutrino flux calculation described in section 6.5 and the cross sections for various neutrino interactions described in section 6.2.2, a final 40-year equivalent sample of atmospheric neutrino Monte Carlo was generated. It has been well known for some time that there is a deficit of events induced by muon neutrinos [89, 90, 51, 91].

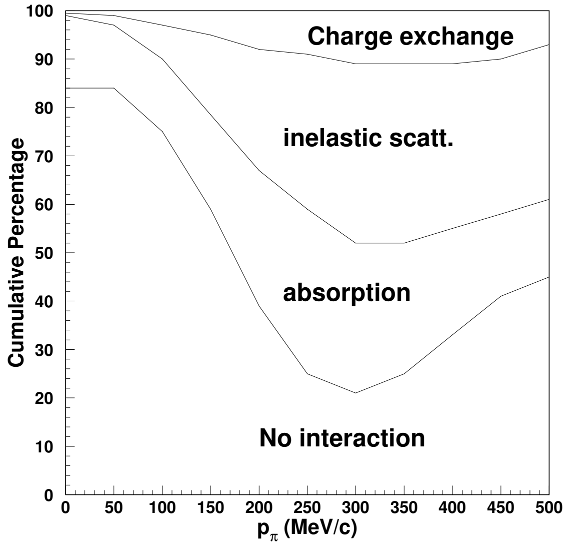

Figure 6.12: Cumulative probabilities for absorption, inelastic scattering, charge exchange, and no interaction of positively charged pions traversing an O^{16} nucleus as a function of the pion's momentum.

To estimate the actual number of background events, the flux was normalized based on the observed deficit of muon neutrinos [29, 28] and the observed number of electron neutrinos. This normalization assumes that muon neutrinos oscillate to tau neutrinos and electron neutrinos do not participate in oscillation. Therefore, the electron neutrino events are used as an overall normalization. Charged current background events induced by electron neutrinos were given a weight of 1.17 while the charged current events induced by muon neutrinos were given a weight of 0.74. All neutral current events were weighted by 1.17. Finally the 40-year sample (898 kton·years) was normalized to the 61-kton·year sample of Super–Kamiokande exposure.

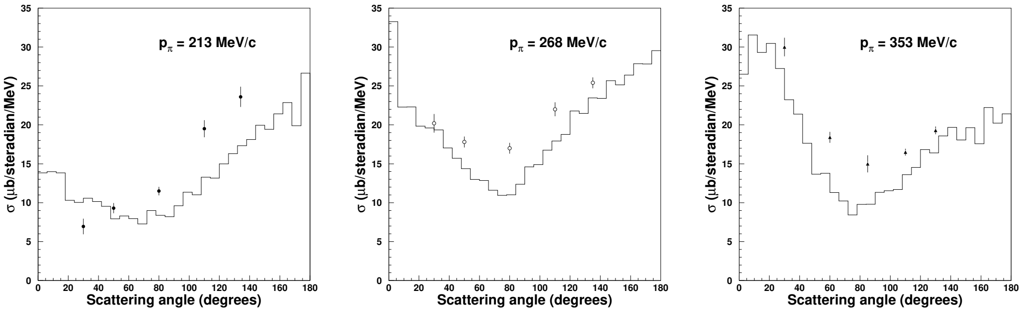

Figure 6.13: Differential cross sections for π^+-^{16}O scattering. The points show the experimental measurement of Ingram *et al.* and the histogram shows the result of the Monte Carlo simulation.

6.3 Detector Simulation

The GEANT [92] program developed at CERN was used in the detector simulation of particles traversing the detector. The program handles the physics processes, detector geometry and response, and run and event control. Hadronic interactions above 500 MeV were simulated using the CALOR [93] program which was also developed at CERN. For energies less than 500 MeV a custom program was used [86].

The number of Cherenkov photons generated by a particle at each wavelength is sampled from the Poisson distribution whose mean is given by equation 4.2. They are emitted at an angle relative to the direction of the path of the particle given by 4.1. Once the photons are emitted, they can undergo Rayleigh scattering, Mie scattering, or absorption. Measurements with an N_2 laser of these contributions is summarized in section 5.4. Figure 5.8 shows with solid lines the model used in the detector simulation and with points the results of the measurement.

Signals are generated for photons which strike the face of a PMT using the quantum efficiency curve shown in figure 4.6 and the single PE distribution for that particular PMT (figure 5.3).

Chapter 7

Selection of Contained Events

Approximately 5×10^5 "high-energy" triggers are recorded in Super–Kamiokande per day, corresponding to about 10 gigabytes of data. Most are either low energy events caused by radioactivity or cosmic ray muons. These data are not interesting to nucleon decay or atmospheric neutrino analyses and must be removed from the sample.

7.1 1st Reduction

The large size of the unreduced data set requires the first step of reduction to quickly reduce the sample significantly. The criteria are:

1. $N_{hit}^{OD}(800 \ \text{ns}) < 50$ hits

2. $N_{hit}^{ID}(300 \ \text{ns}) > 200$ PE

3. time to previous event $> 100 \ \mu$sec

where $N_{hit}^{OD}(\Delta t)$ ($N_{hit}^{ID}(\Delta t)$) is the number of OD (ID) hits within a time window of width Δt. The first criterion removes cosmic ray muons. The second removes low energy events where 200 PE corresponds to an electron with an energy of about 23 MeV. The third criterion removes events caused by decay electrons from stopping cosmic ray muons. This reduction reduces the data set by a factor of ~100 to ~4000 events/day.

7.2 2nd Reduction

The 2nd reduction is designed further to eliminate low energy events and cosmic-ray muons. The selection criteria are:

1. $Q_{max}/Q(300\ \mathrm{ns}) < 0.5$
2. $N_{hit}^{OD}(500\ \ \mathrm{ns}) < 50$ or $N_{hit}^{OD}(500\ \ \mathrm{ns}) > 25$ and $Q_{tot} < 10^5$ PE

where Q_{max} is the largest charge recorded by a single PMT, $Q(\Delta t)$ is the total charge recorded by the ID in a time window of Δt, and Q_{tot} is the total number of PE detected by the ID. The first criterion removes noise events which have one large accidental hit. The second is a further reduction of cosmic ray muon events. The data rate after this reduction is ~400 events/day.

7.3 3rd Reduction

At this stage the event rate is small enough so detailed cuts requiring more computation time are applied to the sample. The third reduction consists of six steps.

7.3.1 Through going muons

Through going muons enter the detector at some point and leave at some other point. Candidates are first selected by requiring that

1. $Q_{max} \geq 230$ PE

2. $N_{hit}^{ID} \geq 1000$

where N_{hit}^{ID} is the total number of hit PMTs in the ID. After events pass these criteria, a muon fitter is applied and a direction is fit by estimating the entering and exiting points of the muon. The entering point is defined as the position of the earliest hit PMT with at least two hit PMTs next to it. The exiting point is defined as the central point where the PMTs are saturated. If the sum of OD hits within an 8-m radius and 800-ns time window ("OD cluster") of the projected entering or exiting point of the muon is greater than 9, the event is classified as a "through-going muon" and discarded.

7.3.2 Stopping muons

Stopping muons are cosmic ray muons which enter the detector but stop and decay instead of exiting. A rough guess for the entrance point (vertex) of the muon is taken to be the earliest hit PMT with at least two hit neighboring PMTs. This vertex is refined and a direction is fit by maximizing the sum of charge in a cone with opening angle of 44 degrees whose axis corresponds to the direction of the muon. After a vertex and direction are found goodness G_{tot} is calculated using equation 8.6. Events with $G_{tot} > 0.5$ having greater than 9 hits in the OD cluster projected back from the fitted direction are classified as a stopping muon and discarded.

7.3.3 Low energy event rejection

Events are rejected if they satisfy one of the following criteria::

1. $N_{hit}^{ID} \leq 500$ and $N_{hit}^{ID}(50 \text{ ns}) < 50$

2. $G_{point} < .5$

where G is defined in equation 8.1. These low energy events are first fit using the low energy vertex fitter. This fitter uses a grid search to maximize the goodness of vertex fit of tubes within a 50-ns timing window. If the goodness is < 0.5, the event is rejected. If the number of hits in the 50-ns time window is < 50, the event is also rejected. In the low energy analysis, nhit is converted to energy. Roughly 5 hits = 1-MeV. Therefore, electrons with energies of less than about 10 MeV are rejected by this cut.

7.3.4 Flasher rejection

PMTs can sometimes have a breakdown in the dynode chain which cause them to emit light which can trigger the detector. These PMTs are called "flashers." Such events typically have a wide timing distribution with many hits occuring well after the main trigger. Events caused by particles traversing the detector typically have hits with times of no more than 100 ns later than the main trigger. Flashing events are rejected by satisfying one of the following criteria:

1. $N_{min}^{slide}(100 \text{ ns}) > 14$

2. $N_{min}^{slide}(100 \text{ ns}) > 9$ and $N_{hit}^{ID} < 800$

where $N_{min}^{slide}(\Delta t)$ is the minimum number of hits occuring in a sliding window of width Δt from about 200 ns to 800 ns after the detector triggers.

7.3.5 Cable hole

The cables which supply power to and transmit signals from the PMTs are bundled together and leave the tank through 12 "cable holes." Four of the bundles make the

OD insensitive in these regions. When data taking began in April 1996, cosmic-ray muons would sometimes pass through the OD into the ID through one of the four cable-bundles. This would cause the ID to trigger with no signal in the OD. In April 1997, "veto-hats" were installed above each of the four troublesome cable-bundles to reduce the rate of muons passing through the bundles without being detected by the OD. These are 2 m $\times$ 2.5 m scintillation counters which if fire, the stopping muon fitter is applied and the event is rejected if the reconstructed vertex is within 4 m from the location of the "veto-hat" that fired.

7.4 Final Reduction: flashscan and scanning

After the third reduction, the event rate is about 30 events/day. Unfortunately this is not a pure atmospheric neutrino/nucleon decay sample. There still remain impurities from cosmic-ray muons and flashing PMTs. "Flashscan" is a program which uses spatial correlations between hit PMTs in separate events to reduce the number of flashers [29]. This program reduces the number of events that must be scanned by physicists from about 30 events/day to about 17 events/day. The remaining events ars scanned by physicists to further eliminate any remaining contamination from flashers or cosmic-ray muons.

7.5 Final Event Sample

The final event rate of fully contained events after the fourth reduction is about 15-events/day. The rate of events with vertices reconstructing within the fiducial volume of the detector, defined as 2 m from the detector wall, is 8.3 events/day. The estimated probability to lose a fully contained atmsopheric neutrino or nucleon decay event through the reduction steps is less than 0.1%. In the 61-kton·year data sample used in this dissertation, 7940 contained events were recorded in the fiducial volume of the detector.

Chapter 8

Event Reconstruction

Event reconstruction is the process of determining the various event characteristics such as vertex, number of particles traversing the detector, the directions and momenta of these particles, and the number of decay electrons. This chapter describes the procedure for determining the various event characteristics.

8.1 Single ring fitting: afit

The first step in event reconstruction is vertex fitting. The vertex is defined as the location of the neutrino interaction or nucleon decay. Using timing information, a point fit is performed by maximizing the goodness of fit defined as

$$G_{point} = \frac{1}{N_{hit}} \sum_i \exp\left(\frac{(t_i - \bar{t})^2}{2a^2\sigma^2}\right) \tag{8.1}$$

where N_{hit} is the number of hit PMTs considered in the fit, $\bar{t}$ is the average time-of-flight subtracted time, σ is the typical timing resolution (2.5 ns), $a = 1.5$ is a factor used to account for scattered light, and t_i is the time of flight subtracted time from the vertex to the ith PMT

$$t_i = \frac{1}{v(d_i, q_i)} d_i \tag{8.2}$$

where d_i is the distance from the ith PMT to the vertex, and $v(d_i, q_i)$ is the velocity of light which depends on d_i and q_i, the charge detected at the i-th PMT.

After the point fit, a direction is calculated.by optimizing the function

$$G_{dir} = \frac{\int_0^{\theta_{edge}} Q(\theta)d\theta}{\sin\theta_{edge}} \exp\left(-\frac{(\theta_{edge} - \theta_C)^2}{\sigma^2}\right) \tag{8.3}$$

where $Q(\theta)$ is the distribution of charge as a function of angle relative to the trial direction (the $Q(\theta)$ distribution for a 525-MeV electron is shown in figure 8.1) and θ_C is the maximum Cherenkov angle for when a particle's velocity $\beta = 1$. θ_{edge} is the angle θ closest to and greater than θ_{peak} where the second derivative of the $Q(\theta)$ distribution is equal to 0. For trial directions, G_{dir} is calculated. The direction and opening angle θ_{edge} are found by maximizing G_{dir}.

The method described above only gives a rough estimate of the vertex and direction of the track. It does not take into account the finite track length of the particle. This is accomplished by defining two goodnesses, G_I and G_O where

$$G_I = \sum_i \frac{1}{\sigma_i^2} \exp\left(-\frac{(t_i - \bar{t})^2}{2a^2\bar{\sigma}^2}\right) \tag{8.4}$$

$$G_O = \sum_i \frac{1}{\sigma_i^2} \max\left[\exp\left(-\frac{(t_i - \bar{t})^2}{2a^2\bar{\sigma}^2}\right), 0.8\ \exp\left(-\lambda_{const}(t_i - \bar{t})\right)\right] \tag{8.5}$$

where $a = 1.5$ accounts for scattered light, σ_i is the timing resolution of the i-th PMT, $\bar{\sigma}$ is the average of the σ_i's, t_i is the residual time of the i-th PMT, $\bar{t}$ is the average of the t_i's, and $\lambda_{const} = 1/(20\ \text{ns})$ is the average difference in time between direct and scattered light. The factors G_I and G_O correspond to direct and scattered

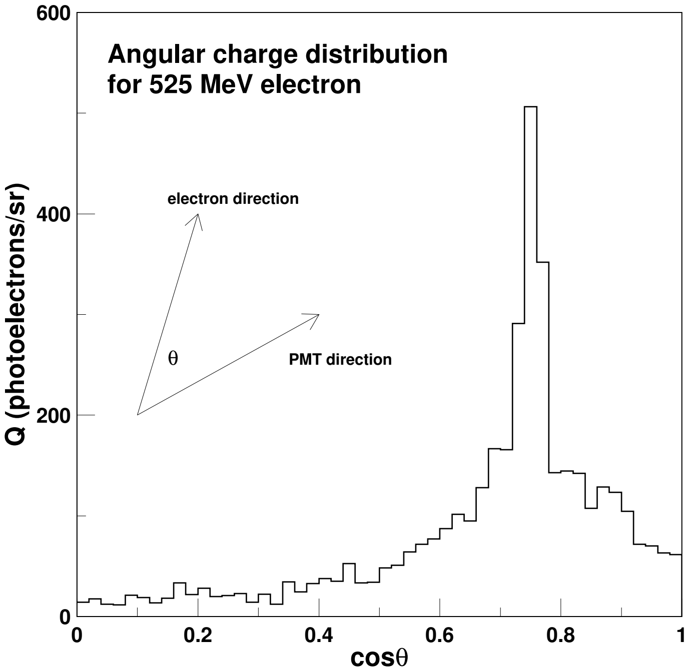

Figure 8.1: A $Q(\theta)$ distribution for a 525-MeV electron.

light, respectively. In G_I, only PMTs with angles $\theta_i < \theta_{edge}$ or with times $t_i < \bar{t}$ are included. For G_O, tubes with angles $\theta_i > \theta_{edge}$ and times $t_i > \bar{t}$ are included. The final goodness is defined as

$$G_{tot} = \frac{G_I + G_O}{\sum_i \sigma_i} \tag{8.6}$$

The goodness is calculated for varying vertices and directions. A final vertex and direction is the point where the goodness is maximized.

The distributions of vertices for single-ring muons with momenta in the range of $p \to \bar{\nu}K^+$; $K^+ \to \mu^+\nu_\mu$ and sub-GeV multi-ring for the 61-kton·year data sample is shown in figure 8.2. Sub-GeV events are defined as events having visible energy less than 1.33 GeV. These are the only samples pertinent to nucleon decay analyses since nucleon decays are often characterized by multiple rings with a maximum total

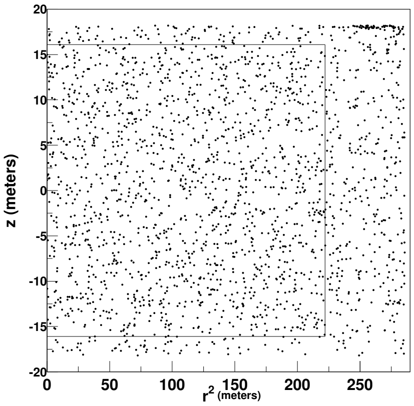

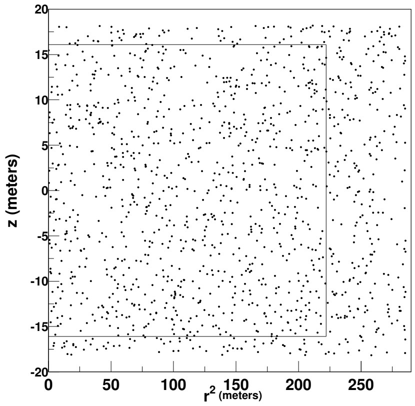

Figure 8.2: Vertex distributions for the 61 kiloton·year sub-GeV sample. Left figure is for single-ring muons and right figure is for multi-ring events.

energy of not more than 1 GeV. The vertices are uniformly distributed throughout the detector volume. To test the vertex resolution, the vertices of reconstructed Monte Carlo events are compared to the "true" vertex. Distributions of deviations from the true vertex are shown for various nucleon decay Monte Carlo samples in figure 8.3. In general, the vertex resolution is better than 25 cm. The only deviation from this is for the $p \to \bar{\nu}K^+$; $K^+ \to \mu^+\nu_\mu$ events which have less Cherenkov light yield.

8.2 Ring counting

Ring counting is the method by which the tracks of particles are found in events with more than one particle traversing the detector. Tracks are also referred to as "rings." This is based on the pattern of Cherenkov light detected on the walls of the detector. Ring counting is an important aspect of a nucleon decay analysis because most nucleon decay modes have multiple particles.

The first step to ring counting is to convert the charge distribution in the detector

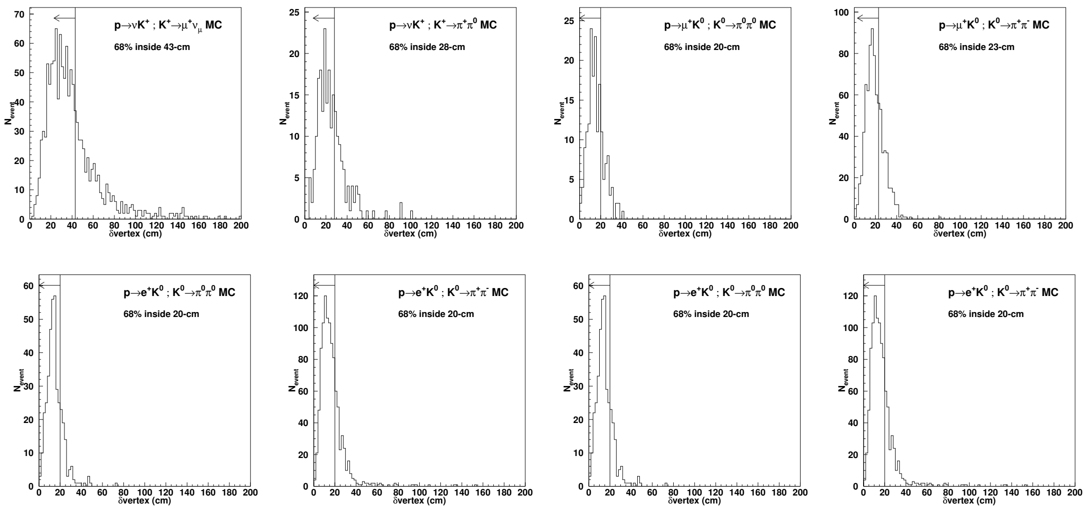

Figure 8.3: Deviation of reconstructed vertex from true vertex for various nucleon decay Monte Carlo samples.

to a Hough transform [94]. The procedure for generating a Hough transform is as follows:

1. Transform the coordinates of the PMTs from (x, y, z) to (θ, ϕ) space, relative to the vertex position.

2. Distribute the charge from each PMT evenly in a circle whose center is the PMT in (θ, ϕ) space (see figure 8.4). The radius of the circle corresponds to the Cherenkov angle.

The idea behind the Hough transform is that the circles overlap in such a way that the point of maximum intensity in the Hough space occurs in the center of the Cherenkov ring pattern. The peaks in Hough space therefore correspond to directions of the particles. A sample event and its Hough transform is shown in figure 8.5.

Four Hough transforms are created using different charge distributions which will be described later. The three highest peaks from each of the four transforms are put

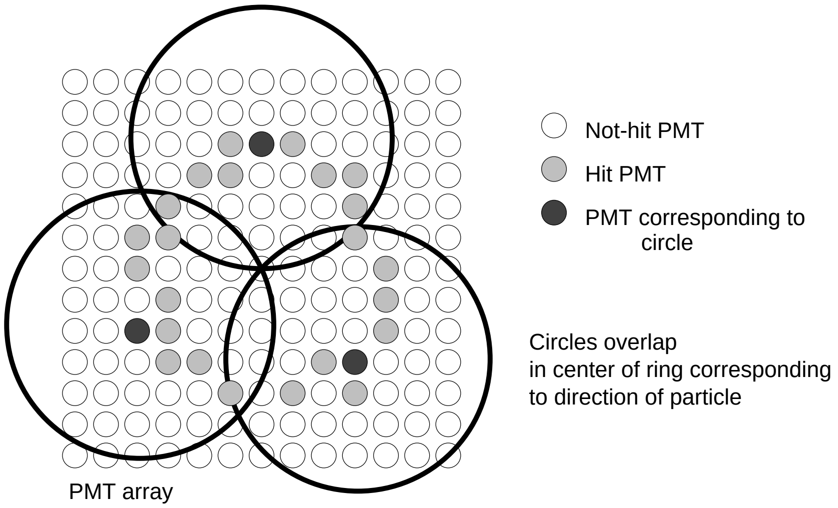

Figure 8.4: Hough transform procedure. After transforming the PMT coordinates from (x, y, z) space to (θ, ϕ) space, evenly distribute the charge from the PMT in a circle around it. The circles overlap in the center of the Cherenkov ring corresponding to the direction of the track.

into a list of "trial" rings. There is also a list of rings which have already been found which will be referred to as "fixed" rings. Each of the trial directions is tested to see if it is a ring. The testing procedure is as follows:

1. Perform charge separation on the fixed rings and the trial ring and compute the likelihood $\mathcal{L}_{trial}$. Charge separation is performed by calculating a likelihood between the actual charge distribution in the detector and the expected charge distributions for varying momenta of the list of rings. Charge is assigned to the rings at the point of maximum likelihood.

2. Perform charge separation only on fixed rings and compute the likelihood $\mathcal{L}_{fixed}$.

3. Compare the likelihood difference $\Delta\mathcal{L} = \mathcal{L}_{trial} - \mathcal{L}_{fixed}$. The trial ring with the greatest $\Delta\mathcal{L}$ which is greater than 0 is added to the list of fixed rings. The procedure is then repeated from scratch starting with creating the Hough transforms. If $\Delta\mathcal{L} < 0$ for all trial rings, the procedure is stopped.

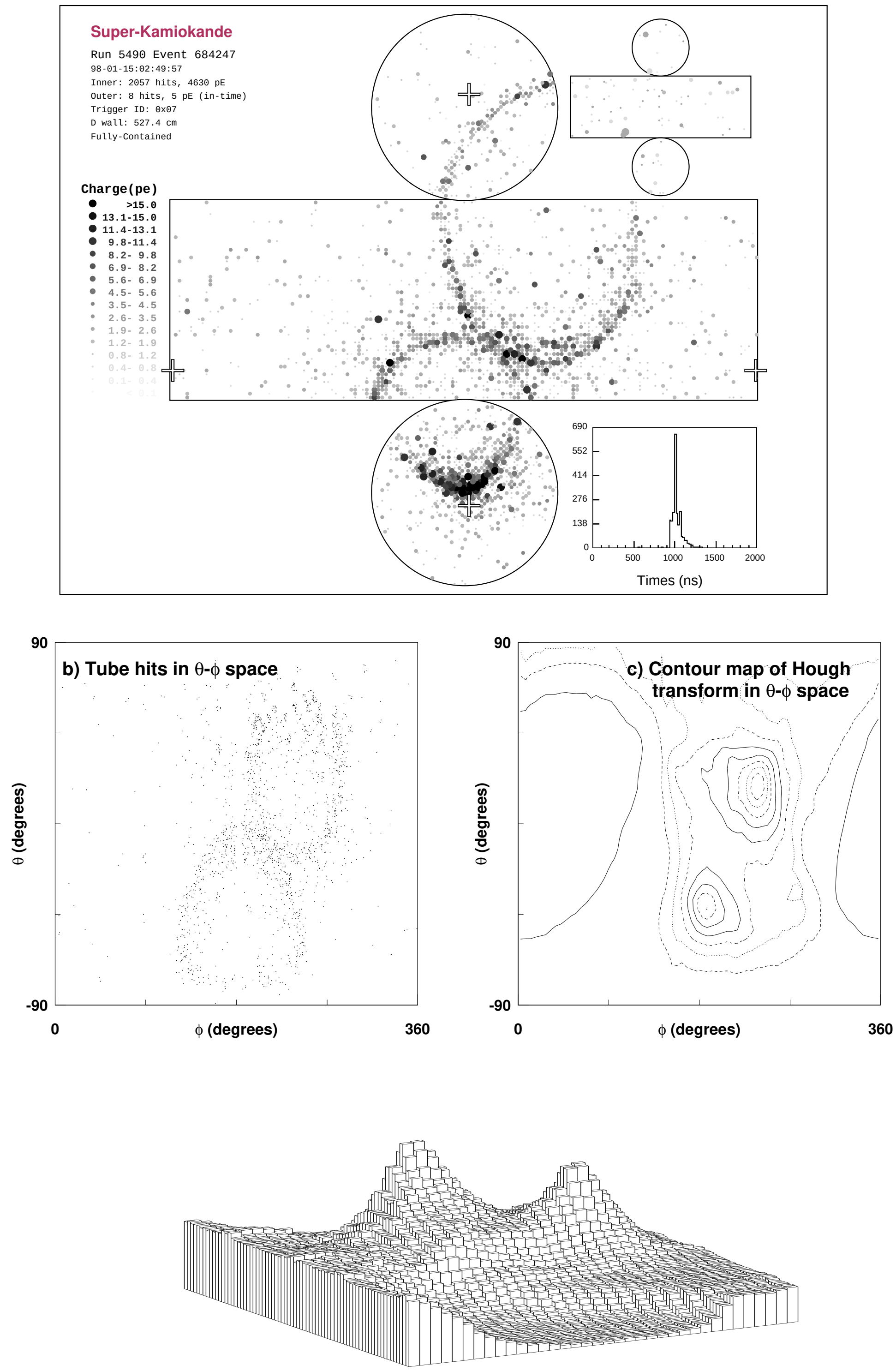

Figure 8.5: An example two-ring event and its hough transforms: a) the actual event b) tube hits in θ-ϕ space c) contour plot of Hough map d) 3-dimensional plot of Hough transform. The two peaks in Hough space can clearly be seen.

Now the four Hough transforms used to find the rings will be described. The first is created with the observed charge of the event with the expected charge of the fixed rings removed. The second is created with the fraction of charge not assigned to any of the fixed rings. The third transform is created with any charge inside a cone of 50° opening angle of any fixed rings removed. Finally there is the "clean" Hough transform which uses the first transform. A circle is centered on each point in the first transform and the place on that circle where the maximum charge occurs is entered in the "clean" space. The purpose of this is to make the peaks in the Hough space more pronounced. For each of the four variations, a separate map is made for Cherenkov angles ranging from 24 degrees to 46 degrees in steps of two degrees.

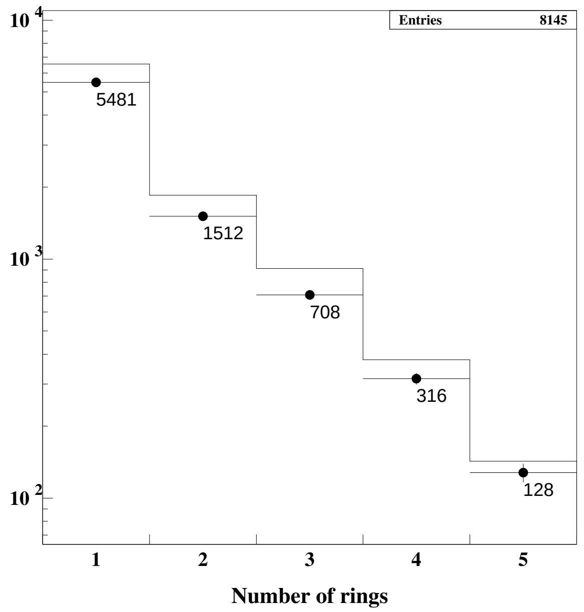

Figure 8.6: Number of rings for the 61-kton·year data sampel (points) and 40-year atmospheric neutrino Monte Carlo (normalized to the 61-kton·year livetime).

The results of the ring counting for the 61-kton·year data sample and the 40-year atmospheric neutrino Monte Carlo is shown in figure 8.6. The performance of the ring counting was checked using the "truth" information from the various nucleon decay Monte Carlo samples. Efficiency curves as a function of particle momentum are shown in figure 8.7 for the various nucleon decay samples. For the $p \to e^+K^0$ and $p \to \mu^+K^0$ Monte Carlo samples with $K_S \to \pi^0\pi^0$, the efficiency to detect the γ-rays from the π^0 becomes better than 95% for p_γ more than about 175 MeV/c. At p_γ =75 MeV/c, the efficiency is estimated to be ~20%. For $p \to \bar{\nu}K^+$; $K^+ \to \pi^+\pi^0$, the efficiency to detect the γ-rays begins to decline at p_γ=75 MeV/c and at p_γ=50 MeV/c, the efficiency is estimated to be ~30%.

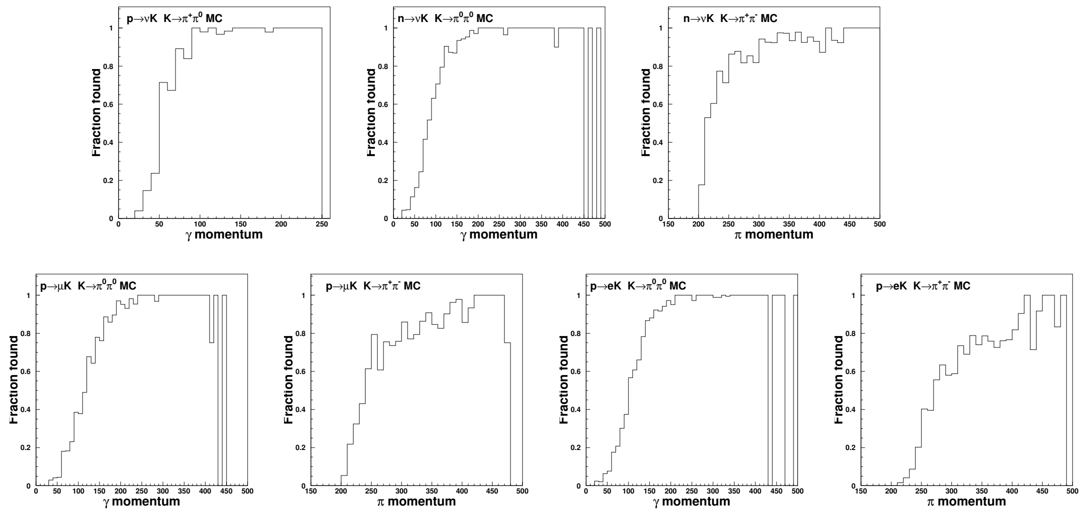

Figure 8.7: Efficiency curves as a function of particle momentum for pions and γ-rays in $p \to \bar{\nu}K^+$, $n \to \bar{\nu}K^0$, $p \to \mu^+K^0$, and $p \to e^+K^0$ Monte Carlo samples.

8.3 Particle identification

Particles are identified in Super–Kamiokande as either showering (e-like) or non-showering (μ-like). Showering particles correspond to electromagnetic showers induced by either electrons, positrons, or γ-rays. Non-showering particles are caused by heavier particles like muons, pions, and protons which do not induce electromagnetic showers. Tracks are identified as either e-like or μ-like by comparing their distribution of charge with the expected charge distributions for electrons or muons. For single ring events, the opening angle of the Cherenkov ring is also considered.

8.3.1 Electron expected PE distribution

The expected PE distribution for electrons at a distance of 16.9 -m from the electron's vertex is first estimated for the ideal case in which there is no light scattering or attenuation. This provides a template charge distribution, $Q(p_e, \theta)$, for electrons which depends on the momentum of the electron, p_e, and the opening angle, θ, between the electron's direction and the direction of Cherenkov photon. Based on vertex, direction, and the estimated momentum of particles detected in Super–Kamiokande, this template charge distribution is altered for geometrical and detector effects yielding the expected PE distribution $Q^e_{exp}(i)$ at the i-th PMT

$$Q^e_{exp}(i) = Q(p_e, \theta_i) \left(\frac{16.9 \text{ m}}{l_i}\right)^{1.5} \exp\left(\frac{l_i}{L}\right) f(\Theta) \tag{8.7}$$

where θ_i is the angle between the i-th PMT and the direction of the electron, l_i is the distance between the i-th PMT and the point of emission of Cherenkov light, L is the water attenuation length, and $f(\Theta)$ is the angular acceptance of the PMT. The exponential factor takes into account water attenuation and the factor $(16.9\text{-m}/l)^{1.5}$ takes into account the difference in dispersion between the ideal case calculated for 16.9-m path length and the actual case of l path length. A sample expected PE distribution for a 525-MeV electron is shown in figure 8.8. This is to be compared with the actual angular charge distribution shown in figure 8.1.

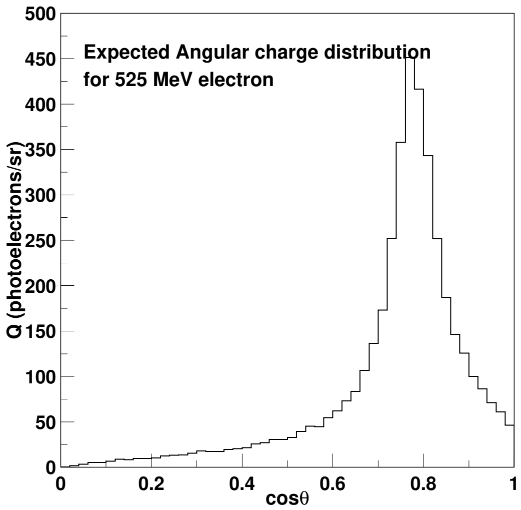

Figure 8.8: The expected angular photoelectron distribution corresponding to a 525-MeV electron. This distribution takes into account detector effects like geometry and light attenuation.

8.3.2 Muon expected PE distribution

The expected PE distribution for μ-like events takes into account the decreasing Cherenkov angle when heavier particles lose energy when traversing the detector. The distribution is given by

$$Q^{\mu}_{exp}(i) = \left[\frac{\alpha_\mu \sin^2\theta_i}{l_i\left(\sin\theta_i + l_i\frac{d\theta_c}{dr}\right)} + Q^{\delta}(i)\right] \exp\left(\frac{l_i}{L}\right) f(\Theta) \tag{8.8}$$

where α_μ is a normalization factor, $l_i(\sin\theta_i + l_i\frac{d\theta_c}{dr})$ accounts for the decrease in Cherenkov angle with path length, and Q^{δ}_i is the contribution from delta-ray production. The parameters l_i, L, θ_i, and $f(\Theta)$ are the same as in equation 8.7. A sample expected angular PE distribution for a 725-MeV muon is shown in figure 8.9.

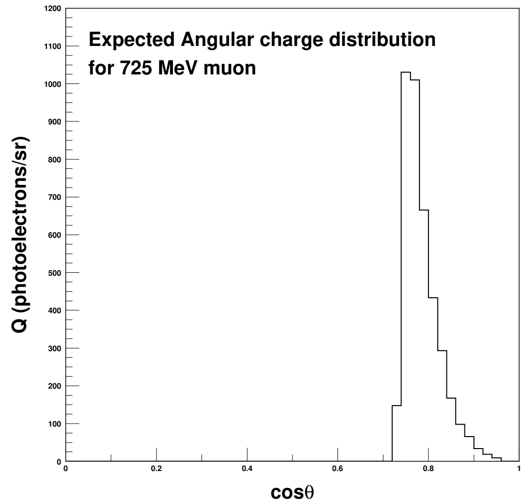

Figure 8.9: The expected angular photoelectron distribution corresponding to a 725-MeV muon.

8.3.3 Particle identification parameter

After the expected charge distributions are generated for the showering and non-showering scenarios, they are compared to the actual charge distribution detected in Super–Kamiokande and a likelihood is calculated for the two.

$$\mathcal{L}(e,\mu) = \prod_i P\left(t_i, Q_{obs}(i), Q^{e,\mu}_{exp}(i)\right) \tag{8.9}$$

where i represents the i-th PMT lying within an angle of $1.5\,\theta_C$ relative to the direction of the particle. To account for scattered light the probability function depends on the time t_i of the PMT.

$$\begin{aligned} P^{e,\mu} &= p\left(Q^{e,\mu}_{exp,direct}(i), Q_{obs}(i)\right) && -30 \text{ ns} < t - t_0 < 2\sigma + 5 \text{ ns} \\ &= p\left(Q^{e,\mu}_{exp,direct}(i), 0\right)\, p(Q^{e,\mu}_{exp,scatt}(i), Q_{obs}(i)) && \text{otherwise} \end{aligned} \tag{8.10}$$

The first is the probability function used for direct Cherenkov light and the second is used for scattered light. The $p\,(Q_{exp}, Q_{obs})$ is the probability to observe Q_{obs} PE with and expectation of Q_{exp}. For $Q_{obs} < 20$ PE, this is derived from the measured single-PE distribution. For $Q_{obs} \geq 20$ PE it is a Gaussian

$$p(Q_{exp}, Q_{obs}) = \frac{1}{\sqrt{2\pi}\sigma} \exp\left(-\frac{(Q_{exp} - Q_{obs})^2}{2\sigma^2}\right) \tag{8.11}$$

where $\sigma^2 = 1.2^2\, Q_{exp} + (0.1\, Q_{exp})^2$. The second factor accounts for the uncertainty in the relative gain of the PMT. The factor of 1.2 accounts for the actual uncertainty in the PMT resolution compared to the ideal case.

For single ring events, the opening angle of the Cherenkov ring is taken into account. Heavier particles like pions, muons, and protons with $\beta < 1$ generate Cherenkov cones with smaller opening angles . Based on the reconstructed momentum an expected Cherenkov angle, θ_{exp}, is determined. From this, a probability is computed

$$P_\theta^{e,\mu} = A\ \exp\left(-\frac{(\theta_{exp}^{e,\mu} - \theta_{obs})^2}{\sigma_\theta^2}\right) \tag{8.12}$$

where σ_θ is the uncertainty in the Cherenkov angle.

The probabilities for the showering and non-showering scenarios and opening angle are then combined into a total probability

$$\begin{aligned} P_{tot}^{e,\mu} &= P_\theta^{e,\mu} P^{e,\mu} \qquad && nring = 1 \\ &= P^{e,\mu} && nring > 1 \end{aligned} \tag{8.13}$$

The final particle identification parameter is based on a log likelihood method:

$$PID = \sqrt{-\log_{10} P_{tot}^{\mu}} - \sqrt{-\log_{10} P_{tot}^{e}} \tag{8.14}$$

The distributions of the particle identification parameter for the sub-GeV single ring sample is shown in figure 8.10.

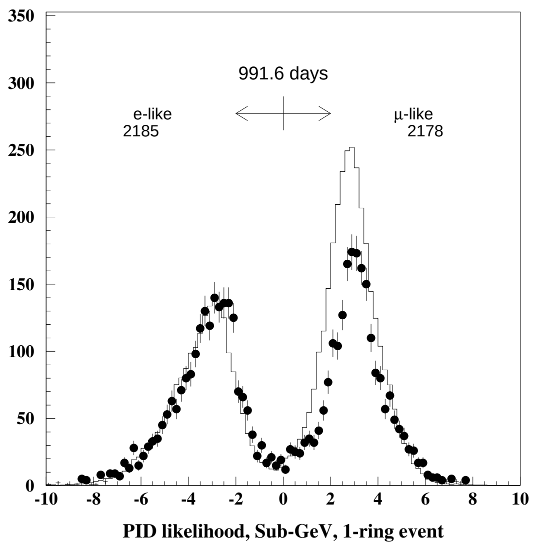

Figure 8.10: The particle identification parameter for single ring sub-GeV events for the 991-day exposure of Super–Kamiokande (points with error bars) and the (normalized) 40-year equivalent sample of atmospheric neutrino Monte Carlo.

8.4 Momentum determination

To determine the momentum of a particle, the total charge corresponding to the particle is calculated by summing the charge from PMTs satisfying the following criteria:

1. $\theta_i < 70°$

2. $-50 \text{ ns} \ < \ t_0 - t_i^{resid} \ < \ 250 \text{ ns}$

where θ_i is the angle between the direction of the particle and the i-th PMT, t_i^{resid} is the time-of-flight subtracted time of the PMT, and t_0 is the average of the residual times. These criteria reject any scattered light. Once the charge is known, a conversion to momentum is applied. This conversion is based on the energy calibration sources described in section 5.5. The converstion for electrons and muons is shown in figure 8.11. The resolution in the momentum determination for electrons and muons is estimated to be

$$\sigma_e = \left[0.6 + \frac{2.6}{\sqrt{|\vec{p}_e|}}\right]\% \tag{8.15}$$

$$\sigma_\mu = \left[1.7 + \frac{0.7}{\sqrt{|\vec{p}_\mu|}}\right]\% \tag{8.16}$$

where $\vec{p}_e$ and $\vec{p}_\mu$ are the momenta of the electron and muon, respectively. The momentum for charged pions is calculated using both the opening angle of the track and the number of PE belonging to the track.

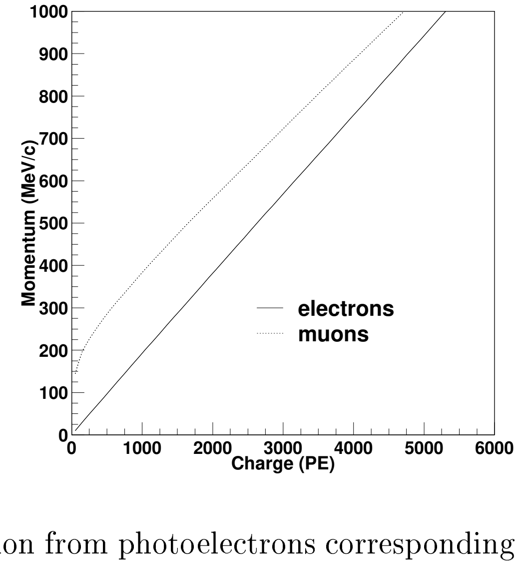

Figure 8.11: Conversion from photoelectrons corresponding to a track to momentum for electrons and muons.

8.5 muon/shower (MS) fit

For single ring events, the vertex is refined using "MS-fit" ("muon/shower" fit). In addition to timing information, MS-fit uses the Cherenkov light patterns for e-like and μ-like tracks (see section 8.3 for a description of these patterns). The timing information provides a good fit in the direction perpendicular to the track of the particle. The vertex is refined in the direction parallel to the track of the particle by maximizing the likelihood defined in equation 8.13 for vertices offset from the original vertex.

8.6 Decay electron counting

Electrons from muon decay can occur either in the same event as the main trigger or can produce a trigger themselves. These two scenarios have separate search methods.

For decays occuring within the main trigger, the main trigger is found by searching the time-of-flight (TOF) subtracted timing distribution for the maximum peak. From this point, decays are searched by looking for the maximum number of hits within a 30-ns sliding time window. Decay electrons are tagged by requiring that

1. $t\ >\ 100$ ns
2. $t\ < 800$ ns
3. $N_{hit}^{30\,ns} \geq 60$
4. $G_{point} > 0.5$

Where t denotes the time of the decay electron, $N_{hit}^{30\,ns}$ is the number of hits within the 30-ns time window, and goodness G_{point} is defined with equation 8.1. The first two criteria reflect the fact that the detection efficiency decreases when the decay is too close to the main peak and when it is too close to the end of the gate. Criteria 3 and 4 ensure that the hit tubes are from an electron.

Decays occuring in separate triggers are selected by requiring

1. $t^{sub} < 20\ \mu$s
2. $t > 1.2\ \mu$s
3. $N_{hit}^{30\,ns} \geq 40$
4. $G_{point} > 0.5$

The first criterion rejects after-events which occur many muon lifetimes after the initial event. The second criterion ensures that the detection efficiency remains constant over the entire time window. Finally criteria 3 and 4 ensure a good fit of the Cherenkov ring from the electron.

From Monte Carlo studies, the efficiencies to detect decay electrons from μ^+ and μ^- are estimated to be 80% and 63%, respectively. These efficiencies were checked using stopping cosmic-ray muons and were found to be accurate to within 1.5%.

Chapter 9

The Search for Nucleon Decay

The strategy for a nucleon decay analysis is straightforward. Monte Carlo events of the decay mode being studied are generated with the aid of methods using nuclear physics (see section 6.1) and detector response to particles traversing Super–Kamiokande. This gives a picture of how nucleon decay into that specific mode will look inside the detector. In addition, Monte Carlo events for the background induced by atmospheric neutrinos are generated. In this dissertation, a 40-year equivalent sample of atmospheric neutrino Monte Carlo was used to estimate the background. Based on the simulated signal and simulated background, selection criteria are generated. After the selection criteria are decided upon, they are applied to real data from Super–Kamiokande to search for nucleon decays.

This chapter describes the search for nucleon decay via $p \to \bar{\nu} K^+$, $n \to \bar{\nu} K^0$, $p \to \mu^+ K^0$, and $p \to e^+ K^0$ using a 61-kton·year (991-days) exposure of Super–Kamiokande. Each section describes a particular decay mode in detail, however at the end of the chapter there are tables summarizing the selection criteria and results of the searches.

9.1 $p \to \bar{\nu} K^+$

The K^+ in the decay $p \to \bar{\nu} K^+$ has a β of only $\sim$.6, which is below Cherenkov threshold in water. Therefore it can not be observed directly in Super–Kamiokande. However, candidate events are observed indirectly through the decay products of the K^+. The major decay modes are $K^+ \to \mu^+ \nu_\mu$ and $K^+ \to \pi^+ \pi^0$ with branching ratios of 63.5% and 21.2%, respectively. Because the hadronic cross-section for low momentum kaons to interact inelastically is small, more than 90% of them stop before decaying. The search for $p \to \bar{\nu} K^+$ then becomes a search for K^+ decays at rest.

9.1.1 $K^+ \to \pi^+ \pi^0$

The π^0 and π^+ from the K^+ decay at rest have equal and opposite momenta of approximately 205 MeV$/c$. The γ-rays from the decay of the π^0 completely reconstruct this momentum. The π^+, barely over Cherenkov threshold with $\beta \approx .86$, produces a small amount of Cherenkov radiation which can be detected in the direction opposite that of the π^0. To quantify this, "backwards charge" (Q_{back}) is defined as the sum of the PEs measured by the PMTs which lie within a cone of 40° opening angle whose axis is the opposite direction of the reconstructed direction of the π^0. This charge is corrected for light attenuation in the water and the angular dependence of photon acceptance of the PMTs. In addition, the π^+ decays into a muon ($\pi^+ \to \mu^+ \nu_\mu$; lifetime $\tau = 2.6 \times 10^{-8}$ ns) which decays into a positron ($\mu^+ \to e^+ \nu_e \bar{\nu}_\mu$; lifetime $\tau = 2.2 \times 10^{-6}$ ns). Detection of the positron is possible. A sample event display of a Monte Carlo event in "unrolled" and "front-back" views is shown in figure 9.1. The "unrolled" view is the cylindrical structure of Super–Kamiokande with the top folded up, the bottom folded down, and the sides rolled out. The "front-back" view is a hemispherical view with PMTs plotted in the θ-ϕ coordinate system relative to the reconstructed vertex position. In the "front-back" view of figure 9.1, the γ-rays from the π^0 decay can be seen in the left hemisphere and a collapsed Cherenkov ring from the π^+ can be seen in the right hemisphere.

Based on the nucleon decay Monte Carlo simulation and the 40-year equivalent atmospheric neutrino Monte Carlo simulation, the following selection criteria were decided upon:

A1. two e-like rings

A2. one decay electron

A3. 85 MeV/c^2 < $M_{\gamma\gamma}$ < 185 MeV/c^2

A4. 175 MeV/c < $|\vec{p}_{\gamma\gamma}|$ < 250 MeV/c

A5. 40 PE < Q_{back} < 100 PE

where $|\vec{p}_{\gamma\gamma}|$ is the sum of the momenta of the two e-like rings and $M_{\gamma\gamma}$ is the invariant mass of the two e-like rings which is calculated using the kinematic relation

$$m^2 = E_{\gamma\gamma}^2 - \vec{p}_{\gamma\gamma}{}^2 \tag{9.1}$$

The invariant mass distributions for both $p \rightarrow \bar{\nu}K^+;K^+ \rightarrow \pi^+\pi^0$ and atmospheric neutrino Monte Carlo events which passed criteria A1 and A2 are shown in figure 9.2. Criteria A1, A3, and A4 search for the π^0 with the monochromatic momentum expected. Criterion A3 is centered around the π^0 mass of about 135 MeV/c^2. Criterion A2 is a search for the decay of the π^+ into muon into positron and criterion A5 searches for Cherenkov light from the π^+. For $p \rightarrow \bar{\nu}K^+$; $K^+ \rightarrow \pi^+\pi^0$ Monte Carlo events, the resolution of vertex fitting was estimated to be ~28 cm (figure 8.3) and 66% of the events were identified as having two rings.

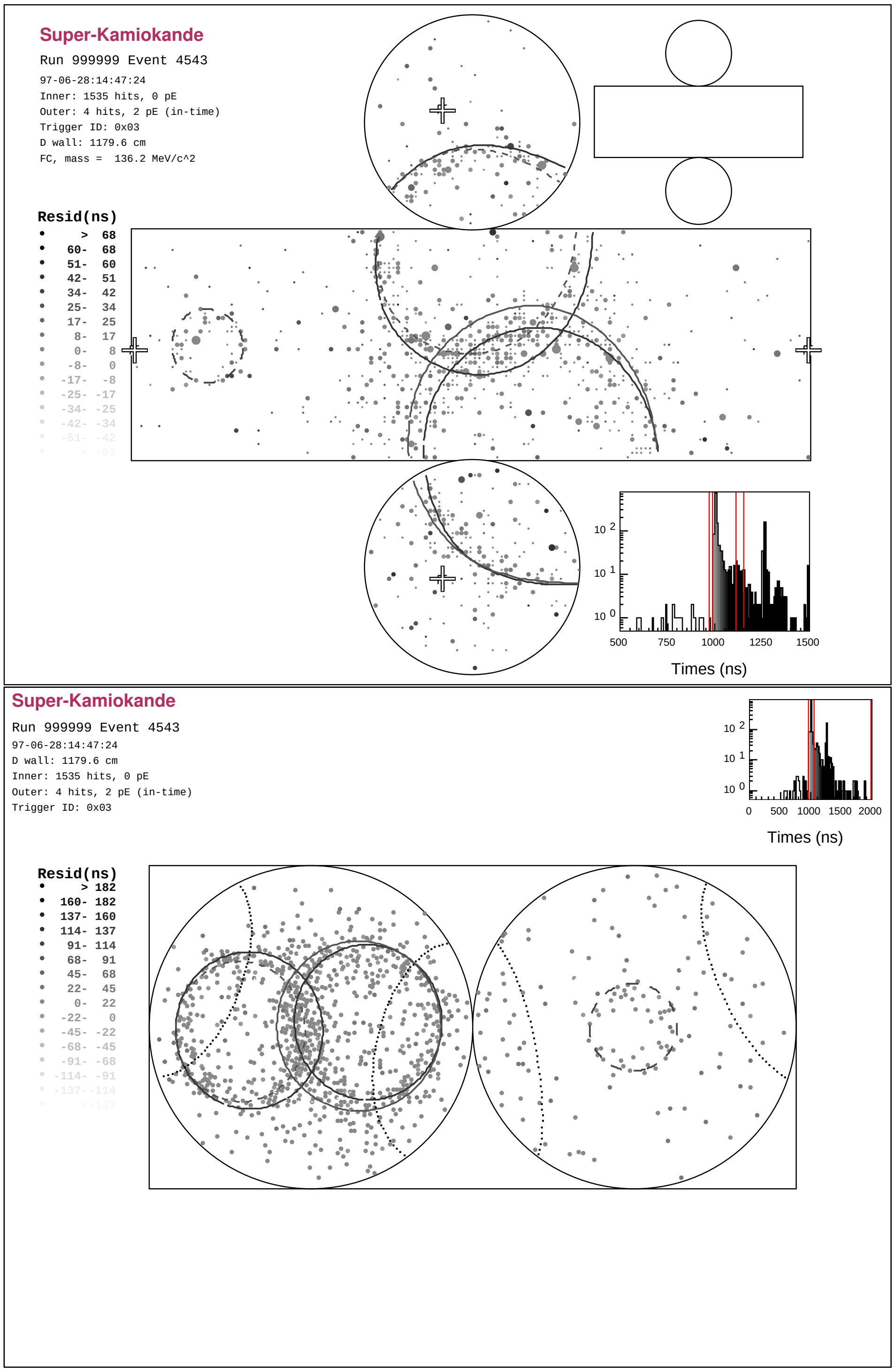

Figure 9.1: $p \to \bar{\nu} K^+$; $K^+ \to \pi^+ \pi^0$ Monte Carlo event in unrolled view and front-back view. The two γ-rays from the decay of the π^0 can be seen clearly in both views. A collapsed Cherenkov ring from the π^+ can be seen in the backwards hemisphere (right circle) in the front-back view. The spike in the time histogram around 1250 ns is from the decay electron.

It is appropriate to now describe the two methods used to decide upon the selection criteria depending on the kinematics of the event (A3, A4, and A5). These methods were used to decide upon selection criteria in all modes. Criteria A3 and A4 were chosen by finding the center of the signal distribution and selecting symmetric cuts so that approximately 95% of the events passed. This method assumes a flat background distribution. Criterion A5 was chosen by maximizing $S/\sqrt{N}$, where S is the number of signal events passing and N is the number of background events passing. In general, initial kinematic criteria were determined using the first method. Final kinematic cuts on parameter spaces with significant background were decided upon using the second method, while parameter spaces with little background the first method was used to determine final kinematic criteria.

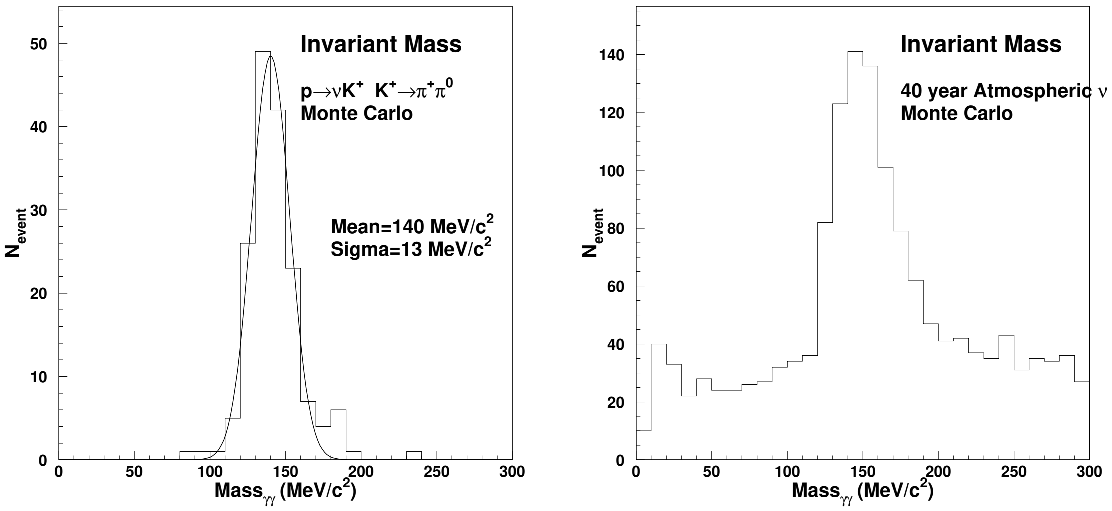

Figure 9.2: Invariant mass distribution for events passing criteria A1 and A2 for $p \to \bar{\nu}K^+;K^+ \to \pi^+\pi^0$ Monte Carlo and the 40-year equivalent sample of atmospheric neutrino Monte Carlo.

By passing the $p \to \bar{\nu}K^+;K^+ \to \pi^+\pi^0$ Monte Carlo events through selection criteria A1-A5, the detection efficiency was determined to be 31%. The major contribution to the inefficiency was the detection of two γ-rays from the decay of the π^0. Including the kaon branching ratio of 21.2% into $\pi^+\pi^0$, the total detection efficiency for this mode was estimated to be 6.8%.

The selection criteria were applied to the sample of 40-year equivalent atmospheric neutrino Monte Carlo and the number of background events expected in the 61-kton·year exposure of Super–Kamiokande was estimated to be 1.7 events. This normalized background was estimated using the methods described in section 6.2.4 (all quoted background estimates will be normalized according to this procedure). Figure 9.3 shows the distribution of Q_{back} vs. $|\vec{p}_{\gamma\gamma}|$ for $p \rightarrow \bar{\nu}K^+; K^+ \rightarrow \pi^+\pi^0$ Monte Carlo and the 40-year sample of atmospheric neutrino Monte Carlo for events passing selection criteria A1-A3.

The breakdown of the types of neutrino interactions which appear in the background estimate is shown in table 9.1. Most of the background is from single-π and multi-π production. The major contribution of the multi-π production is in the lower energy scheme of 1.4 GeV to 2.0 GeV neutrino-nucleon invariant mass. The incoming neutrino energy of the background is typically between 600 MeV and 2 GeV.

The selection criteria for this decay mode were applied to the 61-kton·year data sample. Figure 9.4 shows the results of the final two cuts. No events pass. Based on the estimated detection efficiency and background estimation, a lower limit on the partial lifetime of $p \rightarrow \bar{\nu}K^+$ of 6.0×10^{32} yr at the 90% C.L. was set. For an explanation on setting a limit see appendix A.

9.1.2 $K^+ \rightarrow \mu^+\nu_\mu$

The μ^+ from the decay $K^+ \rightarrow \mu^+\nu_\mu$ at rest has a monochromatic momentum of 236 MeV/c, a region highly contaminated by atmospheric neutrinos. However, if a

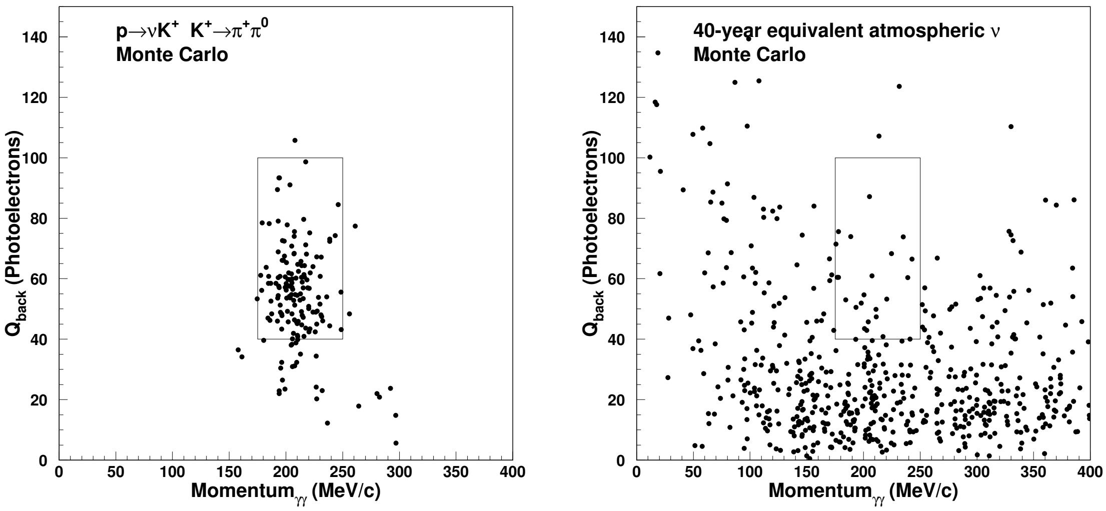

Figure 9.3: Q_{back} vs. $|\vec{p}_{\gamma\gamma}|$ for $p \rightarrow \bar{\nu}K^+;K^+ \rightarrow \pi^+\pi^0$ and 40-year atmospheric neutrino Monte Carlo samples. The Q_{back} cut is asymmetric because it maximizes $S/\sqrt{N}$.

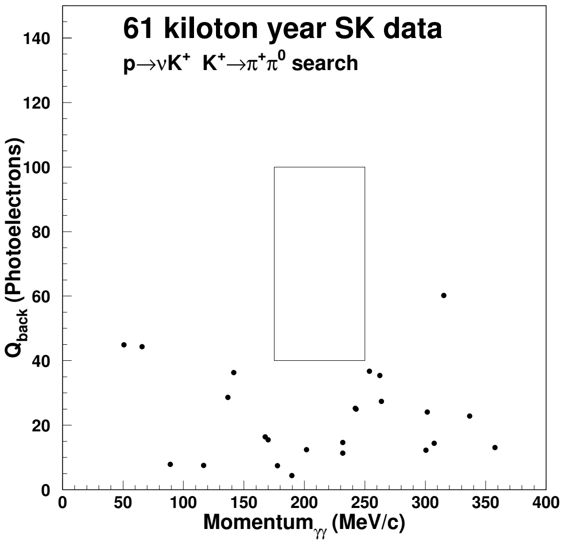

Figure 9.4: Q_{back} vs. $|\vec{p}_{\gamma\gamma}|$ distribution for 61-kton·year data. No events pass the selection criteria.

Background for $p \to \bar{\nu} K^+$; $K^+ \to \pi^+ \pi^0$					
interaction		$\nu_e + \bar{\nu}_e$		$\nu_\mu + \bar{\nu}_\mu$	
		N_{norm}	%	N_{norm}	%
CC	quasi-elastic	-	-	-	-
	single-π	3.5	11.8%	5.2	20.5%
	multiple-π	2.3	9.0%	5.2	20.5%
	K prod.	-	-	-	-
	η prod.	-	-	-	-
NC	quasi-elastic	-	-	-	-
	single-π	1.2	4.6%	-	-
	multiple-π	3.3	13.0%	3.5	13.8%
	K prod.	-	-	-	-
	η prod.	1.2	4.6%	-	-
TOTALS		11.5	45%	13.9	55%

Table 9.1: Breakdown of background contributions to the decay $p \to \bar{\nu} K^+$; $K^+ \to \pi^+ \pi^0$. N_{norm} is the number normalized to the neutrino oscillation hypothesis (see section 6.2.4 for an explanation). The % is the normalized percentage contribution to the background.

nucleon which is not in the outermost nuclear shell of O^{16} decays, the remaining N^{15} nucleus is left in an excited state. This excited state of N^{15} can decay in different ways. Table 6.1 lists the modes which have a γ-ray in the final state. The case where a proton of O^{16} in the $p_{3/2}$ state decays leading to a prompt 6.3-MeV γ-ray emission from the excited N^{15} is the most prominent with a probability of 41%[67].

Due to the K^+ lifetime of 12 ns, the signal from its decay products will be delayed relative to the signal from the de-excitation of the N^{15}. The timing resolution in Super-Kamiokande enables these two signals to be clearly separated within an event. A timing distribution corrected for time of flight for a $p \to \bar{\nu} K^+$; $K^+ \to \mu^+ \nu_\mu$ Monte Carlo event with the N^{15} decay emitting a prompt 6.3-MeV γ-ray is shown in figure 9.5.

The search for the decay mode $p \to \bar{\nu} K^+$;$K^+ \to \mu^+ \nu_\mu$ was performed by first searching for a muons with a monochromatic momentum of 236 MeV/c. The selection

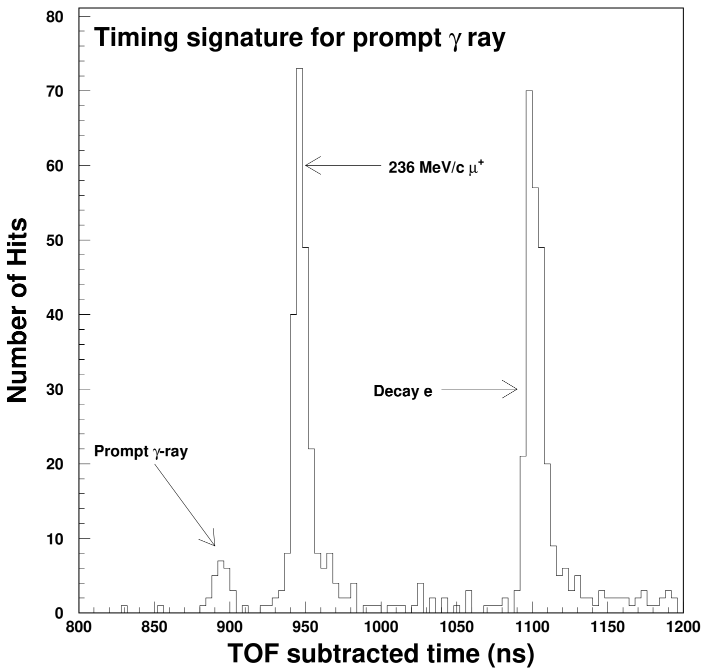

Figure 9.5: Sample time of flight (TOF) subtracted timing distribution for a $p \to \bar{\nu}K^+$; $K^+ \to \mu^+\nu_\mu$ Monte Carlo event with prompt γ-ray emission.

criteria for such events were determined to be:

B1. one μ-like ring

B2. one decay electron

B3. 215 MeV/c < $|\vec{p}_\mu|$ < 260 MeV/c

B4. "proton" event rejection

Criteria B1-B3 are a selection of a 236-MeV/c monochromatic muon. Criterion B4 rejects events which are caused by neutral current reactions where a large amount of momentum is transferred to a proton, ejecting it from the O^{16} nucleus. These recoil protons can have momenta that are above Cherenkov threshold making them visible in the detector. The Cherenkov rings produced by such protons appear to be μ-like, however they have a smaller opening angle. Therefore when they are fit as muons the vertex is shifted a large amount and the γ-rays from the nuclear deexcitation associated with such reactions can appear at an earlier time. These events can be rejected by calculating a goodness of fit. Cherenkov rings from protons have a different characteristic than muons and this can be parameterized by the goodness of fit. More details of the proton rejection criterion can be found in reference [95].

After selection criteria B1-B4 are applied, events are classified into two groups, "prompt γ detection" and "no prompt γ detection." These are independent event samples from which limits can be drawn and combined.

To describe the search for the prompt γ-ray, three quantities must be defined. The first is t_0 which is a reference time associated with the detection of the muon. The second is t_1 which is the time before t_0 from which to begin a backwards search in time for the earlier hits from the prompt γ ray. Finally, t_{win} is the width of the timing window in which hits are summed. A graphical description of these three quantities is shown in figure 9.6.

The reference point t_0 corresponding to the muon was found by searching for the point in time when:

$$\left.\frac{dN_{hit}}{dt}\right|_{t=t_0} = max\left[\frac{dN_{hit}}{dt}\right] \tag{9.2}$$

After t_0 was found, PMTs which were within a cone of 50° opening angle relative to the direction of the muon were removed. Removing these tubes enabled the search for the prompt γ to start at an earlier time. With the remaining tubes, a backwards scan of dN_{hit}/dt was made starting at t_0. The starting time t_1 was then defined as the first point less than t_0 where $dN_{hit}/dt = 0$. Once t_1 was found, a time window of width $t_{win} = 12$ ns was slid backwards starting with its trailing edge at t_1. The hits

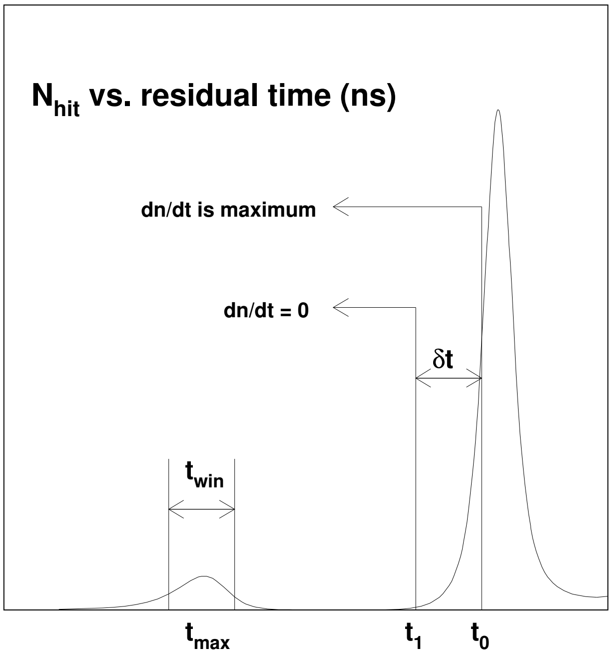

Figure 9.6: Description of quantities used in the prompt γ-ray search.

falling within t_{win} were summed and the maximum number of hits falling within t_{win} was then defined as $N_{hit}^{12\,ns}$. This defined the final selection criterion:

B5. $N_{hit}^{12\,ns} > 7$

Passing the $p \to \bar{\nu}K^+ ; K^+ \to \mu^+\nu_\mu$ prompt γ Monte Carlo and 40-year atmospheric neutrino Monte Carlo through criteria B1-B5 the detection efficiency and background were estimated to be 9.3% and 1 event, respectively. The efficiency includes all branching ratios. Passing the 61-kton·year data through this reduction yielded no events, therefore a lower limit on the partial lifetime of $p \to \bar{\nu}K^+$ was set to be 8.2×10^{32} years at the 90% confidence level. Figure 9.7 shows N_{hit}^{12ns} for the normalized 40-year sample of atmospheric neutrino Monte Carlo, $p \to \bar{\nu}K^+ ; K^+ \to \mu^+\nu_\mu$ Monte Carlo normalized to 2.3 events/61-kton·year in the signal region, and 61-kton·yr

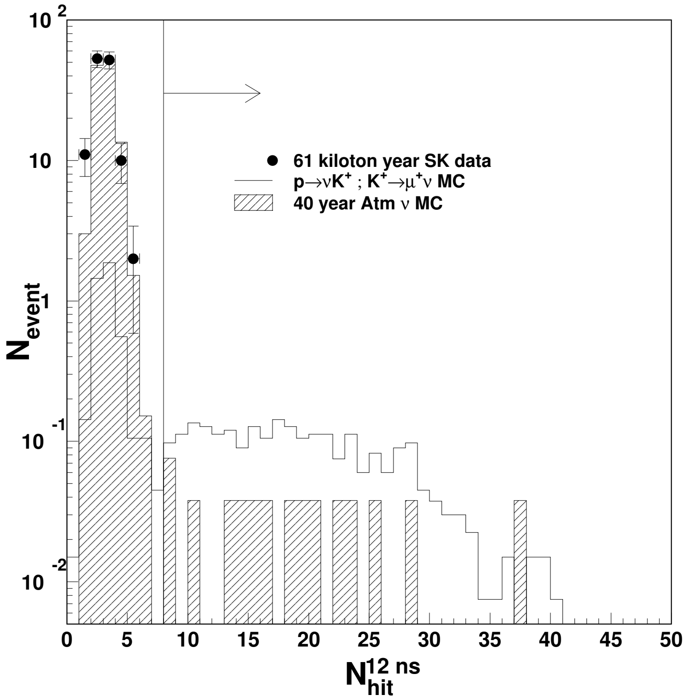

Figure 9.7: N_{hit}^{12ns} distributions for $p \to \bar{\nu}K^+;K^+ \to \mu^+\nu_\mu$ Monte Carlo, 40-year equivalent Monte Carlo event samples, and 61-kton·year SK data. The $p \to \bar{\nu}K^+;K^+ \to \mu^+\nu_\mu$ Monte Carlo was normalized to 2.3 events/61 kton·year.

sample of data.

The events passing criteria B1-B2 but failing B5 were then searched for an excess within the momentum range around the monochromatic momentum of the muon. The method of estimating the excess was developed by Y. Hayato [95]. The number of events in three momentum regions, 200 to 215 MeV/c, 215 to 260 MeV/c, and 260 to 300 MeV/c were summed separately for $p \to \bar{\nu}K^+$; $K^+ \to \mu^+\nu_\mu$ Monte Carlo, atmospheric neutrino Monte Carlo, and the 61-kton·yr data sample. The χ^2 method was applied to fit normalization parameters for the MC samples to the data. The χ^2

Background for $p \to \bar{\nu} K^+$; $K^+ \to \mu^+ \nu_\mu$ prompt γ-ray search					
interaction		$\nu_e + \bar{\nu}_e$		$\nu_\mu + \bar{\nu}_\mu$	
		N_{norm}	%	N_{norm}	%
CC	quasi-elastic	-	-	4.4	30.8%
	single-π	-	-	2.2	15.4%
	multiple-π	-	-	-	-
	K prod.	-	-	0.7	4.9%
	η prod.	-	-	-	-
NC	quasi-elastic	-	-	2.3	16.1%
	single-π	-	-	1.2	8.3%
	multiple-π	1.2	8.3%	2.3	16.1%
	K prod.	-	-	-	-
	η prod.	-	-	-	-
TOTALS		1.2	8.3%	13.1	91.7%

Table 9.2: Breakdown of background contributions to the decay $p \to \bar{\nu} K^+$; $K^+ \to \mu^+ \nu_\mu$ with a prompt-γ ray emission. (See table 9.1 for an explanation of N_{norm} and %.)

function was defined as:

$$\chi^2 = \sum_{i=1}^{3} \frac{\left[N_i^{data} - \left(aN_i^{atm\nu} + bN_i^{pdk}\right)\right]^2}{N_i^{data}} \tag{9.3}$$

where a and b are the normalization parameters for atmospheric neutrino and proton decay Monte Carlo samples and N_i^{data}, N_i^{pdk}, and $N_i^{atm\nu}$ are the numbers of events of real data, proton decay MC, and atmospheric neutrino MC, respectively, in each momentum region i.

The minimum $\chi^2 = 0.853$ was in the unphysical region where the excess of proton decay signal was estimated to be negative, $bN_2^{pdk} = -26.76$. The minimum χ^2 in the physical region was 3.49 where $bN_2^{pdk} = 0$. The 90% confidence level upper limit on the number of events from proton decay was obtained by requiring that $\chi^2_{90\%C.L.} - \chi^2_{min} = 7.3$ using the method outlined in reference [96]. The 90% confidence level on the upper limit of the number of events from proton decay was obtained to be 15.6. The fitted momentum spectrum for events passing criteria B1 and B2 is shown in figure 9.8 which shows the 61-kton·year data, the fitted atmospheric neutrino Monte Carlo, and the 90% C.L. on the excess of signal added to the fitted atmospheric neutrino Monte Carlo. Using this spectrum fitting method the lower limit on the partial lifetime of $p \rightarrow \bar{\nu} K^+$ was found to be 4.3×10^{32} years (90% C.L.).

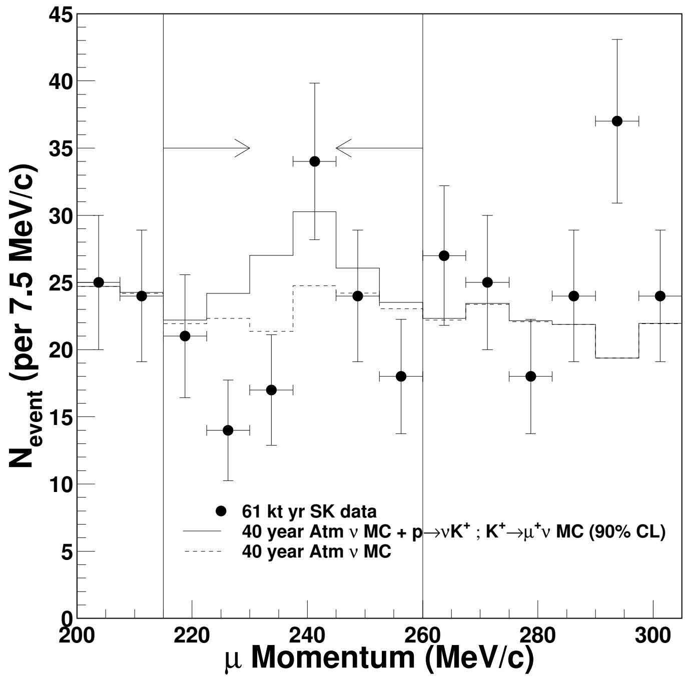

Figure 9.8: Momentum spectrum for events passing criteria B1-B2. The points with error bars are the data, the solid line is the 90% C.L. upper limit on the excess of signal events with the atmospheric neutrino Monte Carlo events, and the dashed line is the same as the solid line with the signal excess removed.

Method	efficiency	N_{BG}^{exp}	N_{obs}	s_{90}	τ/B (90% CL)
$K^+ \rightarrow \pi^+\pi^0$	6.8%	1.7	0	2.3	6.0×10^{32} years
$K^+ \rightarrow \mu^+\nu_\mu$ prompt γ	9.3%	1.0	0	2.3	8.2×10^{32} years
$K^+ \rightarrow \mu^+\nu_\mu$ spectrum fit	33%	137	128	15.6	4.3×10^{32} years
combined	49%	-	-	6.2	1.7×10^{33} years

Table 9.3: Summary of three methods used to search for $p \rightarrow \bar{\nu}K^+$.

9.1.3 Final Limit of $p \rightarrow \bar{\nu}K^+$

Table 9.3 summarizes the search for $p \rightarrow \bar{\nu}K^+$ via the three methods: $K^+ \rightarrow \pi^+\pi^0$, $K^+ \rightarrow \mu^+\nu_\mu$ prompt γ, and $K^+ \rightarrow \mu^+\nu_\mu$ spectrum fitting. No evidence for $p \rightarrow \bar{\nu}K^+$ was found in these data, therefore the three limits were combined using the method described in appendix A. The combined lower limit of the partial lifetime for $p \rightarrow \bar{\nu}K^+$ using the three methods was 1.7×10^{33} years at the 90% C.L. This can be compared to previous limits of 1.8×10^{32} years set by IMB [12] and 1.0×10^{32} years set by Kamiokande [58].

9.2 $n \rightarrow \bar{\nu}K^0$

The K^0 is a linear superposition of the CP eigenstates K_S and K_L by which it decays. In this dissertation, only decays of K_S were studied because the lifetime of K_L is long enough so that it has a very high probability of interacting in water before decaying. Such interactions destroy the signature of these events. Two decay modes of K_S were used, $K_S \rightarrow \pi^0\pi^0$ and $K_S \rightarrow \pi^+\pi^-$.

9.2.1 $K_S \rightarrow \pi^0\pi^0$

The decay $K_S \rightarrow \pi^0\pi^0$ is characterized by four electromagnetic showers from the decays of the two π^0s. A sample $n \rightarrow \bar{\nu}K^0; K_S \rightarrow \pi^0\pi^0$ event is shown in figure

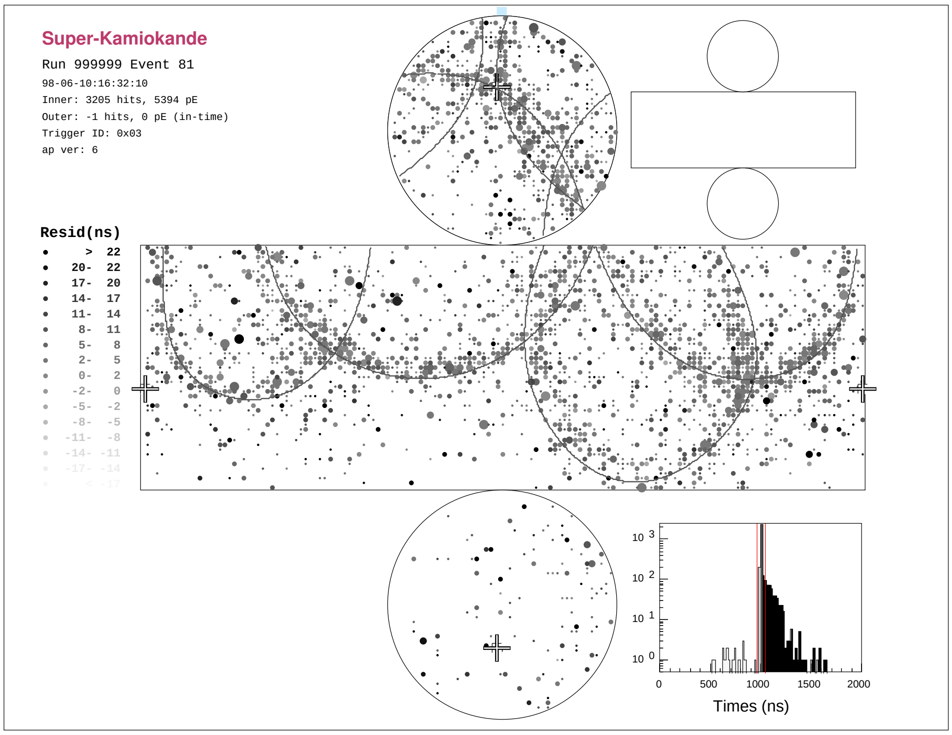

Figure 9.9: $n \to \bar{\nu} K^0$; $K_S \to \pi^0 \pi^0$ Monte Carlo event.

9.9. The K_S decays in flight and the energies and momenta from the γs completely reconstruct its mass and momentum. The selection criteria were selected to be:

C1. three or four e-like rings

C2. no decay electrons

C3. 400 MeV/c^2 $<$ $M_{\gamma s}$ $<$ 600 MeV/c^2

C4. 200 MeV/c $<$ $|\vec{p}_{\gamma s}|$ $<$ 400 MeV/c

Criteria C1, C3, and C4 search for the K_S with momentum in the proper range. Invariant mass was calculated as in equation 9.1. Criterion C2 reflects the fact that these events have no decay electrons. Plots of $|\vec{p}_{\gamma s}|$ vs. $M_{\gamma s}$ for $n \to \bar{\nu} K^0$; $K_S \to \pi^0 \pi^0$ and atmospheric neutrino Monte Carlo are shown in figure 9.10. The signal region

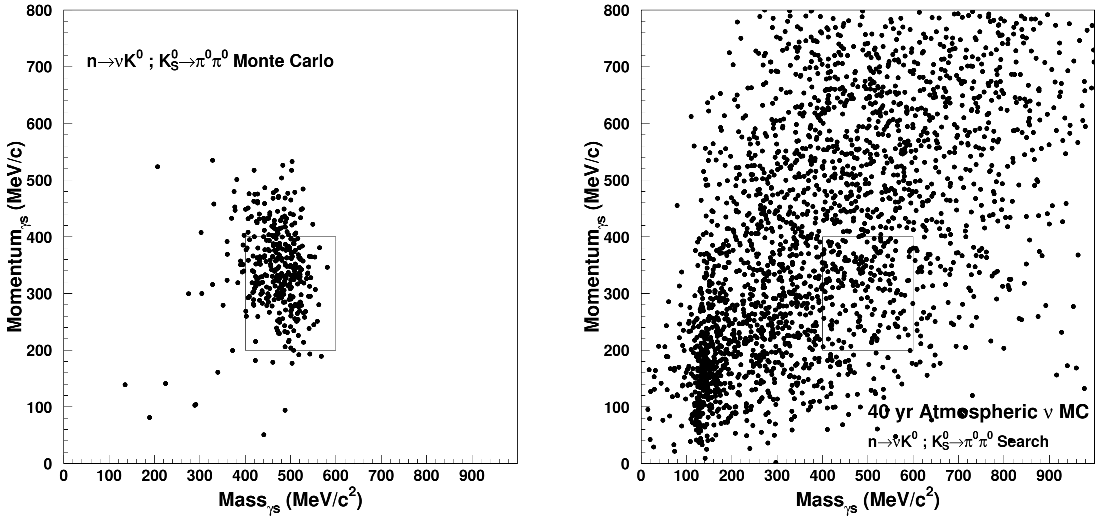

Figure 9.10: $|\vec{p}_{\gamma s}|$ vs. $M_{\gamma s}$ for events passing criteria C1-C2 for $n \to \bar{\nu} K^0$; $K_S \to \pi^0\pi^0$ Monte Carlo and 40-year atmospheric neutrino Monte Carlo.

has a significant expected background of 14 events. To reduce this background, the invariant mass of combinatoric pairs of rings were reconstructed. For an event to be accepted, it must have at least one of the pairs reconstruct to the π^0 mass (85 MeV/c^2 $< m_{\gamma\gamma} <$ 185 MeV/c^2). This π^0 constraint will be labeled criterion C5. Revised plots of $|\vec{p}_{\gamma s}|$ vs. $M_{\gamma s}$ for $n \to \bar{\nu} K^0$; $K_S \to \pi^0\pi^0$ and atmospheric neutrino Monte Carlo samples are shown in figure 9.11.

By passing the two Monte Carlo samples through the selection criteria, the detection efficiency and background for $n \to \bar{\nu} K^0$; $K_S \to \pi^0\pi^0$ were estimated to be 6.1% and 11, respectively. The detection efficiency includes the $K_S \to \pi^0\pi^0$ branching ratio of 31.4% and the probability of 1/2 for the K^0 to be in the K_S state. From now on, all detection efficiencies quoted will include all branching ratios. A breakdown of the background inducing neutrino interactions is outlined in table 9.4. By imposing the π^0 constraint the background decreased by 21% from 14 to 11 events while the detection efficiency decreased by only 6% from 6.5% to 6.1%. Passing the data through

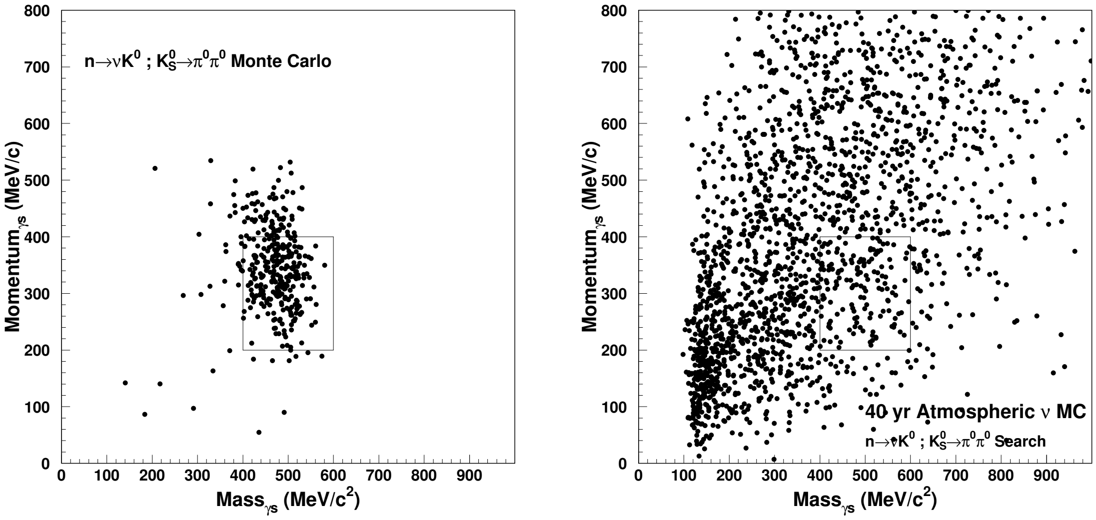

Figure 9.11: $|\vec{p}_{\gamma s}|$ vs. $M_{\gamma s}$ for events passing criteria C1-C2 for $n \rightarrow \bar{\nu}K^0$; $K_S \rightarrow \pi^0\pi^0$ Monte Carlo and 40-year atmospheric neutrino Monte Carlo. These events also satisfy the requirement that at least one pair of e-like rings reconstructed to the π^0 mass.

the selection criteria yielded 5 events (figure 9.12), consistent with the background expected from atmospheric neutrinos. The final limit of $n \rightarrow \bar{\nu}K^0$; $K_S \rightarrow \pi^0\pi^0$ was calculated using the method outlined in appendix A and was found to be 2.8×10^{32} years at the 90% C.L.

9.2.2 $K_S \rightarrow \pi^+\pi^-$

The characteristic for $n \rightarrow \bar{\nu}K^0$; $K_S \rightarrow \pi^+\pi^-$ is its two low energy collapsed Cherenkov rings from the two pions. A sample event is shown in figure 9.13. The selection are straight-forward:

D1. two μ-like rings

D2. one decay electron

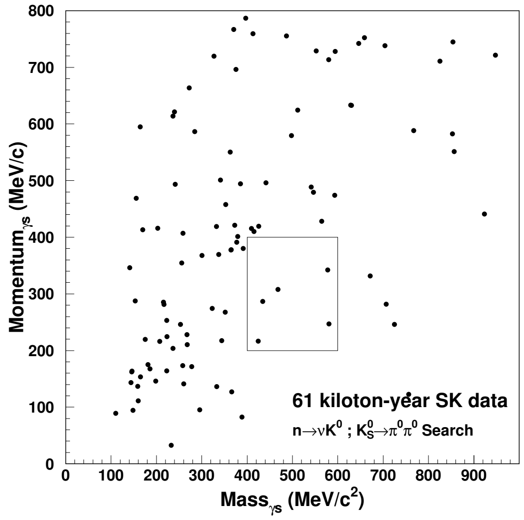

Figure 9.12: $|\vec{p}_{\gamma s}|$ vs. $M_{\gamma s}$ for events passing criteria C1-C2 and the π^0 mass requirement for the 61-kton·year Super–Kamiokande data sample. The number of events passing the selection criteria is consistent with the expected background.

Background for $n \to \bar{\nu} K^0$; $K_S \to \pi^0\pi^0$					
interaction		$\nu_e + \bar{\nu}_e$		$\nu_\mu + \bar{\nu}_\mu$	
		N_{norm}	%	N_{norm}	%
CC	quasi-elastic	1.2	0.7%	-	-
	single-π	48.0	28.6%	2.2	1.3%
	multiple-π	26.9	16.0%	7.4	4.4%
	K prod.	-	-	-	-
	η prod.	1.2	0.7%	1.5	0.9%
NC	quasi-elastic	-	-	-	-
	single-π	4.7	2.8%	5.8	3.5%
	multiple-π	16.4	9.8%	36.3	21.6%
	K prod.	1.2	0.7%	-	-
	η prod.	2.3	1.4%	12.9	7.7%
TOTALS		101.8	60.6%	66.1	39.4%

Table 9.4: Breakdown of background contributions to the decay $n \to \bar{\nu} K^0$; $K_S \to \pi^0\pi^0$ (see table 9.1 for an explanation of N_{norm} and %.)

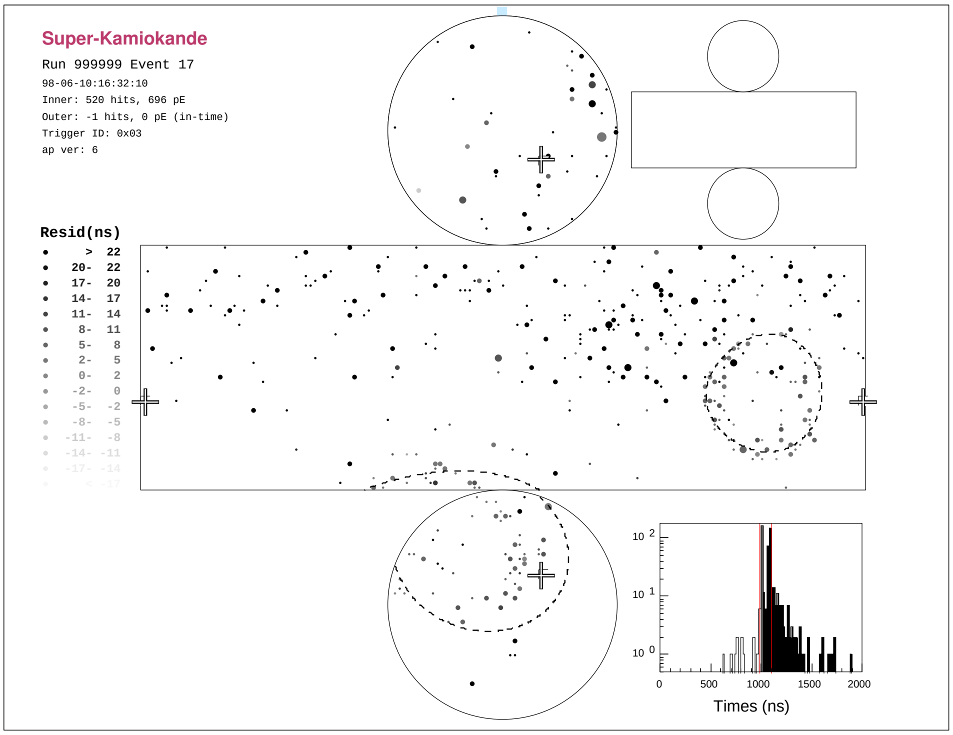

Figure 9.13: $n \to \bar{\nu} K^0$; $K_S \to \pi^+\pi^-$ Monte Carlo event.

D3. 450 MeV/c^2 $< M_{\pi\pi} <$ 550 MeV/c^2

D4. 200 MeV/c $< |\vec{p}_{\pi\pi}| <$ 400 MeV/c

The invariant mass ($M_{\pi\pi}$) and momentum ($|\vec{p}_{\pi\pi}|$) were calculated with the assumption that the two μ-like rings were from a π^+ and π^-. This is because pions and muons with the same momentum have different Cherenkov light yields. The momentum calculation of the two cases (μ or π) will therefore be different. Plots of $|\vec{p}_{\pi\pi}|$ vs. $M_{\pi\pi}$ for $n \to \bar{\nu} K^0$; $K_S \to \pi^+\pi^-$ and atmospheric neutrino Monte Carlo are shown in figure 9.14. Based on these samples, the detection efficiency and background were estimated to be 2.0% and 2.0 events, respectively. The breakdown of the types of interactions which caused the background is outlined in table 9.5. Passing the data through D1-D4 yielded 4 events, slightly higher than the expected background but within statistical error (figure 9.15). The limit set for $n \to \bar{\nu} K^0$ using the decay $K_S \to \pi^+\pi^-$ was $0.5{\times}10^{32}$ years at the 90% C.L.

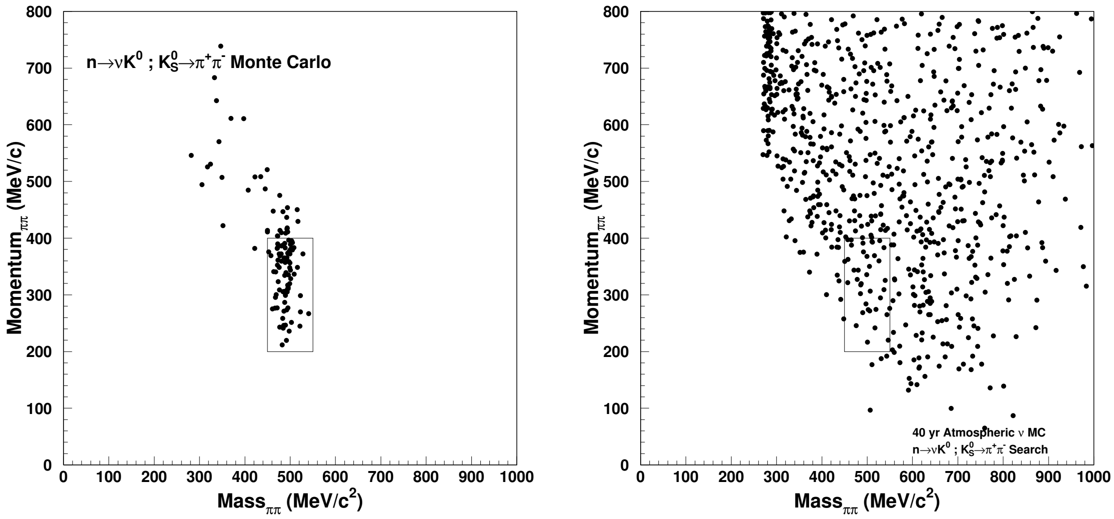

Figure 9.14: $|\vec{p}_{\pi\pi}|$ vs. $M_{\pi\pi}$ for events passing criteria D1-CD for $n \to \bar{\nu} K^0$; $K_S \to \pi^+\pi^-$ Monte Carlo and 40-year atmospheric neutrino Monte Carlo.

9.2.3 Final Limit of $n \to \bar{\nu} K^0$

A summary of the two methods used to search for $n \to \bar{\nu} K^0$ is shown in table 9.6. Unfortunately this decay mode has a high expected background and therefore the sensitivity to detect it is less than that of other modes. This is unfortunate since it is one of the more favored modes of SUSY GUTs. The two methods were combined and a final limit for $n \to \bar{\nu} K^0$ was calculated to be $2.5{\times}10^{32}$ years at the 90% C.L. This can be compared to previous limits of 0.27×10^{32} years set by IMB [12] and 0.86×10^{32} years set by Kamiokande [58].

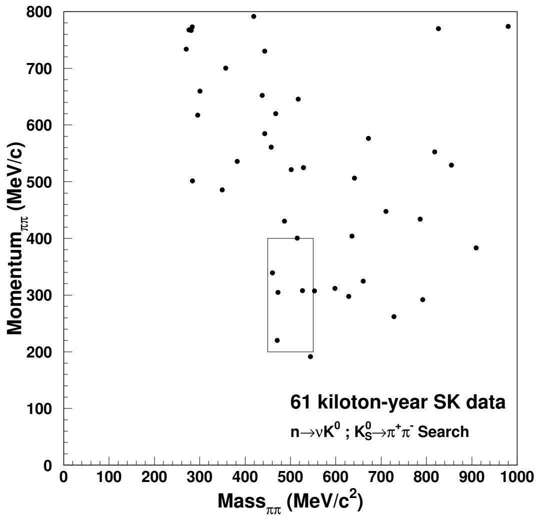

Figure 9.15: $|\vec{p}_{\pi\pi}|$ vs. $M_{\pi\pi}$ for events passing criteria D1-D2 the 61-kton·year Super–Kamiokande data sample. Like the search for $n \to \bar{\nu}K^0$; $K_S \to \pi^0\pi^0$, the number of events passing the selection criteria is consistent with the expected background.

Background for $n \to \bar{\nu}K^0$; $K_S \to \pi^+\pi^-$					
interaction		$\nu_e + \bar{\nu}_e$		$\nu_\mu + \bar{\nu}_\mu$	
		N_{norm}	%	N_{norm}	%
CC	quasi-elastic	-	-	1.5	5.1%
	single-π	-	-	21.5	73.1%
	multiple-π	-	-	2.2	7.5%
	K prod.	-	-	0.7	2.4%
	η prod.	-	-	-	-
NC	quasi-elastic	-	-	-	-
	single-π	-	-	1.2	4.1%
	multiple-π	-	-	-	-
	K prod.	-	-	2.3	7.8%
	η prod.	-	-	-	-
TOTALS		0	0%	29.4	100%

Table 9.5: Breakdown of background contributions to the decay $n \to \bar{\nu}K^0$; $K_S \to \pi^+\pi^-$.

Method	efficiency	N_{BG}^{exp}	N_{obs}	s_{90}	τ/B (90% CL)
$K_S \to \pi^0\pi^0$	6.1%	11	5	3.5	2.8×10^{32} years
$K_S \to \pi^+\pi^-$	2.0%	2.0	4	6.1	0.5×10^{32} years
combined	8.1%	-	-	5.4	2.5×10^{32} years

Table 9.6: Summary of two methods used to search for $n \to \bar{\nu}K^0$ (see table 9.1 for an explanation of N_{norm} and %.)

9.3 $p \to \mu^+ K^0$

Unlike the modes $p \to \bar{\nu}K^+$ and $n \to \bar{\nu}K^0$ where one of the decay products is an invisible neutrino, the mode $p \to \mu^+K^0$ is completely visible. The only exception is when the K_S decays asymmetrically in the decay $K_S \to \pi^+\pi^-$ and one of the pions is below Cherenkov threshold. Being able to reconstruct all particles provides many kinematic handles to separate signal from background.

9.3.1 $K_S \to \pi^0\pi^0$

A $p \to \mu^+K^0$; $K_S \to \pi^0\pi^0$ event would ideally reconstruct to four e-like rings, one μ-like ring, and one decay electron. This is hardly ever the case, so cuts were chosen based on a Monte Carlo simulation of $p \to \mu^+K^0$; $K_S \to \pi^0\pi^0$ events. A sample event is shown in figure 9.16. The initial selection criteria were chosen to be:

E1. one μ-like ring

E2. two to four e-like rings

E3. zero or one decay electron

In addition to selection criteria E1-E3, $p \to \mu^+K^0$; $K_S \to \pi^0\pi^0$ events have a very distinctive kinematic signature. All particles (μ and γs) are completely visible, making it possible to completely reconstruct these events. Based on the

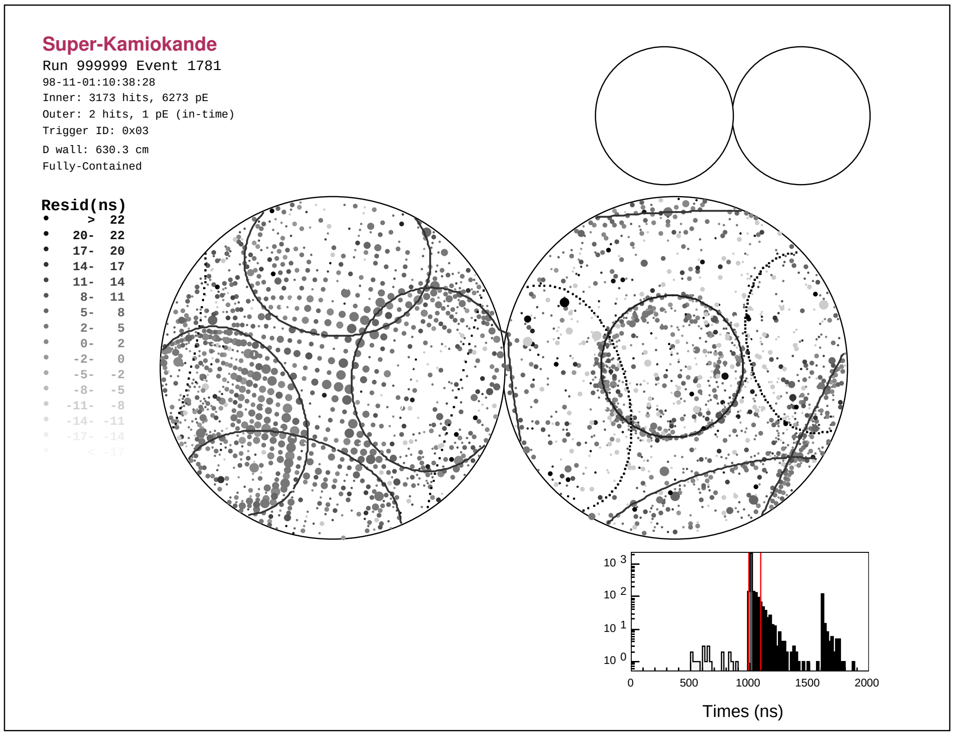

Figure 9.16: $p \to \mu^+ K^0$; $K_S \to \pi^0 \pi^0$ Monte Carlo in front-back view. The four EM showers from the γs from the decays of the π^0s (left hemisphere) are balanced by the μ track (right hemisphere). Note the spike in the timing histogram at about 1600 ns from the decay electron of the μ.

$p \to \mu^+ K^0$;$K_S \to \pi^0 \pi^0$ and 40-year atmospheric neutrino background Monte Carlo samples, addition selection criteria were decided upon:

E4. 750 MeV/c^2 $< M_{tot} <$ 1000 MeV/c^2

E5. $|\vec{p}_{tot}| <$ 300 MeV/c

E6. 400 MeV/c^2 $< M_{\gamma s} <$ 600 MeV/c^2

E7. 150 MeV/c $< |\vec{p}_\mu| <$ 400 MeV/c

Criterion E4 requires that the visible tracks reconstruct the 938-MeV/c^2 mass of the proton. Criterion E5 is a momentum cutoff due to the Fermi momentum in

O^{16} (figure 6.1). Criterion E6 calculates the invariant mass of all e-like rings using equation 9.1. For proton decay events via $p \to \mu^+ K^0$, this should reconstruct to the mass of the K^0. Criterion E7 searches for the momentum of the muon. Because of the kinematic power to reject much of the background, all selection criteria were chosen based only on the $p \to \mu^+ K^0$;$K_S \to \pi^0\pi^0$ Monte Carlo sample. Distributions of total momentum ($|\vec{p}_{tot}|$) vs. total invariant mass (M_{tot}) for $p \to \mu^+ K^0$;$K_S \to \pi^0\pi^0$ and 40-year atmospheric neutrino Monte Carlo for events passing selection criteria C1-C3 are shown in figure 9.17. Distributions of $|\vec{p}_\mu|$ vs. $M_{\gamma s}$ for events passing selection criteria C1-C5 for the two Monte Carlo samples are shown in figure 9.18.

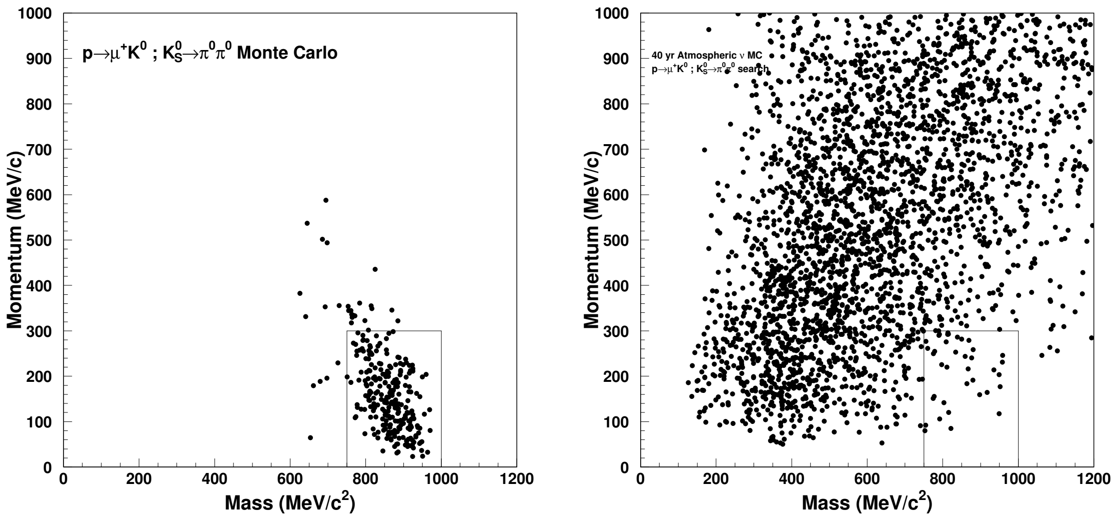

Figure 9.17: Momentum vs. mass for events passing criteria E1-E3 for $p \to \mu^+ K^0$; $K_S \to \pi^0\pi^0$ Monte Carlo and 40-year atmospheric neutrino Monte Carlo.

By applying selection criteria E1-E7 to the $p \to \mu^+ K^0$; $K_S \to \pi^0\pi^0$ and atmospheric neutrino Monte Carlo samples the detection efficiency and background were estimated to be 6.1% and 1 event, respectively. The breakdown of the types of neutrino interactions which caused the background is in table 9.7. Applying the selection criteria to the 61-kton·year data sample yielded no events (figure 9.19) therefore a

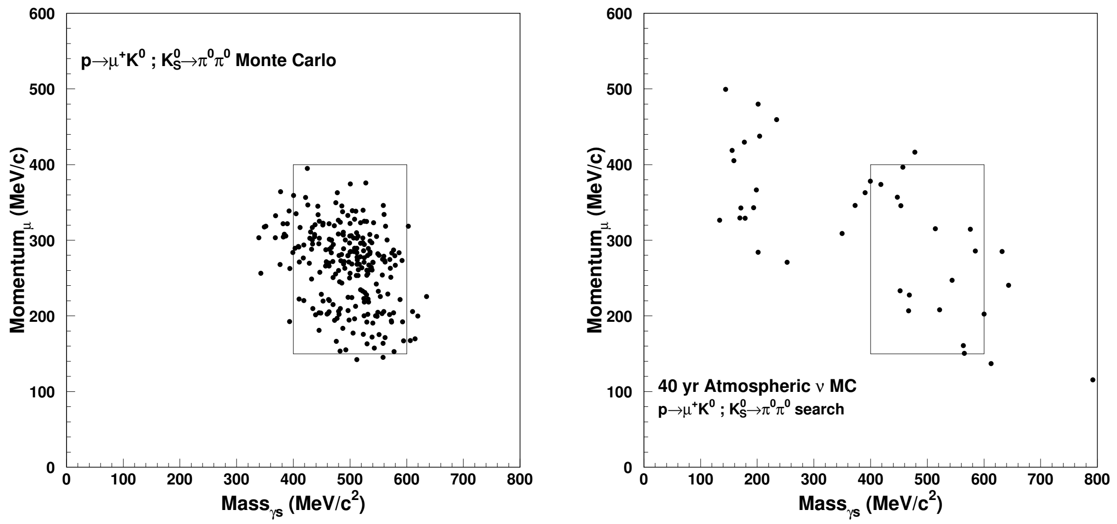

Figure 9.18: μ momentum vs. e-like mass for events passing selection criteria E1-E5 for $p \to \mu^+K^0$; $K_S \to \pi^0\pi^0$ Monte Carlo and 40-year atmospheric neutrino Monte Carlo.

lower limit on the partial lifetime of the proton into $p \to \mu^+K^0$ was set to be 5.4×10^{32} years at the 90% C.L.

9.3.2 $K_S \to \pi^+\pi^-$

In $p \to \mu^+K^0$; $K_S \to \pi^+\pi^-$ events either both pions are above Cherenkov threshold or the K_S decays asymmetrically and one pion is below Cherenkov threshold. The former case provides a clean signature of 3 lower energy Cherenkov rings (figure 9.20) from which kinematic variables of the event can be reconstructed. The selection criteria for this case were chosen to be:

F1. three rings

F2. one or two decay electrons

F3. 750 MeV/$c^2 < M_{tot} <$ 1000 MeV/c^2

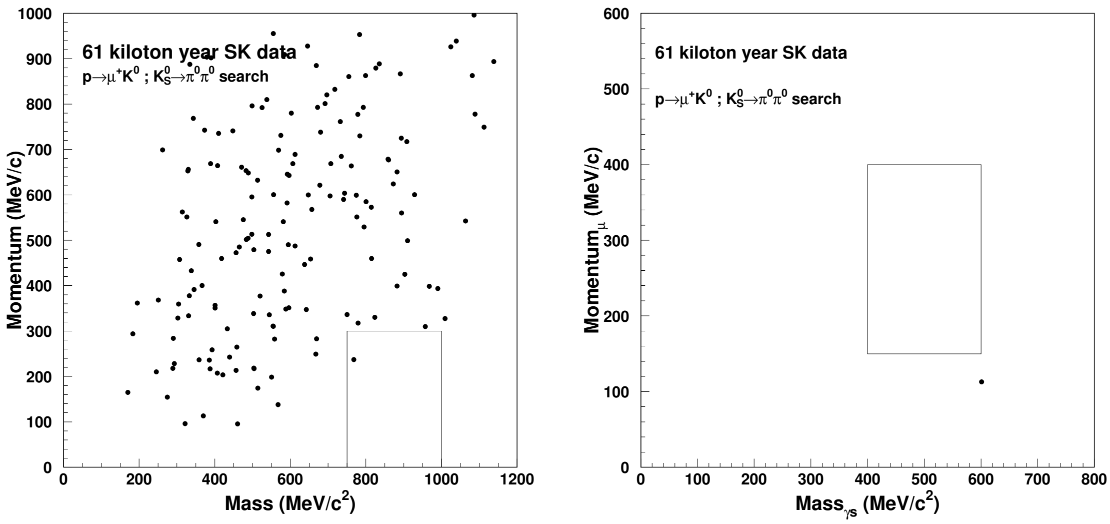

Figure 9.19: Total momentum vs. total mass and μ momentum vs. e-like mass for the 61-kton·year data sample in searching for $p \rightarrow \mu^+ K^0$; $K_S \rightarrow \pi^0\pi^0$. The events in the left figure have passed criteria E1-E3 and the events in the right figure have passed E4-E5.

F4. $|\vec{p}_{tot}| < 300$ MeV/c

F5. 450 MeV/c^2 $< M_{\pi\pi} <$ 550 MeV/c^2

Criterion F1 requires no particle type because approximately 37% of the $p \rightarrow \mu^+ K^0$;$K_S \rightarrow \pi^+\pi^-$ events classified as having three rings identified all three as e-like. Since the efficiency to detect three rings was only 20%, any additional particle type requirement would significantly reduce an already small efficiency. Furthermore, the kinematics of these events provides a powerful background rejection. The remaining selection criteria are straight-forward. Once again, criteria F3 and F4 search for the proton mass and the cut-off from Fermi momentum. Criterion F5 searches for the kaon mass. In order to calculate these kinematic quantities, the track corresponding to the muon must be chosen since momentum and energy determination depends upon whether the particle is a muon, pion, or a light showering particle. The muon was chosen as

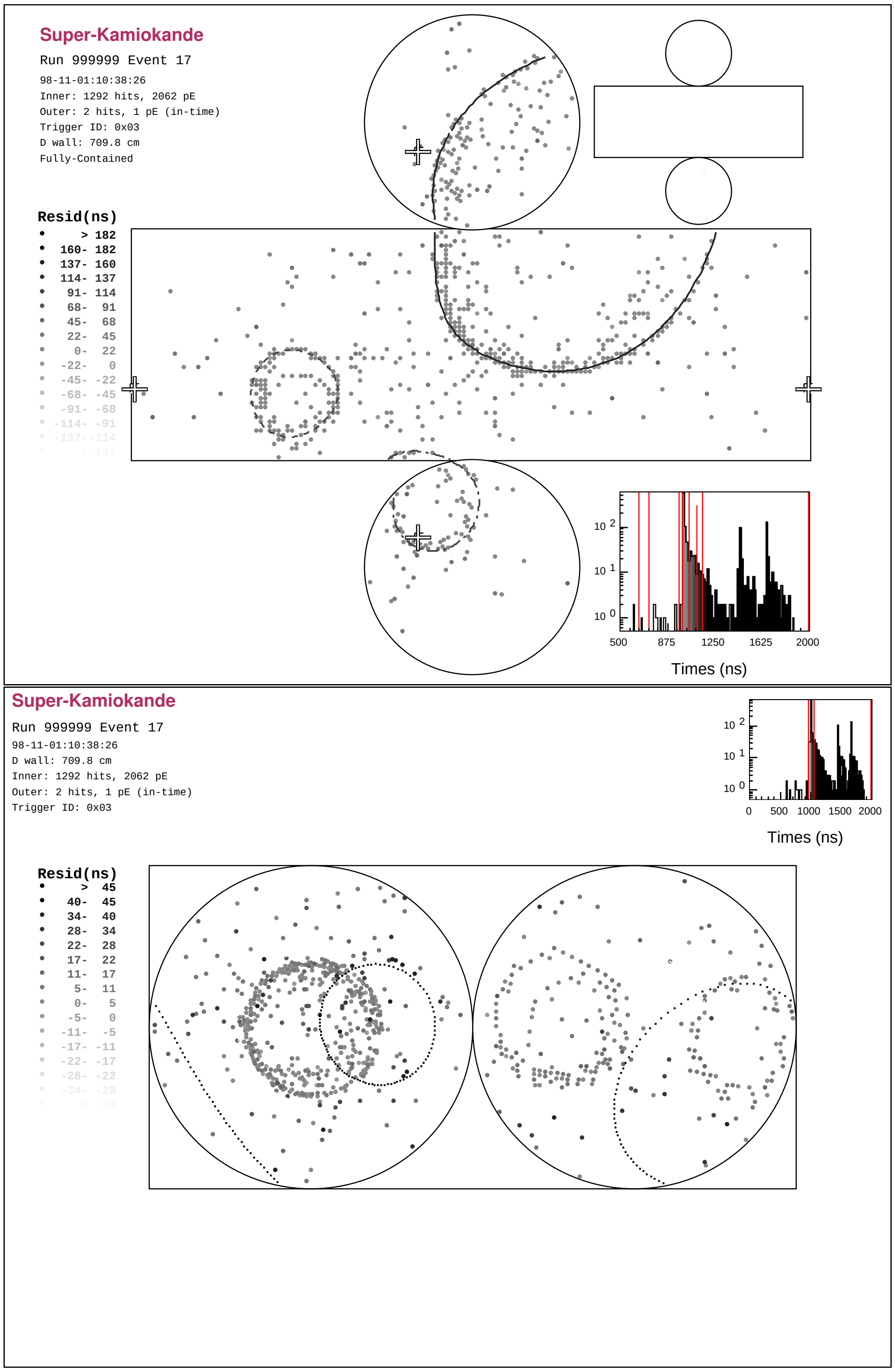

Figure 9.20: $p \to \mu^+ K^0\,; K_S \to \pi^+\pi^-$ Monte Carlo event in unrolled view and front-back view. The two collapsed Cherenkov rings from the two pions from the decay of the K_S balance the track from the muon. Note the two spikes in the timing histogram at about 1500 ns and 1700 ns from the two decay electrons.

Background for $p \to \mu^+ K^0$; $K_S \to \pi^0\pi^0$					
interaction		$\nu_e + \bar{\nu}_e$		$\nu_\mu + \bar{\nu}_\mu$	
		N_{norm}	%	N_{norm}	%
CC	quasi-elastic	-	-	-	-
	single-π	2.3	16.2%	0.7	5.2%
	multiple-π	2.3	16.2%	3.0	21.1%
	K prod.	-	-	-	-
	η prod.	-	-	-	-
NC	quasi-elastic	-	-	-	-
	single-π	-	-	1.2	8.4%
	multiple-π	-	-	4.7	33.1%
	K prod.	-	-	-	-
	η prod.	-	-	-	-
TOTALS		4.6	32%	9.6	68%

Table 9.7: Breakdown of background contributions to the decay $p \to \mu^+ K^0$; $K_S \to \pi^0\pi^0$ (see table 9.1 for an explanation of N_{norm} and %.)

the most energetic track and by checking the "truth" information of the Monte Carlo was determined to be correctly chosen with an efficiency of approximately 90%. The momentum for this track was calculated by assuming it was a muon. The momentum for the other two tracks were calculated by assuming they were pions. Figure 9.21 shows the distributions of $|\vec{p}_{tot}|$ vs. M_{tot} for signal and background Monte Carlo samples. The invariant mass of the two pions was calculated for events passing selection criteria F1-F4. This distribution for the two Monte Carlo samples is shown in figure 9.22.

Based on the two Monte Carlo samples the detection efficiency and background were estimated to be 2.8% and 0.2 events, respectively. The low efficiency can be attributed to asymmetric decay of the K_S where one pion is below Cherenkov threshold and the inefficiency of the ring-counting algorithm at low energies. The two background events which passed were muon induced multiple pion production in the invariant mass range of 1.4 GeV $< W <$ 2.0 GeV. Applying selection criteria F1-F5

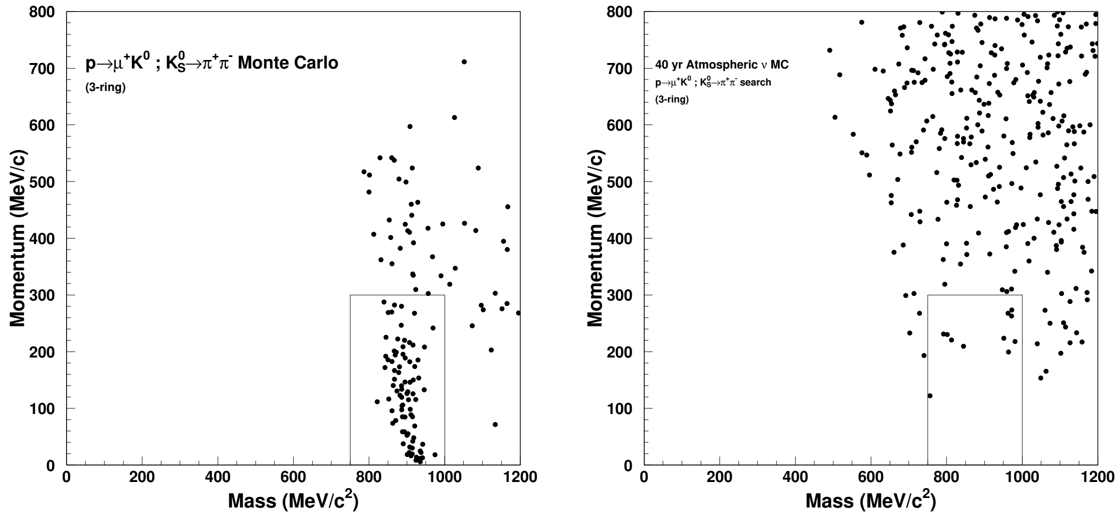

Figure 9.21: $|\vec{p}_{tot}|$ vs. M_{tot} for events passing criteria F1-F2 for $p \to \mu^+ K^0; K_S \to \pi^+\pi^-$ Monte Carlo and 40-year atmospheric neutrino Monte Carlo.

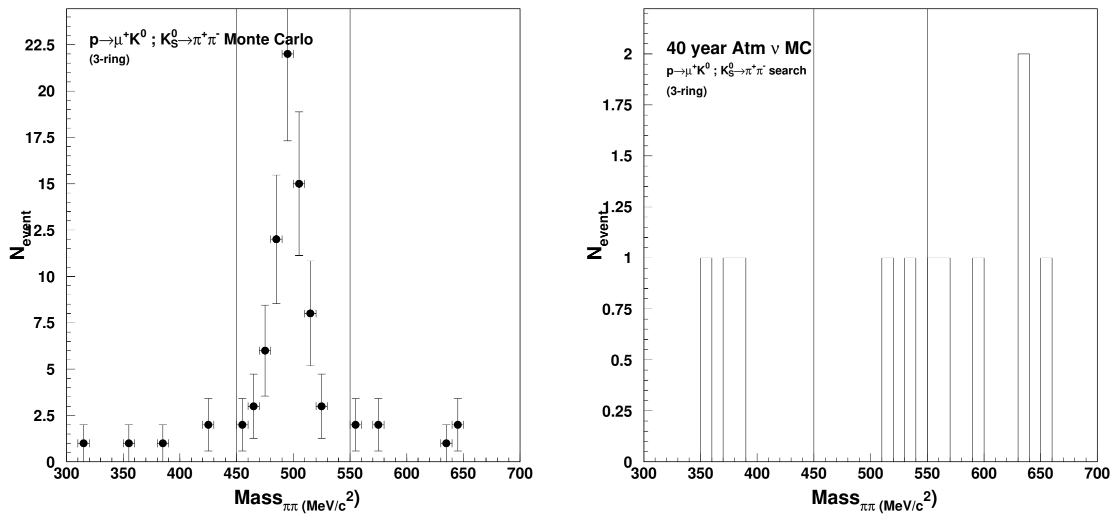

Figure 9.22: Invariant mass of the two pions for events passing selection criteria F1-F4 for $p \to \mu^+ K^0;\, K_S \to \pi^+\pi^-$ Monte Carlo and 40-year atmospheric neutrino Monte Carlo.

to the 61-kton·year data sample yielded no events (figure 9.23) therefore a lower limit on the lifetime of $p \to \mu^+ K^0$ was set to be 2.5×10^{32} years at the 90% C.L.

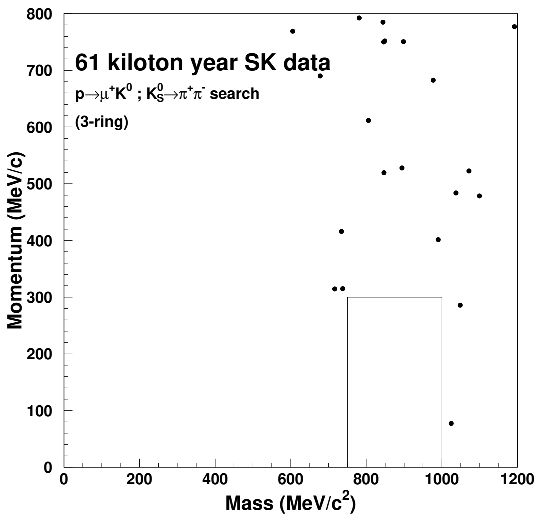

Figure 9.23: $|\vec{p}_{tot}|$ vs. M_{tot} for events passing selection criteria F1-F2 for the 61-kton·year data sample.

$p \to \mu^+ K^0$; $K_S \to \pi^+\pi^-$ events with asymmetric K_S decays do not have the kinematic power of those events where all three tracks were reconstructed. However some kinematic variables can be reconstructed. The momentum of the muon and the total momentum of the event can be used as constraints. Once again, the muon track was chosen to be the most energetic track. The following selection criteria were used to search for these types of events

G1. two μ-like rings

G2. two decay electrons

G3. $|\vec{p}_{tot}| < 300$ MeV/c

G4. 250 MeV/c $< |\vec{p}_\mu| <$ 400 MeV/c

The distribution of $|\vec{p}_{tot}|$ vs. $|\vec{p}_\mu|$ is shown in figure 9.24. The detection efficiency and background were estimated to be 5.3% and 1.3, respectively. The main contribution to the background was charged current single pion production. A breakdown of the interactions contributing to the background is in table 9.8. Applying the selection criteria G1-G4 to the data yielded no events (figure 9.25). The lower limit on the partial lifetime into $p \to \mu^+ K^0$ was then set to be 4.7×10^{32} years (90% C.L.).

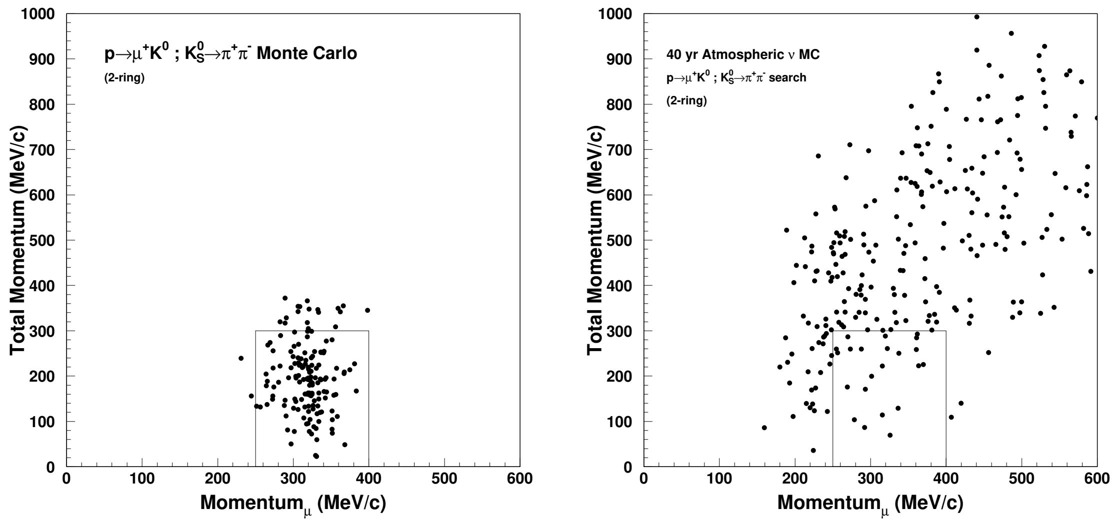

Figure 9.24: Distribution of $|\vec{p}_{tot}|$ vs. $|\vec{p}_\mu|$ for events passing selection criteria G1-G2 for $p \to \mu^+ K^0$; $K_S \to \pi^+\pi^-$ Monte Carlo and 40-year atmospheric neutrino Monte Carlo.

9.3.3 Final Limit of $p \to \mu^+ K^0$

Table 9.9 summarizes the search for $p \to \mu^+ K^0$ using the three methods. Once again, no evidence for $p \to \mu^+ K^0$ was found, therefore the three limits were combined. The combined lower limit of the partial lifetime using the three methods was 1.2×10^{33} years at the 90% C.L. This can be compared to previous limits of 1.3×10^{32} years set by IMB [12] and 1.2×10^{32} years set by Kamiokande [58].

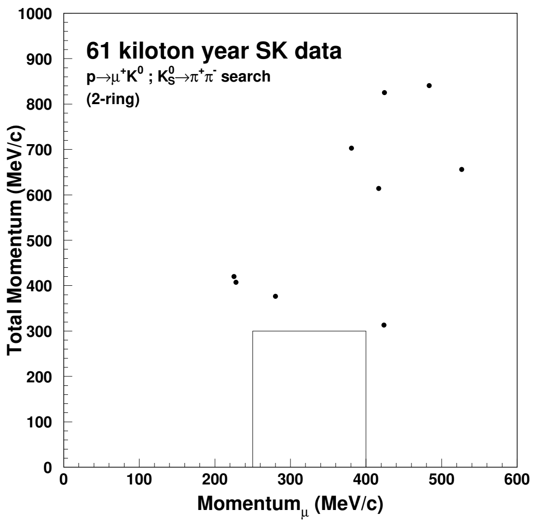

Figure 9.25: Distribution of $|\vec{p}_{tot}|$ vs. $|\vec{p}_\mu|$ for events passing selection criteria G1-G2 for the 61-kton·year data sample.

9.4 $p \to e^+K^0$

9.4.1 $K_S \to \pi^0\pi^0$

The decay $p \to e^+K^0$; $K_S \to \pi^0\pi^0$ is characterized by five EM showers from the e^+ and the four γs from the decays of the π^0s. These events are completely visible, so total invariant mass and total momentum can be reconstructed. The following selection criteria were chosen:

H1. three to five e-like rings

H2. no decay electrons

H3. 750 MeV/c^2 $<$ M_{tot} $<$ 1000 MeV/c^2

H4. $|\vec{p}_{tot}|$ $<$ 300 MeV/c

Background for $p \to \mu^+ K^0$; $K_S \to \pi^+\pi^-$ 2-ring scenario					
interaction		$\nu_e + \bar{\nu}_e$		$\nu_\mu + \bar{\nu}_\mu$	
		N_{norm}	%	N_{norm}	%
CC	quasi-elastic	-	-	0.7	3.8%
	single-π	-	-	15.5	84.2%
	multiple-π	-	-	2.2	12.0%
	K prod.	-	-	-	-
	η prod.	-	-	-	-
NC	quasi-elastic	-	-	-	-
	single-π	-	-	-	-
	multiple-π	-	-	-	-
	K prod.	-	-	-	-
	η prod.	-	-	-	-
TOTALS		0	0%	18.4	100%

Table 9.8: Breakdown of background contributions to the decay $p \to \mu^+ K^0$; $K_S \to \pi^+\pi^-$ in the scenario where only two rings were reconstructed (See table 9.1 for an explanation of N_{norm} and %.)

Method	efficiency	N_{BG}^{exp}	N_{obs}	s_{90}	τ/B (90% CL)
$K_S \to \pi^0\pi^0$	6.1%	1.0	0	2.3	5.4×10^{32} years
$K_S \to \pi^+\pi^-$ (3-ring)	2.8%	0.2	0	2.3	2.5×10^{32} years
$K_S \to \pi^+\pi^-$ (2-ring)	5.3%	1.3	0	2.3	4.7×10^{32} years
combined	14%	-	-	2.3	12×10^{32} years

Table 9.9: Summary of three methods used to search for $p \to \mu^+ K^0$.

The motivation for these selection criteria is the same as those in previous sections. Plots of $|\vec{p}_{tot}|$ vs. M_{tot} for $p \to e^+ K^0$; $K_S \to \pi^0\pi^0$ and atmospheric neutrino Monte Carlo events passing criteria H1-H2 are shown in figure 9.26. Other cuts beyond H1-H4 were studied, but they did not significantly improve the signal to noise ratio.

By applying selection criteria H1-H4 to the $p \to e^+ K^0$; $K_S \to \pi^0\pi^0$ and 40-year atmospheric neutrino Monte Carlo samples the detection efficiency and background were estimated to be 11.8% and 1.2, respectively. The breakdown of the types of neutrino interactions which caused the background is in table 9.10. When the cuts

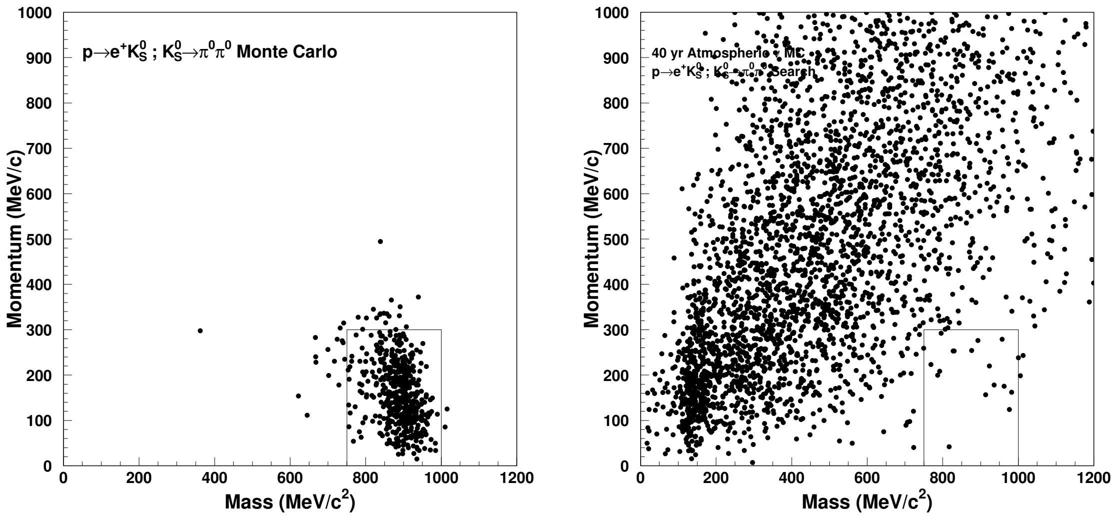

Figure 9.26: Momentum vs. mass for events passing criteria H1-H2 for $p \rightarrow e^+K^0$; $K_S \rightarrow \pi^0\pi^0$ Monte Carlo and 40-year atmospheric neutrino Monte Carlo.

were applied to the 61-kton·year data sample, one event passed (figure 9.27). This is consistent with the expectation from atmospheric neutrino induced background, therefore a lower limit on the lifetime into $p \rightarrow e^+K^0$ of 7.5×10^{32} years at the 90% confidence level was set.

9.4.2 $K_S \rightarrow \pi^+\pi^-$

A sample $p \rightarrow e^+K^0$; $K_S \rightarrow \pi^+\pi^-$ event is shown in figure 9.28. Like the search for $p \rightarrow \mu^+K^0$; $K_S \rightarrow \pi^+\pi^-$, the search for $p \rightarrow e^+K^0$; $K_S \rightarrow \pi^+\pi^-$ was divided into two search methods for the cases where both pions are above Cherenkov threshold and where one pion is below Cherenkov threshold. The selection criteria for events where both pions are above Cherenkov threshold were selected to be:

I1. three rings, at least one of which is e-like

I2. zero or one decay electron

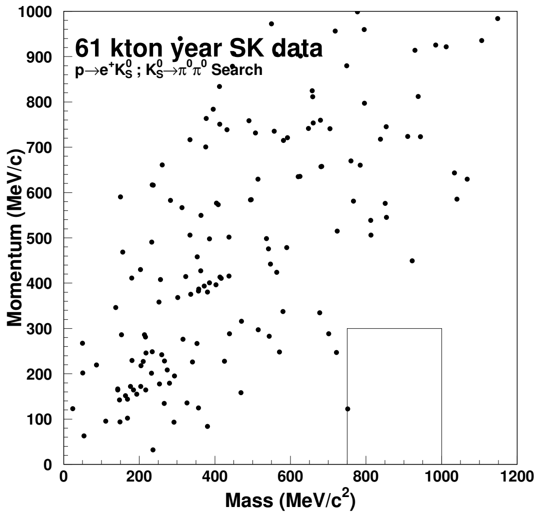

Figure 9.27: Momentum vs. mass for events passing criteria H1-H2 the 61-kton·year Super–Kamiokande data sample.

Background for $p \to e^+K^0$; $K_S \to \pi^0\pi^0$					
interaction		$\nu_e + \bar{\nu}_e$		$\nu_\mu + \bar{\nu}_\mu$	
		N_{norm}	%	N_{norm}	%
CC	quasi-elastic	1.2	6.9%	0.7	4.0%
	single-π	3.5	20.2%	-	-
	multiple-π	4.7	26.9%	0.7	4.0%
	K prod.	-	-	-	-
	η prod.	-	-	0.7	4.0%
NC	quasi-elastic	-	-	-	-
	single-π	-	-	1.2	6.9%
	multiple-π	1.2	6.9%	3.5	20.2%
	K prod.	-	-	-	-
	η prod.	-	-	-	-
TOTALS		10.6	60.9%	6.8	39.1%

Table 9.10: Breakdown of background contributions to the decay $p \to e^+K^0$; $K_S \to \pi^0\pi^0$ (see table 9.1 for an explanation of N_{norm} and %.)

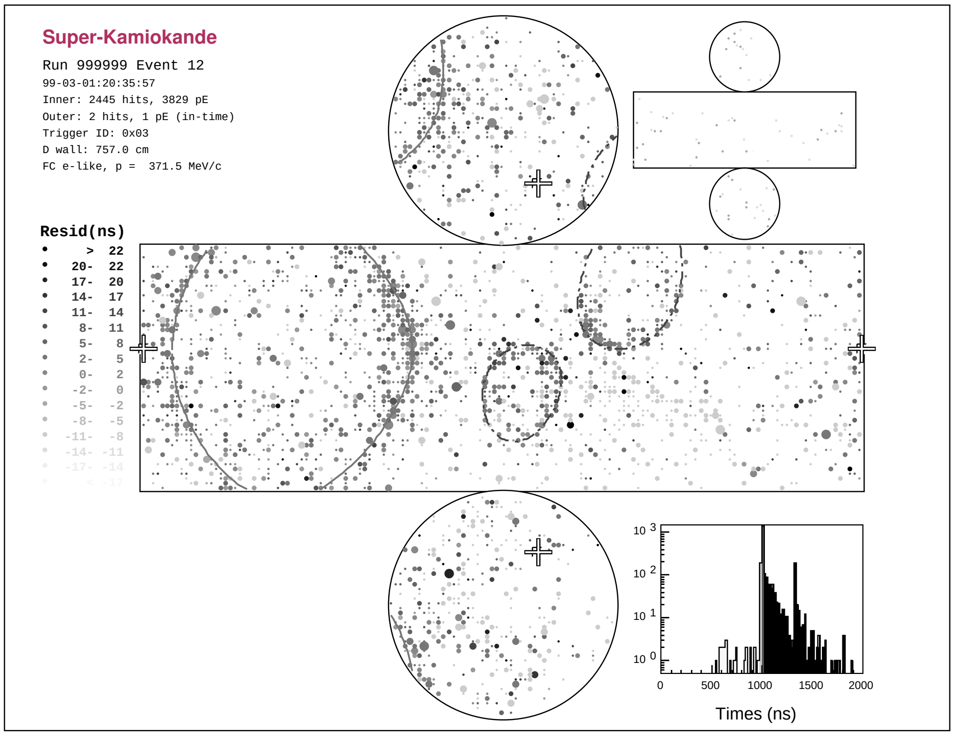

Figure 9.28: $p \to e^+K^0\,;\; K_S \to \pi^+\pi^-$ Monte Carlo event. The two lower energy collapsed Cherenkov rings are from the π^+ and π^- from the K_S decay.

I3. $750\ \mathrm{MeV}/c^2 < M_{tot} < 1000\ \mathrm{MeV}/c^2$

I4. $|\vec{p}_{tot}| < 300\ \mathrm{MeV}/c$

I5. $450\ \mathrm{MeV}/c^2 < M_{\pi\pi} < 550\ \mathrm{MeV}/c^2$

Since multiple e-like rings are allowed, the ring corresponding to the e^+ in $p \to e^+K^0$ must be chosen. This was done by selecting the most energetic ring. The other two rings were taken to be the π^+ and π^-. From this, M_{tot}, $\vec{p}_{tot}$, and $M_{\pi\pi}$ were calculated. The distributions of $|\vec{p}_{tot}|$ vs. M_{tot} for $p \to e^+K^0\,;\; K_S \to \pi^+\pi^-$ and atmospheric neutrino Monte Carlo samples are shown in figure 9.29. The invariant mass of the two pion rings were then reconstructed for events passing selection criteria I1-I4 (figure 9.30).

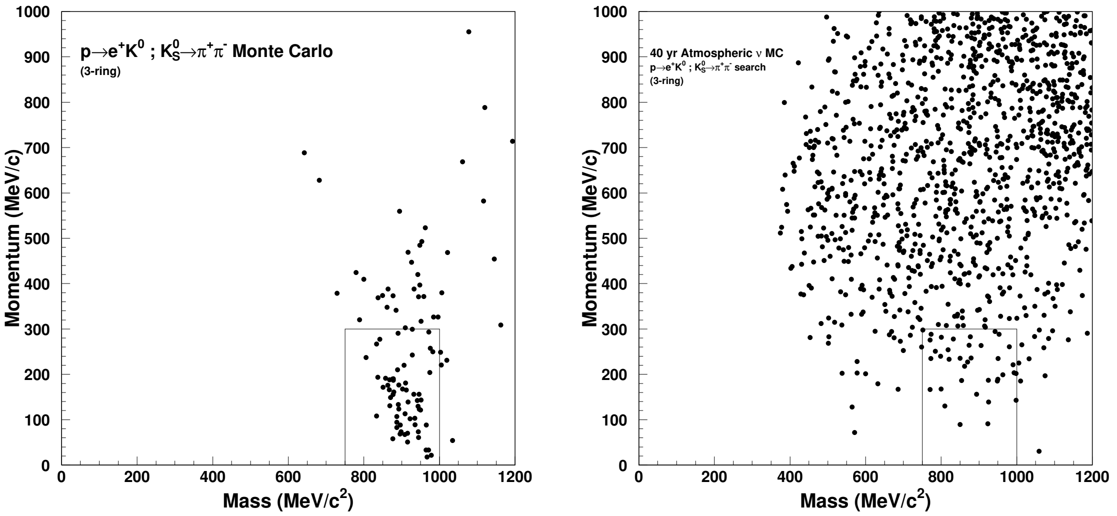

Figure 9.29: Momentum vs. mass for events passing criteria I1-I2 for $p \to e^+K^0$; $K_S \to \pi^+\pi^-$ Monte Carlo and 40-year atmospheric neutrino Monte Carlo.

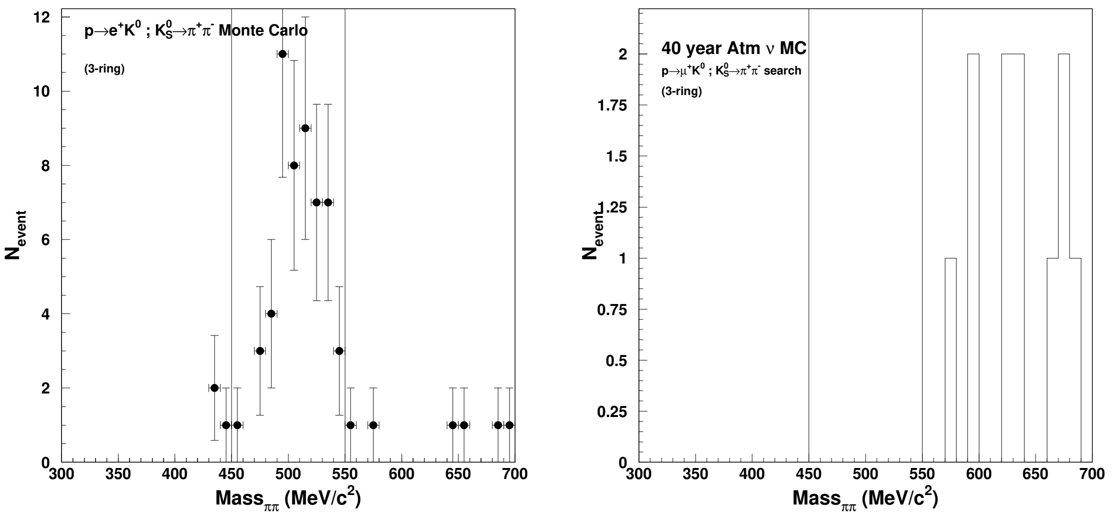

Figure 9.30: Invariant mass of the two pions for events passing selection criteria I1-I4 for $p \to e^+K^0$; $K_S \to \pi^+\pi^-$ Monte Carlo and 40-year atmospheric neutrino Monte Carlo.

Based on the Monte Carlo samples for signal and background, the detection efficiency and background for $p \rightarrow e^+K^0$; $K_S \rightarrow \pi^+\pi^-$ reconstructing three rings were estimated to be 1.4% and < 0.2, respectively. Passing the 61-kton·year data sample through selection criteria I1-I5 yielded no events (figure 9.31). A lower limit on the partial lifetime into $p \rightarrow e^+K^0$ of 1.2×10^{32} years at the 90% confidence level was set.

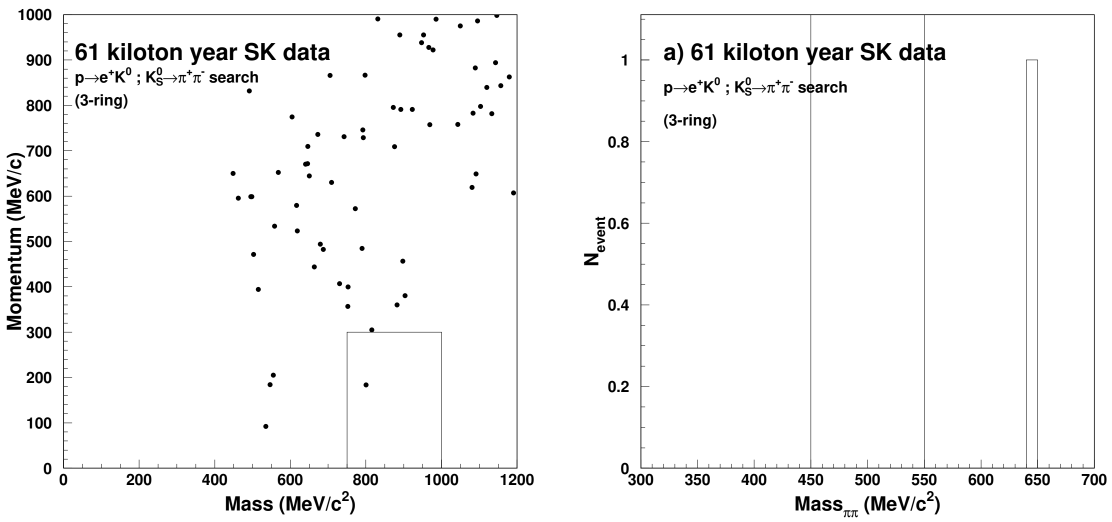

Figure 9.31: a) Total momentum vs. total mass for the 61-kton·year data sample for events passing selection criteria I1-I2. b) $M_{\pi\pi}$ for the data event in the 61-kton·year data sample which passed selection criteria I1-I4.

For those $p \rightarrow e^+K^0$; $K_S \rightarrow \pi^+\pi^-$ events where one pion is either below Cherenkov threshold or not found by the ring-finder, selection criteria were generated based on the two-ring scenario:

J1. one e-like ring

J2. one μ-like ring

J3. one decay electron

J4. 250 MeV/c $<$ $|\vec{p}_e|$ $<$ 400 MeV/c

J5. $|\vec{p}_{tot}|$ $<$ 300 MeV/c

Plots of $|\vec{p}_{tot}|$ vs. $|\vec{p}_e|$ are shown for $p \to e^+K^0$; $K_S \to \pi^+\pi^-$ and 40-year atmospheric neutrino Monte Carlo in figure 9.32. Based on these samples, the detection efficiency and expected background were estimated to be 6.2% and 0.9 events, respectively. The background is summarized in table 9.11. The majority of the events come from charged current single pion production. Applying cuts J1-J5 to the 61-kton·year data sample yielded six events (figure 9.33), significantly above the background. The limit set for $p \to e^+K^0$ was 1.3×10^{32} years at the 90% confidence level.

Some discussion of the excess in the number of signal events is needed. If this were nucleon decay into $p \to e^+K^0$, events would also be expected in the other two methods for the $p \to e^+K^0$ search. The number of events that could be expected in the $K_S \to \pi^0\pi^0$ search is 10 and the number for $K_S \to \pi^+\pi^-$ 3-ring scenario is 1. Observation of no events in the $K_S \to \pi^+\pi^-$ 3-ring scenario is consistent with this hypothesis, but the observation of only one event in the $K_S \to \pi^0\pi^0$ search (consistent with background) is not. Therefore, the anomaly is most likely not due to nucleon decay via $p \to e^+K^0$.

The statistical error of background estimation is only ± 0.2, so is not enough to account for the excess in the data. However, the systematic error is important. All of the background is due to single-π production which has an uncertainty of about 20%. An illustration of this uncertainty is in the expected number of single-π^0 events from neutral current interactions compared with the number from data (see figure 5.16) The data have about 10% more π^0s than the Monte Carlo. Also, the uncertainty of pion-nucleon scattering in the nucleus is estimated to be about 20%. Including these uncertainties, one gets a maximum expected background of 1.5 events. The probability to observe 6 events given an expectation of 1.5 is about 0.35%.

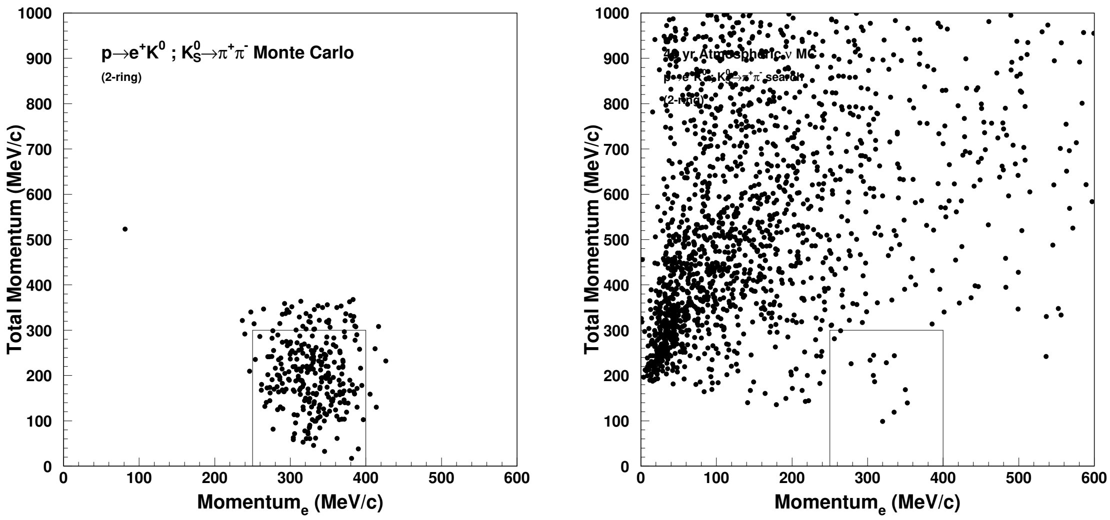

Figure 9.32: Distribution of $|\vec{p}_{tot}|$ vs. $|\vec{p}_e|$ for events passing selection criteria J1-J3 for $p \to e^+K^0$; $K_S \to \pi^+\pi^-$ Monte Carlo and 40-year atmospheric neutrino Monte Carlo.

9.4.3 Final Limit of $p \to e^+K^0$

Table 9.12 summarizes the search for $p \to e^+K^0$. Based on the three search methods described above there was no evidence for proton decay into $p \to e^+K^0$, therefore the limits derived from the three methods were combined yielding a limit of 4.4×10^{32} years at the 90% C.L. This can be compared to previous limits of 0.32×10^{32} years set by IMB [12] and 1.5×10^{32} years set by Kamiokande [58]. The reason that the combined limit is smaller than the limit drawn only from $p \to e^+K^0$;$K_S \to \pi^0\pi^0$ is the relatively large number of events in the data which fell within the signal region for the $p \to e^+K^0$;$K_S \to \pi^+\pi^-$ scenario with two rings.

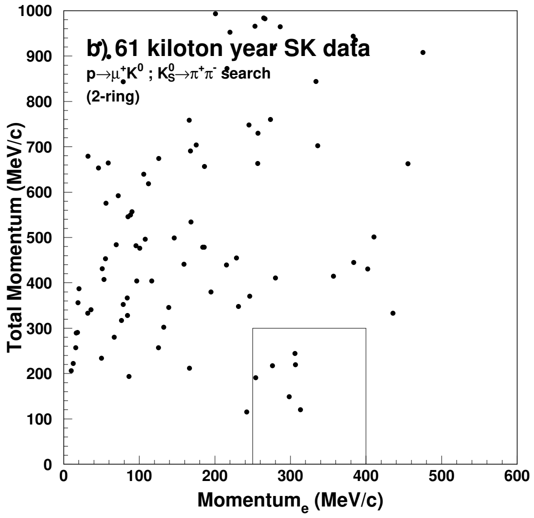

Figure 9.33: Data search for $p \to e^+K^0$; $K_S \to \pi^+\pi^-$ with selection criteria J1-J5. Total momentum vs. total mass for the 61-kton·year data sample.

Background for $p \to e^+K^0$; $K_S \to \pi^+\pi^-$ 2-ring scenario					
interaction		$\nu_e + \bar{\nu}_e$		$\nu_\mu + \bar{\nu}_\mu$	
		N_{norm}	%	N_{norm}	%
CC	quasi-elastic	-	-	-	-
	single-π	7.0	55.6%	4.4	34.8%
	multiple-π	-	-	-	-
	K prod.	-	-	-	-
	η prod.	-	-	-	-
NC	quasi-elastic	-	-	-	-
	single-π	-	-	1.2	9.6%
	multiple-π	-	-	-	-
	K prod.	-	-	-	-
	η prod.	-	-	-	-
TOTALS		7.0	55.6%	5.6	44.4%

Table 9.11: Breakdown of background contributions to the decay $p \to e^+K^0$; $K_S \to \pi^+\pi^-$ for the two-ring scenario (see table 9.1 for an explanation of N_{norm} and %.)

Method	efficiency	N_{BG}^{exp}	N_{obs}	s_{90}	τ/B (90% CL)
$K_S \to \pi^0\pi^0$	12%	1.2	1	3.2	7.5×10^{32} years
$K_S \to \pi^+\pi^-$ (3-ring)	1.4%	< 0.2	0	2.3	1.2×10^{32} years
$K_S \to \pi^+\pi^-$ (2-ring)	6.2%	0.9	6	9.6	1.4×10^{32} years
combined	20%	-	-	9.1	4.4×10^{32} years

Table 9.12: Summary of three methods used to search for $p \to e^+K^0$.

Particle	lifetime τ	$c\tau$	mass	Decay Mode	Branching Ratio
K^+	12.9 ns	3.7 m	493.7 MeV/c^2	$\mu^+\nu_\mu$ $\pi^+\pi^0$	63.5% 21.2%
K_S^0	.089 ns	2.7 cm	497.7 MeV/c^2	$\pi^+\pi^-$ $\pi^0\pi^0$	68.6% 31.4%
K_L^0	52 ns	15.5 m	497.7 MeV/c^2	$\pi^\pm e^\mp\nu_e$ $\pi^\pm\mu^\mp\nu_\mu$ $3\pi^0$ $\pi^+\pi^-\pi^0$	38.8% 27.2% 21.1% 12.6%

Table 9.13: Summary of K mesons. Values taken from the Particle Data Book.

9.5 Summary

This section is a summary of the nucleon decay analyses in this chapter. Table 9.13 is a summary of the properties of the K mesons, table 9.14 summarizes the searches for the various modes, and tables 9.15, 9.16, 9.17,and 9.18 summarize the selection criteria used to search for the various modes.

Mode	Method	efficiency	N_{BG}^{exp}	N_{obs}	s_{90}	τ/B (10^{32} years) (90% CL)
$p \to \bar{\nu} K^+$	$K^+ \to \pi^+\pi^0$	6.8%	1.7	0	2.3	6.0
	$K^+ \to \mu^+\nu_\mu$ prompt γ	9.3%	1.0	0	2.3	8.2
	$K^+ \to \mu^+\nu_\mu$ spectrum fit	33%	137	128	15.6	4.3
	combined	49%	-	-	6.2	17
$n \to \bar{\nu} K^0$	$K_S \to \pi^0\pi^0$	6.1%	11	5	3.5	2.8
	$K_S \to \pi^+\pi^-$	2.0%	2.0	4	6.1	0.5
	combined	8.1%	-	-	5.4	2.5
$p \to \mu^+ K^0$	$K_S \to \pi^0\pi^0$	6.1%	1.0	0	2.3	5.4
	$K_S \to \pi^+\pi^-$ (3-ring)	2.8%	0.2	0	2.3	2.5
	$K_S \to \pi^+\pi^-$ (2-ring)	5.3%	1.3	0	2.3	4.7
	combined	14%	-	-	2.3	12
$p \to e^+ K^0$	$K_S \to \pi^0\pi^0$	12%	1.2	1	3.2	7.5
	$K_S \to \pi^+\pi^-$ (3-ring)	1.4%	< 0.2	0	2.3	1.2
	$K_S \to \pi^+\pi^-$ (2-ring)	6.2%	0.9	6	9.6	1.4
	combined	20%	-	-	9.1	4.4

Table 9.14: Summary of final results for searches for $p \to \bar{\nu} K^+$, $n \to \bar{\nu} K^0$, $p \to \mu^+ K^0$, and $p \to e^+ K^0$.

Method	**Selection Criteria**
$K^+ \to \pi^+\pi^0$	A1) two e-like rings A2) one decay A3) 85 MeV/c^2 $< M_{\gamma\gamma} <$ 185 MeV/c^2 A4) 175 MeV/c $< p_{\gamma\gamma} <$ 250 MeV/c A5) 40 PE $< Q_{back} <$ 100 PE
$K^+ \to \mu^+\nu_\mu$ prompt γ-ray	B1) one μ-like ring B2) one decay B3) 215 MeV/c $< p_\mu <$ 260 MeV/c B4) proton rejection B5) $N_{hit}^{12\,ns} > 7$
$K^+ \to \mu^+\nu_\mu$ spectrum fit	B1) one μ-like ring B2) one decay B3) 215 MeV/c $< p_\mu <$ 260 MeV/c B6) $N_{hit}^{12\,ns} \leq 7$

Table 9.15: Summary of the selection criteria used to search for $p \to \bar{\nu} K^+$.

Method	Selection Criteria
$K_S \to \pi^0\pi^0$	C1) three or four e-like rings C2) no decays C3) 400 MeV/c^2 $<$ $M_{\gamma s}$ $<$ 600 MeV/c^2 C4) 200 MeV/c $<$ $p_{\gamma s}$ $<$ 400 MeV/c C5) π^0 constraint
$K_S \to \pi^+\pi^-$	D1) two μ-like rings D2) one decay D3) 450 MeV/c^2 $<$ $M_{\pi\pi}$ $<$ 550 MeV/c^2 D4) 200 MeV/c $<$ $p_{\pi\pi}$ $<$ 400 MeV/c

Table 9.16: Summary of the selection criteria used to search for $n \to \bar{\nu}K^0$.

Method	Selection Criteria
$K_S \to \pi^0\pi^0$	E1) one μ-like ring E2) two to four e-like rings E3) zero or one decay E4) 750 MeV/c^2 $<$ M_{tot} $<$ 1000 MeV/c^2 E5) p_{tot} $<$ 300 MeV/c E6) 400 MeV/c^2 $<$ $M_{\gamma s}$ $<$ 600 MeV/c^2 E7) 150 MeV/c $<$ p_μ $<$ 400 MeV/c
$K_S \to \pi^+\pi^-$ three-ring	F1) three rings F2) one or two decays F3) 750 MeV/c^2 $<$ M_{tot} $<$ 1000 MeV/c^2 F4) p_{tot} $<$ 300 MeV/c F5) 450 MeV/c^2 $<$ $M_{\pi\pi}$ $<$ 550 MeV/c^2
$K_S \to \pi^+\pi^-$ two-ring	G1) two μ-like rings G2) two decays G3) p_{tot} $<$ 300 MeV/c G4) 250 MeV/c $<$ p_μ $<$ 400 MeV/c

Table 9.17: Summary of the selection criteria used to search for $p \to \mu^+K^0$.

Method	Selection Criteria
$K_S \to \pi^0\pi^0$	H1) three to five e-like rings H2) no decays H3) 750 MeV/c^2 $<$ M_{tot} $<$ 1000 MeV/c^2 H4) p_{tot} $<$ 300 MeV/c
$K_S \to \pi^+\pi^-$ three-ring	I1) three rings, at least one e-like I2) zero or one decay I3) 750 MeV/c^2 $<$ M_{tot} $<$ 1000 MeV/c^2 I4) p_{tot} $<$ 300 MeV/c I5) 450 MeV/c^2 $<$ $M_{\pi\pi}$ $<$ 550 MeV/c^2
$K_S \to \pi^+\pi^-$ two-ring	J1) one e-like ring J2) one μ-like ring J3) one decay J4) 250 MeV/c $<$ p_e $<$ 400 MeV/c J5) p_{tot} $<$ 300 MeV/c

Table 9.18: Summary of the selection criteria used to search for $p \to e^+K^0$.

Chapter 10

Conclusion

10.1 Summary

After a 991-day (61-kton·year) exposure, 7940 contained events were recorded in the fiducial volume of the Super–Kamiokande detector. This data sample was searched for nucleon decay via $p \to \bar{\nu}K^+$, $n \to \bar{\nu}K^0$, $p \to \mu^+K^0$, and $p \to e^+K^0$. No evidence for nucleon decay into any of the modes was found, therefore lower limits on the partial lifetimes into these modes of (17, 2.5, 12, and 4.4) $\times 10^{32}$ at the 90% confidence level were set. These limits exceed limits set by previous detectors significantly. A summary of the results for IMB, Kamiokande, Soudan II, and Super–Kamiokande is shown in table 10.1 and in figure 10.1.

Limit summary (10^{32} years, 90% CL)				
Mode	Super–Kamiokande	IMB[12]	Kamiokande [58]	Soudan II [97, 54]
$p \to \bar{\nu}K^+$	17	1.8	1.0	0.46
$n \to \bar{\nu}K^0$	2.5	0.86	0.27	0.26
$p \to \mu^+K^0$	12	1.3	1.2	1.2
$p \to e^+K^0$	4.4	0.32	1.5	0.85

Table 10.1: Summary of limits studied in this dissertation for Super–Kamiokande, IMB, Kamiokande, and Soudan II.

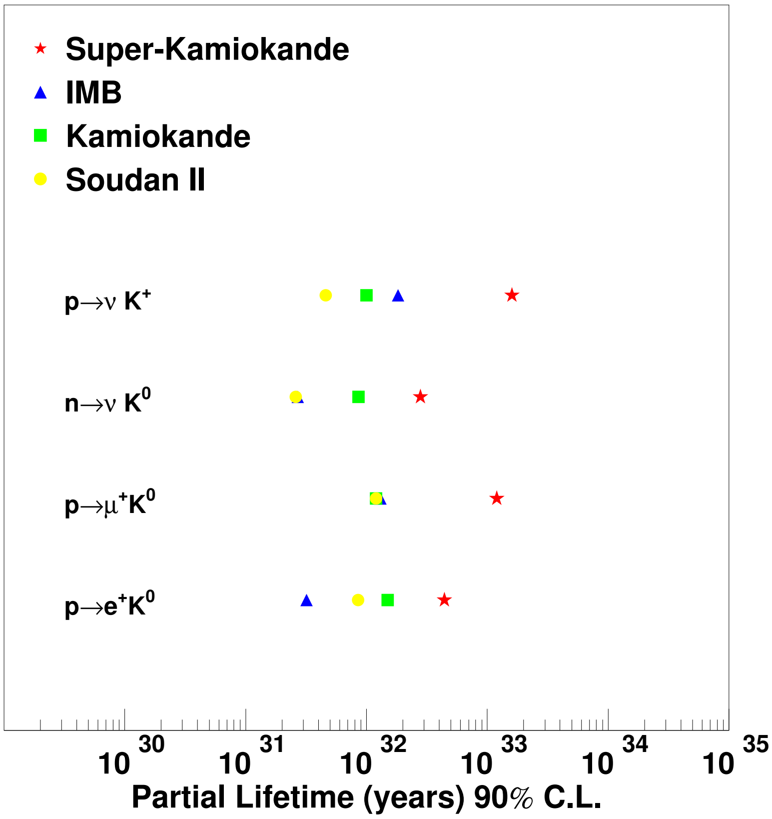

Figure 10.1: Summary of limits set in this dissertation and previous limits.

10.2 Future

Unfortunately, the sensitivity to the nucleon decay modes studied in this dissertation is now limited by the background from atmospheric neutrinos. Therefore an increase in the exposure by a factor of x will result in a sensitivity of only $\sqrt{x}$. For instance, assuming that the detection efficiency does not change and that the number of observed events becomes comparable to the number of estimated background, the limit for $p \to \bar{\nu}K^+$ after an exposure of 610 kton·years (10 times the current exposure of Super–Kamiokande) is estimated to be about 7×10^{33} years (90% C.L.). This impacts the potential "next detector" in that new ways must be found to eliminate the background. Some of this can be done by developing better event reconstruction algorithms or imposing more stringent selection criteria.

However, before thinking of new ways to reject the background, the background must be better understood. As of now, the various contributions to the background estimation are not well understood. Uncertainties in the overall atmospheric neutrino flux, the loss of muon neutrinos in neutrino oscillations, the pion production cross-sections, and the hadronic interactions of pions all contribute to the reasonably large uncertainty in the background estimation [98]. Since the background affects the sensitivity of a detector to specific nucleon decay modes, these contributions to the background estimation must be better understood in order to optimize the potential performance of the next detector.

10.3 Discussion

The result for $p \to \bar{\nu}K^+$ presented in this dissertation essentially excludes the minimal SUSY $SU(5)$ model. However, in the past several years interest has grown in models based on the $SO(10)$ symmetry group. The $SO(10)$ group is desirable since it allows for a right-handed neutrino and puts all fermions into a single multiplet.

The $SO(10)$ model by Lucas and Raby [23] predicts proton lifetimes into $p \to \bar{\nu}K^+$ varying from 1×10^{33} to 2×10^{34} years and bound neutron lifetimes into $n \to \bar{\nu}K^0$ varying from 2×10^{32} to 1×10^{33} years. The results for $p \to \bar{\nu}K^+$ and $n \to \bar{\nu}K^0$ presented in this dissertation are beginning to test these predictions, however more exposure and sensitivity is needed to significantly constrain them.

There has been recent excitement about an $SO(10)$ model incorporating neutrino mass proposed by Babu, Pati, and Wilczek [24] which suggests that the proton lifetime into $p \rightarrow \bar{\nu}K^+$ should be less than 5×10^{33} years [32]. In addition, it predicts that the branching ratio for $p \rightarrow \mu^+K^0$ is comparable to that for $p \rightarrow \bar{\nu}K^+$. Simultaneous observation of these decays would support this theory. No evidence for nucleon decay into either of these modes was found with the analysis presented in this dissertation. Furthermore, the limits set on these modes are comparable to the prediction for the lifetimes. If this model is indeed correct, Super–Kamiokande should begin to see events within the next couple of years. If not, the results will constrain the model significantly.

Appendix A

Setting a Limit

The decay rate Γ of a proton (and subsequently the lifetime τ) is given by the simple formula

$$\Gamma = \frac{n_{obs}}{N_0} \frac{1}{\Delta t \, \epsilon \, B} = \frac{1}{\tau} \quad \text{(A.1)}$$

where n_{obs} is the number of observed proton decays, N_0 is the number of protons at $t = 0$, Δt is the exposure time, ϵ is the detection efficiency, and B is the branching ratio of the proton into a particular mode. The partial lifetime removes the unknown branching ratio and is defined as

$$\frac{\tau}{B} = \frac{N_0 \, \Delta t \, \epsilon \, B}{n_{obs}} \quad \text{(A.2)}$$

The probability to observe n events is governed Poisson statistics

$$P(n, \mu) = \frac{\mu^n}{n!} e^{-\mu} \quad \text{(A.3)}$$

where μ is the mean of the distribution. For cases where background exists the mean μ is $\mu_s + \mu_b$ where μ_s is the mean number of signal events and μ_b is the mean number of background events. When the observed number of events is either zero or consistent with the expected background, an upper limit on the number of events from that particular nucleon decay mode is set. This upper limit $s_{P_{cl}}$ is defined as the value of μ_s for which any repeat of the experiment would yield more than the number observed in the current experiment with a probability P_{cl}. In general, limits are quoted with $P_{cl} = 90\%$, or in other words, at the 90% confidence level. The general formula for calculating s_{90} is

$$0.90 = \frac{\int_0^{s_{90}} P\left(n_{obs}, x\right)\, dx}{\int_0^{\infty} P\left(n_{obs}, x\right)\, dx} \tag{A.4}$$

this is the background unsubtracted limit. To get the background subtracted limit, x is substituted with $x + \mu_b$ where μ_b is the mean expected background. This method of setting limits is the *Poisson processes with background* method outlined in reference [96]. All limits quoted in this dissertation were based on this procedure. The lower limit on the partial lifetime is then given by

$$\frac{\tau}{B} > \frac{N_{p(n)}\, \lambda\, \epsilon\, B_m}{s_{90}} \tag{A.5}$$

where $N_{p(n)}$ is the number of protons (neutrons) per kiloton in water, λ is the detector exposure in kiloton·years, ϵ is the detection efficiency, and B_m is the meson branching ratio.

Finally, when using different methods to set limits on a single nucleon decay modes (i.e. different meson decay modes), the limits are combined to make a final limit for that particular decay mode. The combined s_{90} for n experiments is similar to equation A.4

$$0.90 = \frac{\int_0^{s_{90}} \prod_{i=1}^{n} \left[\, P\left(n_{obs}, n_i(x)\right)\right]\, dx}{\int_0^{\infty} \prod_{i=1}^{n} \left[\, P\left(n_{obs}, n_i(x)\right)\right]\, dx} \tag{A.6}$$

where i denotes the ith method, n_{obs} is the number of observed events, and $n_i(x)$ is given by

$$n_i(x) = \mu_{b,i} + \frac{\epsilon_i B_i \Delta t}{\sum_{i=1}^{n} \epsilon_i B_i \Delta t} x \tag{A.7}$$

Bibliography

[1] Murray Gell-Mann. A schematic model of baryons and mesons. *Physics Letters*, **8**:214, 1964.

[2] M. Breidenbach *et al.* Observed behavior of highly inelastic electron proton scattering. *Physical Review Letters*, **23**:935, 1969.

[3] H. Weyl. *Zeitschrift für Physik*, **56**:330, 1929.

[4] E.C.G. Stückelberg. *Helvetica Physica Acta*, **11**:229, 1939.

[5] E.P. Wigner. *Proceedings of the American Philosophy Society*, **93**:521, 1949.

[6] S.L. Glashow. *Nuclear Physics*, **22**:579, 1961.

[7] A. Salam. *Proceedings Of The Nobel Symposium Held 1968 At Lerum, Sweden*, page 367, 1968.

[8] S. Weinberg. *Physical Review Letters*, **19**:1264, 1967.

[9] N. Cabibbo. *Physical Review Letters*, **10**:531, 1963.

[10] M. Kobayashi and T. Maskawa. *Progress in Theoretical Physics*, **49**:652, 1973.

[11] H. Georgi and S. Glashow. *Physical Review Letters*, **32**:438, 1974.

[12] C. McGrew *et al.* *Physical Review*, **D59**:052004, 1999.

[13] M. Shiozawa *et al.* *Physical Review Letters*, **81**:3319–3323, 1998.

[14] E. Witten. *Nuclear Physics*, **B188**:513, 1981.

[15] S. Dimopoulos and S. Raby. *Nuclear Physics*, **B192**:353, 1981.

[16] J. Ellis, D.V. Nanopoulos, and Serge Rudaz. *Nuclear Physics*, **B202**:43, 1982.

[17] S. Weinberg. *Physical Review*, **D26**:287, 1982.

[18] N. Sakai and T. Yanagida. *Nuclear Physics*, **B197**:83, 1982.

[19] S. Dimopoulos, S. Raby, and F. Wilczek. *Physics Letters*, **112B**:133, 1982.

[20] S. Dimopoulos and H. Georgi. *Nuclear Physics*, **B193**:150, 1981.

[21] N. Sakai. *Zeitschrift für Physik*, **C11**:153, 1981.

[22] J. Hisano, H. Murayama, and T. Yanagida. *Nuclear Physics*, **402B**:46, 1993.

[23] V. Lucas and S. Raby. *Physical Review*, **D55**:6986, 1997.

[24] K.S. Babu J.C. Pati and F. Wilczek. *Nuclear Physics*, **B566**:33, 2000.

[25] Q. Shafi and Z. Tavartkiladze. *Physics Letters*, **B473**:272, 2000.

[26] H.V. Klapdor-Kleingrothaus and A. Staudt. *Particle Astrophysics*. Institute of Physics Publishing, London, 1995.

[27] K.S. Babu, J.C. Pati, and F. Wilczek. *Physics Letters*, **B423**:337, 1998.

[28] Y. Fukuda *et al.* *Physical Review Letters*, **81**:1562–1567, 1998.

[29] Mark D. Messier. *Evidence for Neutrino Mass from Observations of Atmospheric Neutrinos with Super-Kamiokande*. PhD thesis, Boston University, 1999.

[30] J.C. Pati and A. Salam. *Physical Review Letters*, **32**:661, 1973.

[31] J.C. Pati and A. Salam. *Physical Review*, **D10**:275, 1974.

[32] Jogesh C. Pati. *Talk presented at NNN 2000 Workshop in Irvine,CA*, Feb. 2000.

[33] P. Nath, A.H. Chamesddine, and R. Arnowitt. *Physical Review*, **D32**:2348, 1985.

[34] P. Nath and R. Arnowitt. *Invited talk at the International Symposium on Lepton and Baryon Number Conservation*, 1998.

[35] S.P. Rosen. *Physical Review Letters*, **34**:774, 1975.

[36] M. Goldhaber, P. Langacker, and R. Slansky. *Science*, **210**:851, 1980.

[37] F. Reines, C.L. Cowan, and M. Goldhaber. *Physical Review*, **96**:1157, 1954.

[38] C.C. Giamati and F. Reines. *Physical Review*, **126**:2178, 1962.

[39] W.R. Kropp and F. Reines. *Physical Review*, **137B**:740, 1965.

[40] H.S. Gurr, W.R. Kropp, F. Reines, and B. Meyer. *Physical Review*, **158**:1321, 1967.

[41] F. Reines and M.F. Crouch. *Physical Review Letters*, **32**:493, 1974.

[42] J. Learned, F. Reines, and A. Soni. *Physical Review Letters*, **43**:907, 1979.

[43] G. Flerov, D. Klochkov, V. Skobkin, and V. Terent'ev. *Soviet Physics Doklady*, **3**:79, 1958.

[44] J.C. Evans Jr. and R.I. Steinberg. *Science*, **197**:989, 1977.

[45] R.I. Steinberg and Jr. J.C. Evans. *Proceedings from Neutrino '77*, page 321, 1977.

[46] J. Bartelt *et al. Physical Review*, **D36**:1990, 1987.

[47] M.R. Krishnaswamy *et al. Physics Letters*, **106B**:339, 1981.

[48] M.R. Krishnaswamy *et al. Physics Letters*, **115B**:349, 1982.

[49] G. Battistoni *et al. Nuclear Instruments and Methods in Physics Research*, **A245**:277, 1986.

[50] C. Berger *et al. Nuclear Instruments and Methods in Physics Research*, **A262**:463, 1987.

[51] W.W.M. Allison *et al. Physics Letters*, **B391**:491, 1997.

[52] G. Battistoni *et al. Physics Letters*, **133B**:454, 1983.

[53] C. Berger *et al. Physics Letters*, **B269**:227, 1991.

[54] D. Wall *et al. Physical Review*, **D61**:72004, 2000.

[55] R. Becker-Szendy *et al. Nuclear Instruments and Methods in Physics Research*, **A324**:363, 1993.

[56] R. Claus *et al. Nuclear Instruments and Methods in Physics Research*, **A261**:540, 1987.

[57] T.J. Phillips *et al. Physics Letters*, **B224**:348, 1989.

[58] Hirata *et al. Physics Letters*, **B220**:308, 1989.

[59] J.D. Jackson. *Classical Electrodynamics.* John Wiley and Sons, New York, 1975.

[60] H. Kume *et. al.* *Nuclear Instruments and Methods in Physics Research*, **205**:443–449, 1983.

[61] A. Suzuki *et. al.* *Nuclear Instruments and Methods in Physics Research*, **A329**:299–313, 1993.

[62] H. Ikeda *et. al.* *Nuclear Instruments and Methods in Physics Research*, **A320**:310–316, 1992.

[63] Jeffrey S. George. *Experimental Study of the Atmospheric ν_μ/ν_e Ratio in the Multi-GeV Energy Range.* PhD thesis, University of Washington, June 1998.

[64] M. Nakahata *et al.* *Nuclear Instrumemtatopm and Methods in Physics Research*, **A421**:113, 1999.

[65] S. Hiramatsu *et al.* *Proceedings for the International Conference on Nuclear Structure Studies Using Electron Scattering and Photoreaction, Sendai, Japan*, page 429, 1972.

[66] R.D. Woods and D.S. Saxon. *Physical Review*, **95**:577, 1954.

[67] H. Ejiri. *Physical Review*, **C48**:1442, 1993.

[68] Particle Data Group. *The European Physical Journal*, **C3**:1–794, 1998.

[69] J.S. Hyslop *et al.* *Physical Review*, **D46**:961, 1992.

[70] R.G. Glasser *et al.* *Physical Review*, **D15**:1200, 1977.

[71] M. Honda *et al.* *Physics Letters*, **B248**:193, 1990.

[72] M. Honda *et al.* *Physical Review*, **D52**:4985, 1995.

[73] G. Barr, T.K.Gaisser, and T. Stanev. *Physical Review*, **D39**:3532, 1989.

[74] T. Futagami *et al.* *Physical Review Letters*, **82**:5194, 1999.

[75] C.H. Llewellyn Smith. *Physics Reports*, **3**:261, 1972.

[76] D. Rein and L.M. Sehgal. *Annals of Physics*, **133**:79, 1981.

[77] D. Rein and L.M. Sehgal. *Nuclear Physics*, **B223**:29, 1983.

[78] P. Marage *et al.* *Zeitschrift für Physik*, **C31**:191, 1986.

[79] M. Gluck E. Reya and A. Vogt. *Zeitschrift für Physik*, **C67**:433, 1995.

[80] S.J. Barish *et al.* *Physical Review*, **D17**:1, 1978.

[81] S. Barlag *et al.* *Zeitschrift für Physik*, **C11**:283, 1982.

[82] P. Musset and J. Vialle. *Physics Reports*, **C39**:1, 1978.

[83] J.E. Kim *et al.* *Review of Modern Physics*, **53**:211, 1981.

[84] D. Rein. *Zeitschrift für Physik*, **35**:43, 1987.

[85] E. Oset *et al.* *Nuclear Physics*, **A484**:557, 1988.

[86] M. Nakahata *et al.* *Journal of the Physical Society of Japan*, **55**:3786, 1986.

[87] C.H.Q. Ingram *et al.* *Physical Review*, **C27**:1578, 1983.

[88] D. Ashery *et al.* *Physical Review*, **C23**:2173, 1981.

[89] D. Casper *et al.* *Physical Review Letters*, **66**:2561, 1991.

[90] Hirata *et al.* *Physics Letters*, **B280**:146, 1992.

[91] Y. Fukuda *et al.* *Physics Letters*, **B433**:9–18, 1998.

[92] *GEANT Detector Description and Simulation Tool.* CERN Geneva, Switzerland, 1993.

[93] T.A. Gabriel *et al.* *IEEE Transactions on Nuclear Science*, **36,1**:14, 1989.

[94] Davies. Machine Vision : Theory, Algorithms, Practicalities. Academic Press, San Diego, 1997.

[95] Yoshinari Hayato. *Search for proton decay into $K^+\bar{\nu}$.* PhD thesis, Tokyo Institute of Technology, February 1998.

[96] Particle Data Group. *Physical Review*, **D54**:85, 1996.

[97] W. W. M. Allison *et al.* *Physics Letters*, B427:217, 1998.

[98] Dave Casper. *Talk presented at NNN 2000 Workshop in Irvine,CA*, Feb. 2000.